Physik Department

The role of plastic collagen remodeling during structure formation of human mammary gland organoids

Dissertation
von

Benedikt Buchmann

Technische Universität München

Fakultät für Physik

Lehrstuhl für Zellbiophysik - E27

The role of plastic collagen remodeling during structure formation of human mammary gland organoids

Benedikt Buchmann

Vollständiger Abdruck der von der Fakultät für Physik der Technischen Universität München zur Erlangung des akademischen Grades eines

Doktors der Naturwissenschaften (Dr. rer. nat.)

genehmigten Dissertation.

Vorsitzender:	Prof. Dr. Martin Zacharias
Prüfer der Dissertation:	1. Prof. Dr. Andreas Bausch
	2. Prof. Dr. Maximilian Reichert

Die Dissertation wurde am 20.05.2021 bei der Technischen Universität München eingereicht und durch die Fakultät für Physik am 22.06.2021 angenommen.

Abstract

The extracellular matrix (ECM) is a key regulator driving cell proliferation and migration in two- and three-dimensional matrices. It can affect cellular behavior by biochemical, structural or mechanical signaling. For instance, aligned collagen fibers direct cell migration and enable a collective outgrowth, while the biochemical ECM composition modulates the general invasiveness of cells into the surrounding matrix. Further, beside its linear mechanical stiffness, the nonlinear and plastic properties of the ECM have been demonstrated to enable 3D cell migration as well as force-transmission between neighbouring cells and to steer complex multicellular structure formation. Yet, the mechanical description of common ECM matrices is mainly limited to the linear regime, while the nonlinear and plastic mechanical response function of the hydrogels is mostly neglected. Especially, during organogenesis the growth of multicellular aggregates and concomitant cell-ECM invasion is accompanied by distinct cell-ECM interactions and ECM remodelling processes, which are far beyond the linear regime. In particular, during the growth of primary human mammary gland organoids the global boundary conditions of the collagen I network play a crucial role in sculpting the resulting organoid morphology. While in attached collagen gels thin branched organoids develop, single primary human mammary gland cells cultivated in floating gels evolve into large, arborized organoids. The marked impact of the mechanical ECM properties on organoid development is further displayed as organoids undergoing alveologenesis are only observable in floating gels. Yet, the detailed mechanical cell-ECM interaction as well as the concomitant cellular behaviour during growth still needs to be unravelled.

In this thesis, first the nonlinear and plastic properties of the commonly used hydrogels collagen I, Matrigel and hybrid gels thereof are characterized. The resulting benchmark compares the highly nonlinear and plastic behaviour of collagen I to the predominantly linear mechanical response function of Matrigel. By the fabrication of hybrid gels composed of Matrigel and collagen I in varying stoichiometries the nonlinear and plastic properties can be gradually tuned. The rheological analysis is supplemented by a structural analysis of the hydrogels, which demonstrates that the hybrid gels cannot be seen as the sum of the individual components but exhibit a separate network structure. The mechanical characterizations and differences are transferred to the cultivation of human mammary gland organoids. Hereby it is demonstrated that the plasticity of the collagen network is prerequisite for branched organoid formation. By confocal long-term live cell imaging, static high-resolution imaging and various biochemical treatments the detailed organoid growth behavior and concomitant cellular interaction with the collagenous matrix is revealed. The observations are summarized into two mechanical descriptions refering branch elongation of human mammary gland organoids to the endogenous cell contractility. Non-contractile luminal organoids grow as a result of an internal cell proliferation, guided by designated leader cells with just minor ECM deformations. In comparison, highly contractile basal organoids exhibit an anisotropic long-ranged deformation field resulting from an orchestrated internal

collective cell migration. In addition, a mechanical stable collagen cage covering and stabilizing the grown organoids is revealed.

In summary, this thesis sets a framework for further nonlinear rheological characterizations of biomimetic hydrogels and highlights the significance of nonlinear and plastic remodeling processes during organoidogenesis. In particular, the detailed analysis of the growth behavior of healthy mammary gland organoids enables the establishment of a reliable model system to study tumorigenesis and related drug treatments.

Acknowledgments

Zuallererst möchte ich mich ganz herzlich bei meinem Doktorvater Prof. Andreas Bausch bedanken, welcher mir nicht nur die Arbeit an diesem spannenden Projekt ermöglicht hat, sondern stets auch eine offene Tür für hilfreiche Ratschläge und Ideen hatte. Danke auch dafür, dass du mich ermutigt hast mich bei der Studienstiftung zu bewerben und dass du mich bei dem ganzen Bewerbungsprozess unterstützt hast. Ich habe sehr viel von dir gelernt.

Des Weiteren danke ich meinen langjährigen Kollegen und mittlerweile besten Freunden Henry Dehne und Alfredo Sciortino. Ohne euch wäre die Arbeit im Labor wesentlich trister, Mittagessen öde und Konferenzen im Ausland deutlich langweiliger gewesen. Um die Diskussionen beim Mittagessen aber ein für alle Mal zu beenden: man kann alles auf eine Pizza machen, auch Ananas.

Die ganze Arbeit wäre nicht möglich gewesen ohne Lisa Engelbrecht, Marion Raich, Franz Hutterer, Pablo Fernandez und Hilary Ganz. Ich danke euch allen vielmals. Die harmonische Zusammenarbeit, das strukturierte Arbeiten und die hilfreichen wissenschaftlichen und nicht-wissenschaftlichen Diskussionen haben das Projekt so geformt, wie ich es alleine auf keinen Fall geschafft hätte.

Ebenfalls bedanken will ich mich bei dem gesamten Lehrstuhl von E22 und E27 für die angenehme Arbeitsatmosphäre. Insbesondere meinem ehemaligen Masterbetreuer Fabian Hecht, sowie meinen Kolleginnen und Kollegen Samuel Randriamanantsoa, Fabian Engelbrecht, Katharina Dürre, Philip Bleicher, Thomas Suren und Iris Ruider gilt großer Dank.

Abschließend danke ich meinen Eltern, Großeltern und meiner Schwester für die unermüdliche Unterstützung während des Studiums und der Promotion in allen Lebenslagen. Auch Anika gilt großer Dank dafür, dass du immer an meiner Seite stehst und du dir jedes Gejammer über gestorbene Organoide und missglückte Experimente angehört hast. Ohne euch hätte ich das niemals geschafft. Danke!

Contents

1 Introduction

The cultivation of human and animal derived cells *in vitro* enables the observation of complex structure formation processes relevant for the tissue development *in vivo*. By monitoring the cellular expansion, external and internal regulators driving structure formation can be extracted. Specifically, on 2D substrates the mechanical linear stiffness of the extracellular matrix (ECM) highly impacts the cellular proliferation, migration and even steers the differentiation of undifferentiated stem cells[1,2]. With the improvement of 3D cell cultivation in the last decades, the importance of the ECM during 3D cell migration and proliferation gained further significance. Here, especially hydrogels of collagen I and Matrigel, but also artificial hydrogels composed of alginate or polyacrylamide have been established[3,4]. In order to migrate through the dense network of various ECM proteins, cells need to interact and remodel their surrounding matrix, ultimately leading to a plastic remodelling. This remodelling is not solely depending on the linear mechanical stiffness, but highly depends on the viscoelastic, nonlinear and plastic response function of the used hydrogels[5]. In most rheological studies the mechanical description of the studied matrices is limited to the linear regime. Only for collagen I networks a linear and nonlinear mechanical description is available. Yet, the plastic behaviour is only described partly.

It is the first aim of this thesis to characterize the linear, nonlinear and plastic mechanical properties of commonly used hydrogels. Therefore, networks derived from collagen I, Matrigel and hybrid gels thereof were analyzed using nonlinear shear rheology. Hereby, the predominantly linear mechanical response of Matrigel is opposed to the highly nonlinear and plastic properties of collagen I networks. Further, it is demonstrated that the characteristic strain-stiffening and cycle-softening of collagen can be gradually tuned by the stepwise addition of Matrigel. In addition, the opposing mechanical response functions of collagen I and Matrigel are linked to the differing underlying network structure which was revealed by confocal imaging. In particular, the diminished collagen polymerization in presence of Matrigel is highlighted.

Such nonlinear and plastic deformations and remodeling processes do not only occur upon macroscopic deformations but are already observable during microscopic 3D single cell migration. The nonlinear mechanical regime gains even further significance within collectively migrating cohorts of cells, where higher forces are present. Especially, during organoidogenesis cells collectively grow into multicellular aggregates while interacting with their ECM. The thereby arising cell structures ultimately mimic the structural and biochemical morphology of their tissue of origin *in vivo*. The resulting multicellular aggregates are denoted as organoids. *In vitro*, organoids derived from human and animal cells established which mimic all kind of organs such as the brain, lung, kidney or mammary gland. Due to their origin of human tissue and the resulting compelling architecture, organoids bear a huge potential for human biology as well as patient-specific and regenerative medicine[6]. In addition, by monitoring organoid growth new insights into the development of healthy but also diseased

tissue can be achieved, what was nearly impossible before. Thus, organoids also serve as ideal model system to study tumorigenesis.

In 2018, every 18 seconds a women was diagnosed with breast cancer which thus is the most frequent cancer disease in women worldwide[7]. In particular, breast cancer is a highly heterogeneous disease, which generally can be divided in different classes[8]. Most general, carcinoma are divided into a preinvasive and invasive histological subtype. The most common subtype is the invasive ductal carcinoma of no special type (NST) during which highly proliferative cancerous luminal cells breach the basal cell layer and basement membrane. Guided by elongated collagen fibres within the stroma the cancerous tissue branches into the surrounding ECM. The arising ductal network maintains the branched structure of the healthy mammary gland. While the involved biochemical signaling pathways are already understood in quite detail, the specific cellular branching behavior still needs to be unraveled.

Due to the relevance of luminal cells during tumorigenesis the second aim of this thesis is to characterize healthy luminal cells cultivated on a 2D substrate and compare their motility and growth behavior with luminal cells embedded within 3D matrices. During their cultivation a special focus will be set on the signaling cascade of the Rho-associated protein kinase (ROCK), which predominantly regulates the actin cytoskeleton organization and the myosin-regulated contractility of the cells. Therefore, confocal live cell imaging is combined with various biochemical inhibitor treatments. Additional imaging of the underlying collagen network highlights the cell-ECM adhesion and interaction.

In 2015, a new protocol to cultivate highly branched mammary gland organoids from single primary human basal cells was presented[9]. The arising organoids establish a bilayered architecture with an outer layer of basal cells and an inner layer of luminal-like cells, which highly resembles the architecture of the human mammary gland *in vivo*. Thus, this assay introduces a promising model system to study the development of healthy and cancerous human mammary gland. Interestingly, it was demonstrated that the resulting organoid morphology can be steered by global boundary conditions of the collagen gel, indicating a pronounced mechanical interaction of the human organoids with their surrounding tissue. However, the underlying temporal-resolved organoid development and especially the precise mechanical interaction with the surrounding collagenous tissue remains elusive.

Finally, the third aim of this thesis is to resolve the specific branching behavior of the human basal mammary gland organoids and the underlying cell-ECM interaction. Therefore, dynamic confocal live-cell imaging during the organoid growth is combined with static high-resolution imaging of the underlying collagen network. The observations are complemented by laser ablation experiments of the collagen network and biochemical treatments affecting cell-cell adhesion, matrix degradation and cell contractility. As a result, a detailed mechanistic force-feedback loop describing branch elongation is summarized. Further, the formation of a mechanical stable collagen cage covering and stabilizing the growing organoids is revealed. Prerequisite for the collagen cage are the nonlinear and plastic properties of collagen I, as shown in the first aim.

2 Theoretical framework

2.1 Mechanical characterization of hydrogels by rheology

In general, the mechanics of a material is classified by its stress response upon the application of a strain. When the stress within a material increases linearly with the applied strain and thus follows Hook's law, the material is denoted as purely elastic. In contrast, when the stress relation of a material is proportional to the applied strain rate, it is called an ideal Newtonian liquid. However, in nature most materials exhibit a more complicated response with an elastic and liquid proportion. Such materials are called viscoelastic. In rheology, their elastic and viscous parts are unraveled by applying an oscillatory shear deformation $\gamma(t)$, while simultaneously measuring the stress response $\sigma(t)$. The resulting temporal strain and stress relations of a viscoelastic material follow the equations

$$\gamma(t) = \gamma_0 \sin(\omega t) \tag{2-1}$$

$$\sigma(t) = \sigma_0 \sin(\omega t + \delta) \tag{2-2}$$

where γ_0 refers to the strain amplitude, σ_0 to the maximal stress and ω to the angular frequency. The phase shift δ between strain and stress demonstrates the viscoelastic proportion of a material. An ideal elastic material exhibits no phase shift and thus $\delta = 0°$ between the strain and stress. In comparison, an ideal Newtonian liquid exhibits a shift of $\delta = 90°$. Thus, the phase shift of a viscoelastic materials is in the regime $0° < \delta < 90°$. Further, the viscoelastic material properties are characterized by the complex shear modulus *G**, characterizing the stiffness of the material and the related phase angle $\tan(\delta)$:

$$G^* = G' + iG'' \tag{2-3}$$

$$tan(\delta) = \frac{G''}{G'} \tag{2-4}$$

G' refers to the storage modulus which is calculated by the ratio of stress to strain. The storage module defines the stored energy within the material, which drives the shape reversal after the strain is released. The viscous part of the material is displayed in the loss module *G''* and refers to the dissipated energy as a result of the internal friction. In order to measure the storage and loss module experimentally, strain-stress experiments with constant strain rate $\dot{\gamma}$ are applied to the sample. The resulting slope of the strain-stress relation refers to the storage module. Further, the resulting network changes upon strain are dependent on the applied strain rate. For instance, on short time scales entangled polymer networks appear solid as stresses within the network cannot relax. In contrast, on long time scales polymers can slide along each other *via* reptation and the material appears fluid. Accordingly, the material behavior on different timescales needs to be probed. As a measure, frequency sweeps of the samples are conducted, during which small non-destructive deformations with increasing frequency are applied. Simultaneously, the shear module is measured and displayed in dependency of the applied frequency.

However, storage and loss module are only defined within the linear regime in which the linear relation between stress and strain is fulfilled. Upon the material dependent yield stress, the linear mechanical regime devolves into a nonlinear description. Within the nonlinear regime the storage modulus is replaced by the differential module *K*, which is defined as[10]:

$$K = \frac{\mathrm{d}\sigma}{\mathrm{d}\gamma} \tag{2-5}$$

The concomitant nonlinear deformations lead to irreversible plastic network remodeling processes, which are displayed by irreversible changes of fiber length, fiber buckling and by the breakage and new formation of weak crosslinks. Which of the underlying processes occur, highly depends on the individual fiber properties as well as the applied strain amplitude and strain rate[11]. For instance, a low strain rate in combination with a high strain amplitude leads to the remodeling of weak crosslinks, while in contrast a high strain rate in combination with a high strain amplitude leads to a permanent fibre elongation. Upon cyclic deformations this plastic network remodeling leads to a cycle dependent mechanical response. However, upon too large deformations the system cannot withstand the stress anymore and ultimately breaks. This irreversible breakage is defined by the ultimate yield strain and stress.

2.2 Mechanisms of 2D and 3D cell migration

In order to study biological, biochemical and physical processes during organogenesis or tumorigenesis, the complex nature of the systems *in vivo* is reduced by cultivating, manipulating and monitoring cells and recapitulated tissue on 2D substrates or in three-dimensional extracellular matrices[12]. In such environments, cell-ECM adhesion and sensing of the substrate as well as the resulting cell migration can be analyzed in detail. In the following, the migratory behavior of cells cultured in 2D and 3D will be compared. In addition, the collective cellular migration and interplay during branching morphogenesis will be described.

2.2.1 Individual and collective cell migration in 2D

2D single cell migration is induced by a polarized expression of the actin network in the direction of migration[13]. Depending on the cell type and the properties of the ECM either thin filopodia-like protrusions or a broad lamellipodia forms in the front of the cells. This polarization is orchestrated by complex signalling cascades involving various proteins such as PIP_3, CDC42 or RAC[14]. In order to adhere to the substrate and to sense the environment, cells form focal adhesions at the cell-ECM boundary[15]. *Via* transmembrane receptors external cues are then transmitted to the internal actin cytoskeleton. During migration, the adhesion in the back loosens and leads to a detachment of the cells from the substrate, which enables the cells to protrude forward. During this, cells apply traction forces *T* in the opposite direction of cell migration on the substrate. Spatially, this force application is limited to the front of the migrating cell, while at the back of the cells the initially applied force is released[16]. Cells sense the stiffness of the underlying substrate during the force built-up *via* actomyosin contractions

and by cell-ECM adhesion *via* focal adhesions. Ultimately, cells migrate preferentially in the direction with the higher stiffness. This directed migration upon the sensing of the substrate stiffness is denoted as durotaxis[1].

Within confluent cell layers, cells are coupled via cell-cell adhesion to their neighbours and thus migrate collectively. To specifically study such collective cell migration, wound healing assays are conducted[17]. The closure of a gap between two opposing epithelial sheets is monitored. During the collective outgrowth, the individual cell traction forces T_x of all cells integrate as a result of the internal cellular coupling along their neighbours to an internal stress σ_{xx} within the sheet perpendicular to the substrate (Fig. 2-1A). The resulting internal stress depends on the cell sheet height h_z as well as width h_y and is calculated by[18]

$$\langle \sigma_{xx}(x) \rangle = \frac{1}{h_z h_y} \int_0^x \int_0^{h_y} T_x(x', y')\, dx'\, dy' \tag{2-6}$$

According to the formula, the cellular coupling and the directed cell migration induce an internal stress within the epithelial sheet which continously increases with distance to the leading edge, while the individual traction forces stay constant throughout the whole area (Fig. 2-1B). After the closure of the gap and within a confluent cell layer an ongoing cell migration can be observed. Spatial clusters with defined correlation length of similarly migrating cells can be observed. With increasing cell-cell and cell-substrate adhesion as well as with increasing cell density the cellular velocity reduces until the cells undergo a jamming transition which ultimately stops their migration[19,20]. In some cases, the increasing pressure leads to a buckling of the epithelial sheet into the third dimension, which ends up in the formation of cellular domes[21].

The arising collective patterns during cell migration can be steered by spatially constricting cell migration. To this end, only defined areas are functionalized with ECM-proteins such as fibronectin or collagen to enable cell adhesion, while the remaining space is passivated and thus excluded for cell adhesion[22]. As a result, arbitrary patterns to study individual and

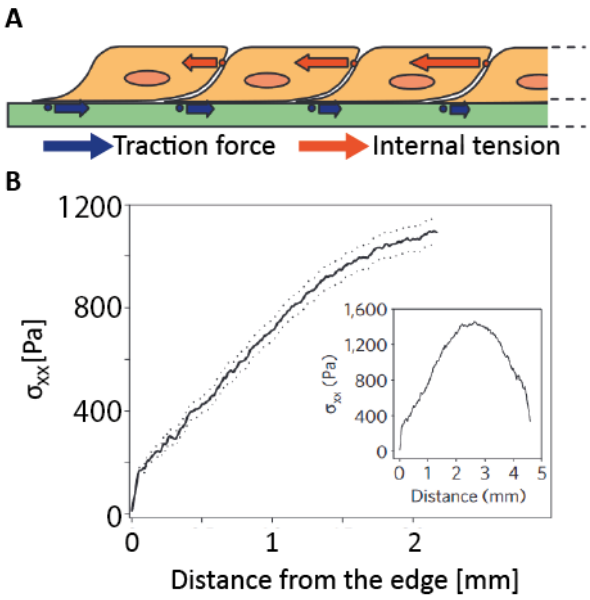

Figure 2-1: 2D tug of war model*[18]*. A *Cells within an epithelial layer apply individual traction forces on the substrate. Due to cellular coupling, the individual traction forces integrate which leads to an increasing internal tension.* ***B*** *With increasing distance to the edge, the tension within the epithelial layer increases.*

collective cell migration, as well as cell-cell interactions, can be designed. By analysing the cell migration on strip-like patterns, it can be demonstrated that the correlation length of cell migration correlates with the dimensions of the spatial confinement[23]. As long as the strip width is below the maximal correlation length, all cells adhering to the pattern exhibit a collective outward directed migration along the long strip axis. On wider strips, this collective migration breaks into smaller cellular clusters with the size of the correlation length and the global velocity field exhibit swirl-like patterns. Accordingly, on circular patterns cells start to exhibit a collective cellular rotation as long as the size of the pattern is not exceeding the correlation length of the underlying cell migration. Small patterns decorated with only two cells are sufficient to induce a polarization within the cells such that they exhibit a persistent rotation[24]. This collective cell rotation is not restricted to circular patterns but can be seen in any ring-shaped or in 3D-like cylindrical micropattern as soon as the cells are confluent and coupled *via* cell-cell adhesion[25,26].

2.2.2 Cell-ECM invasion and branching morphogenesis in 3D

In 3D assays, cells are already cultivated within a natural spatial confinement given by the ECM. Here, cells need to migrate through a dense network with various adhesion sites and differing biochemical and mechanical properties. 3D single cell migration modes are divided in three different modes: mesenchymal, amoeboid and lobopodial (Fig. 2-2A)[27]. In particular, mesenchymal migration is characterised by a strong cell-ECM adhesion *via* focal adhesions and a distinct ECM remodelling during the ECM invasion. Actin polymerization at the leading edge generates a lamellipodia which in turn aligns the ECM fibres in the direction of the migration. A simultaneous high proteolytic activity degrading the ECM further facilitates the invasion. In comparison, during amoeboid cell migration, cells show a reduced cell-ECM adhesion and mainly exhibit a round cellular morphology. Their migration is directed by cell body deformations squeezing through the pores of the ECM. Thus, cells follow the path of least resistance. As last, lobopodial migration can be described as mix of the other two migration modes. Hereby, cells exhibit a strong cell-ECM adhesion, while an internal asymmetric pressure drives cell body deformations which ultimately leads to the formation of protrusions of the plasma membrane called lobopodia at the leading edge. In particular, position of the nucleus in combination with myosin-II contractility within the cell generates the asymmetric pressure[28].

Due to the spatial confinement, 3D cell migration is predominantly dependent and regulated by the surrounding biochemical, structural and mechanical milieu (Fig. 2-2B). Guiding cues can hereby be the molecular ECM composition offering various adhesion sites, the microscopic network structure guiding migration by pores, aligned fibres or stiffness gradients, as well as the stiffness and elasticity of the network. For instance, while cells embedded in collagen exhibit an invasive behaviour, the same cells cultured in Matrigel show a reduced ECM invasion[29]. 3D cell migration is accompanied by distinct ECM remodelling processes such as matrix degradation by matrix metalloproteinases or fibre alignment as consequence of

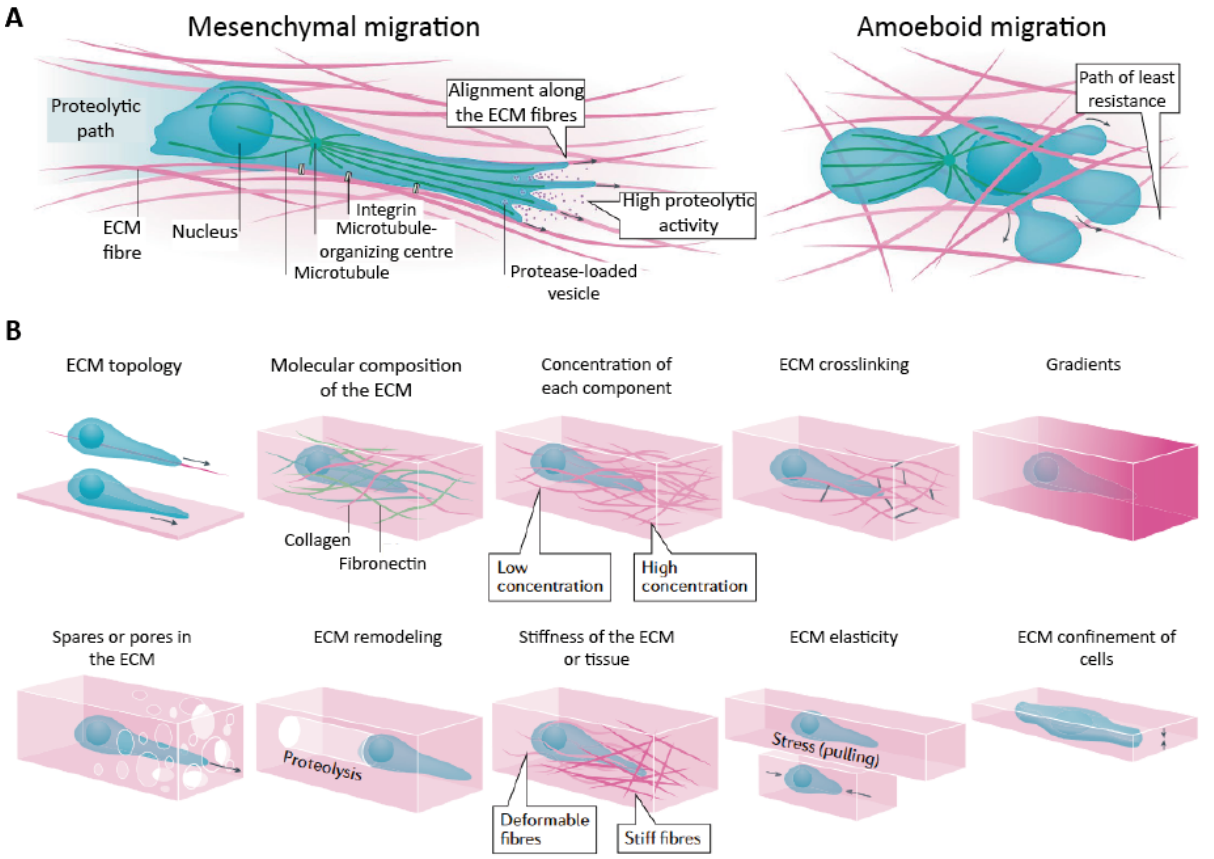

Figure 2-2: 3D migration modes and guiding cues[27]***. A*** *Representative scheme opposing mesenchymal and amobeoid migration.* ***B*** *In 3D migration the ECM steers the cellular invasion by various properties such as composition, structure or stiffness. Remodeling processes such as fibre alignment or matrix degradation are of plastic nature.*

mechanical deformations[30,31]. As a result, cells tend to migrate in regions with higher stiffness or squeeze into regions with large pore to follow the path of least resistance[32]. Thus, instead of relating the global properties of the matrix to the cell migration the local properties in the near field of the cells need to be taken in account. The described remodelling is irreversible and thus plastic. However, already the plastic nature of the ECM is sufficient to regulate cell migration. Human breast adenocarcinoma cells change their utilized migration mode dependent on the mechanical plasticity of the network[33]. While at low plasticity cells mainly show no migration and ECM invasion, at high plasticity cells exhibit a protease-independent migration penetrating the ECM. Further, cells within 3D matrices migrate in the direction of plastically aligned collagen fibres[11,34,35]. However, the cellular force built-up to plastically align the collagen fibres as well as the spatiotemporal-resolved alignment process is still topic of intense research.

During complex structure formation processes such as embryogenesis or organogenesis cells do not exhibit an individual migration but invade their surrounding in a collective manner. For organs with a branched network architecture such as the mammary gland, the lung or the kidney this invasion process is generalized as branching morphogenesis[36]. The underlying specific branching strategy as well as the involved biochemical signalling pathways depend on the organ as well as organism. In general, branching morphogenesis is classified into three different mechanisms: 1.) epithelial folding, 2.) matrix-driven branching and 3.) invasive

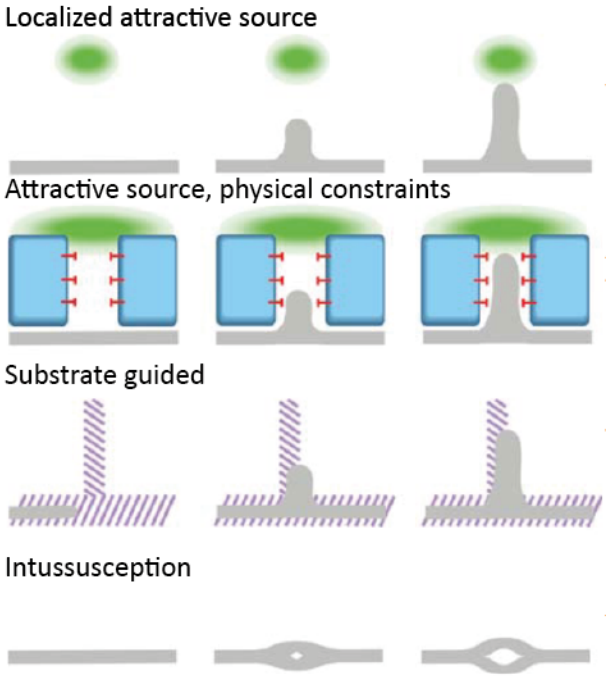

Figure 2-3: Possible guiding cues during matrix-driven branching morphogenesis[36]. *Branching can be guided by a biochemical source, the substrate or a combination of both.*

branching[37]. During epithelial folding, the change in tissue shape can be induced by various internal or external cues. For instance, active cellular forces can trigger an individual cell shape change from basal to apical which results in a global folding. Further, cells can also locally rearrange their position by an internal migration and thus induce a global shape change[38]. In addition, folding can also be induced by a differential proliferation leading to a local change in cell density or by external compressive forces[39]. During such folding process, cells show a reduced cell-ECM interaction and do not form filopodia or lamellipodia. In contrast, during matrix-driven branching cells exhibit a marked interaction with their surrounding and tissue invasion is specifically guided by external cues. In dependency on the organ, organism and ECM these external cues can be a localized biochemical attractive source, physical constraints or a guidance by the substrate (Fig. 2-3)[36]. For instance, in the nascent mouse mammary gland aligned collagen fibres seem to direct the growth of the invading epithelium[40]. During invasive branching, invasion is orchestrated by one or more specific leader cells at the tip of the elongating branch, while the so-called stalk cells in the back show a more passive migration. During invasion, the leader cells strongly interact with the surrounding ECM and exhibit filopodia-like protrusions. The necessary forces are thought to be exerted by the leader cells only, which actively pull on the stalk cells which then elongate the branch *via* intercalations. However, the detailed force distributions and force built-up as well as the specific role of the stalk cells remain elusive. Furthermore, most of the related characterisations were investigated during the development of the *Drosophila* tracheal or during sprouting angiogenesis in the vertebrate vasculature[41,42]. Observations describing the tip and stalk cell dynamics in other tissues are still missing. Thus, it remains unclear if those organism-specific observations can be generalized for other systems.

In summary it has to be noted, that branching morphogenesis is a highly complex process, which *in vivo* can exhibit properties of all three presented mechanisms and thus cannot solely be reduced to a specific morphogenesis type. Especially, invasive branching and matrix-driven

branching exhibit similar characteristics. Thus, to fully unravel the branching of a specific organ, a detailed analysis of the cellular proliferation and migration as well as the interaction with the ECM is necessary.

2.3 Organoids as model systems

With beginning of the early 2010s, 3D cell culture assays significantly improved in order to recapitulate organ growth *in vitro*[43]. By the cultivation of patient- or animal-derived tissue fragments, embryonic stem cells or pluripotent stem cells in 3D matrices the fabrication of organ-like aggregates was established. Hereby, cells self-organize into multicellular organoids which exhibit a simplified but realistic micro-anatomy. Throughout the last years, organoids recapitulating the brain, lung, pancreas, mammary gland and many more organs have been established[44]. Due to their origin of patient-derived stem cells or tissue fragments, organoids bear the potential to introduce a patient-specific medicine[45]. For instance, organoids can be used as model systems to develop a patient-specific drug treatment or to replace diseased tissue *via* regenerative medicine[46]. As an essential basis, the organoid assays and the respective developmental processes need to be fully unraveled. In the following, the human mammary gland and related organoid systems will be in focus.

2.3.1 The human mammary gland

The development of the mammary gland is unique since it mainly takes place after birth compared to tissues like the lung or kidney which fully branch already during embryogenesis[47]. During embryogenesis, only a small rudimentary networks forms, which first during puberty invades into the surrounding collagen-rich environment. As a result, a tree-like ductal

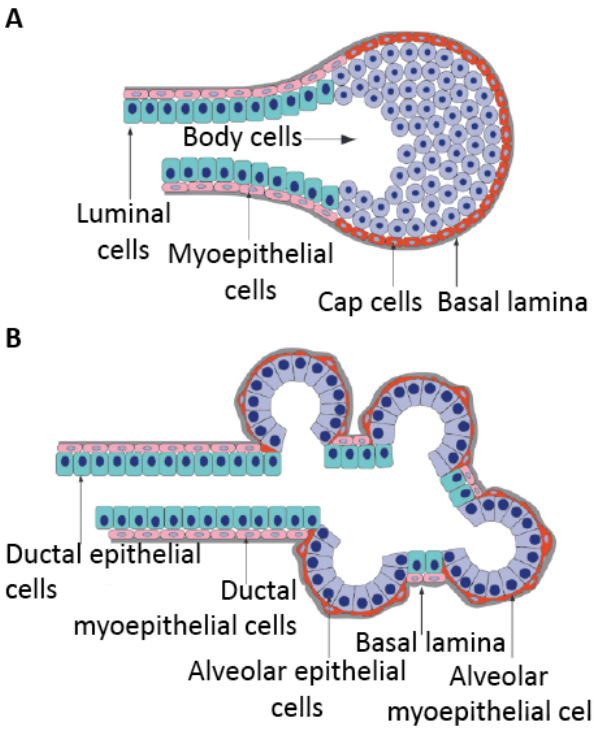

Figure 2-4: Scheme of the mammary gland during different developmental stages[48]***. A*** *Branches of the adult mammary gland exhibit two cell layers of luminal and myoepithelial cells which are covered by a basal lamina.* ***B*** *During pregnancy the mammary gland undergoes marked changes in its architecture during which several alveoli arise at the terminal end buds.*

networks forms. The arising ducts exhibit a bilayered architecture in which secretory luminal cells line the lumen and are surrounded by a layer of contractile myoepithelial or basal cells, which are in contact with the basement membrane (Fig. 2-4A)[48]. Further, it is thought that in-between the layer of both cell types, stem cells are present, which give rise to the either basal or luminal cells[49]. Throughout every menstrual cycle and during pregnancy, the mammary gland undergoes further extensive tissue and ECM remodelling, upon upregulation of hormones such as estrogen, progesterone and somatotropin[50]. During pregnancy, the branched ductal network expands and ultimately forms alveolar buds at the tips of tertiary branches, which are filled with alveolar luminal cells (Fig. 2-4B). These alveolar luminal cells are then responsible for the lactation, while the contractile basal cells pump the milk towards the nipple to feed the baby. By the end of breastfeeding the mammary gland again undergoes marked structural changes back to the initial architecture in a process called involution[51]. Hereby, the regulation of several signaling pathways induces partial apoptosis of the cells within the mammary gland, while neighboring cells close the resulting gap. The resulting tissue reduction is accompanied by marked ECM remodeling *via* the upregulation of matrix metalloproteinases. With beginning of the next pregnancy, this cyclic tissue remodeling starts from the beginning again.

It has to be noted that the presented development of the mammary gland is mainly based on observations found during the branching morphogenesis of the mammary gland in mice, which are then transferred to the human mammary gland. Due to technical limitations and ethical reasons the development of the human mammary gland is nearly impossible to resolve. However, it is known that the development of the mammary gland of human is far more complex and displays more distinct developmental stages than the development of the murine mammary gland[52]. Especially, the extracellular matrices of both tissues differ drastically. While the human mammary gland is surrounded by a collagen-rich environment, the mice mammary gland is only covered by a thin basement membrane embedded in an adipose stroma. To overcome the limitations in studying the human mammary gland and to further unravel underlying growth processes and signaling pathways, organoids derived from human mammary gland tissue were developed with the aim to be used as adequate model systems[9,53].

2.3.2 Human mammary gland organoids

The common preparation assays of mammary gland organoids can mainly be distinguished by three different experimental components: the cell source, human or mouse, the initially seeded cell amount, single cell suspension or tissue fragments, and the main component of the used ECM, collagen I or Matrigel. Due to the different extracellular environment of the mammary gland in human and mice *in vivo*, organoid assays based on human tissue predominantly use collagen I gels as ECM, while organoids grown from mouse cells use Matrigel as ECM.

In Matrigel, single cells and tissue fragments extracted from mice grow into densely branched globular-like organoids[54]. At the end of their development a ductal network connecting the branches arises. An upregulation of the ROCK-signaling cascade has been demonstrated to be prerequisite for organoid growth. In particular, branching is dictated by local cell rearrangements within the terminal end buds without the formation of cellular extensions or protrusions[38]. The type of ECM plays a crucial role during 3D cell migration and thus branching morphogenesis. For mammary gland organoids cultivated from aggregates of human cells, it has been demonstrated that the cellular proliferation and the resulting organoid morphology can be steered by either using Matrigel, collagen I or a complex ECM hydrogel composed of collagen I, hyaluron and laminin (Fig. 2-5A)[53]. While cell fragments in Matrigel grow into spherical aggregates, cell fragments within a pure collagen I matrix start to invade their surrounding by developing short branches. By further tuning the matrix composition, highly branched organoids form a densely packed core from which single branches emerge in the time course of two weeks, which resemble the mammary gland *in vivo*. In such matrices, protrusive leader cells at the tip of extending branches guide the branch extension. On the other side, by further tuning the culture conditions, the cultivation of single primary human cells in a pure collagen I matrix was enabled[9]. As a result, highly branched organoids with a polarized bilayered ductal architecture develop in the time course of two weeks. In particular, each organoid develops from a single primary human basal cell. After two weeks, organoids exhibit an outer layer of basal cells which are covering luminal-like cells expressing GATA3 in an inner layer. The organoids are covered by a self-expressed thin layer of laminin, which mimics the basement membrane *in vivo*. Further, it has been demonstrated in this assay that organoid morphology can be steered by the global boundary conditions of the collagen gel (Fig. 2-5B). While in attached gels organoids develop thin elongated branches, organoids in floating gels exhibit thick branches undergoing alveologenesis. As a result, branch tips round up and form spherical alveoli. Ultimately, the resulting structures are denoted as terminal ductal-lobular like units (TDLU). However, their specific temporal-resolved growth and the detailed mechanical interaction with the ECM still needs to be unraveled, which will be the scope of this thesis.

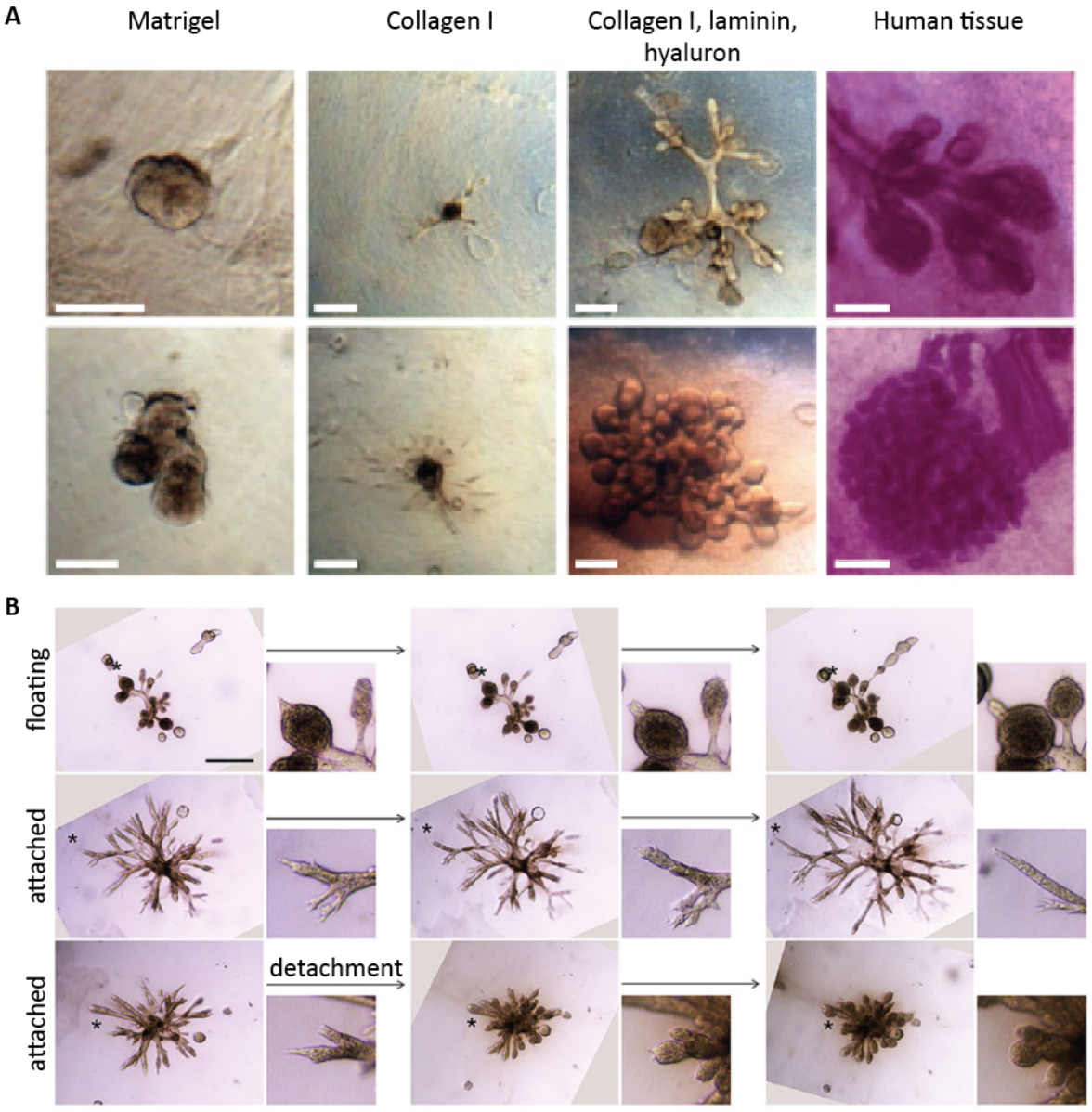

Figure 2-5: Human mammary organoid morphology can be steered by the type of ECM and the boundary conditions. A *Human cell aggregates cultivated in Matrigel only grow into spherical aggregates. Within a pure collagen matrix single branches develop from the aggregate. Highly branched organoids develop in a mixture of collagen I, laminin and hyaluron, resembling the human tissue in vivo*[53]. ***B*** *Organoid morphology of organoids derived from single basal cells can be steered by the boundary conditions of the collagen gel. A detachment of attached collagen gels leads to a shrinkage of the organoids and a widening of the branches*[9]*. Scale bars, 200 µm (**A**), 500 µm (**B**).*

3 Materials and Methods

3.1 Rheology

3.1.1 Rheological testing protocol

In order to analyze the linear and nonlinear mechanical properties of different hydrogels, macro rheology was performed. Experiments were conducted with an Anton-Par Physica MCR 301 stress-controlled rheometer, equipped with a 50-mm cone-plate geometry. The sample volume was set to 750 µl resulting in an according gap size of 300 µm. Prior to the measurements, the plate and cone were treated with 5 µg/cm^2 Cell-Tak Cell and Tissue Adhesive (Corning), enabling a strong attachment of the gels to the plates. After an incubation time of 30 mins, the plates were rinsed ten times with water to remove unbound proteins. To prevent unintended polymerization the lower plate was cooled down to 4°C and first heated up to 37°C once polymerization of the hydrogels was ready to be induced. Five minutes after inducing polymerization, the chamber was sealed with PBS to prevent evaporation. In order to quantify the mechanical properties of the studied hydrogels the following protocol was conducted:

1. Polymerization was monitored by applying continuous oscillations with a strain amplitude of 1% at a frequency of 1 Hz until the storage module G' and loss module G'' equilibrated (Fig. 3-1A). Typically, this took 20 mins.
2. After polymerization, frequency sweeps from 0.01 to 60 Hz with an amplitude of 1% strain were applied to probe the linear properties of the hydrogels (Fig. 3-1B).
3. In order to quantify the nonlinear mechanical response of the hydrogels, '$\dot{\gamma}$-pulses' with increasing strain amplitude and constant strain rate of 1 %/sec were applied (Fig. 3-1C). Each strain amplitude was repeated four times. The strain amplitude was stepwise increased from 40 to 120 % in steps of 20 %.
4. Finally, a strain of 300 % was applied to the sample to characterize the yield strain and stress.

For specifically analyzing the yield strain and stress of untreated networks the protocol was adapted. Here, step 1 was directly followed by step 4. Thus, the pure stress-strain relation was measured by applying a maximal strain of 300 % with a constant strain rate of 1 %/sec independent on the history of network deformations. In order to probe the relaxation behavior of collagen and Matrigel, strain jumps were conducted. Therefore, an instantaneous strain of 80% was applied to the sample. This strain was hold until the relaxation module G(t) equilibrated. Typically, the strain jump measurements were conducted for 80 mins.

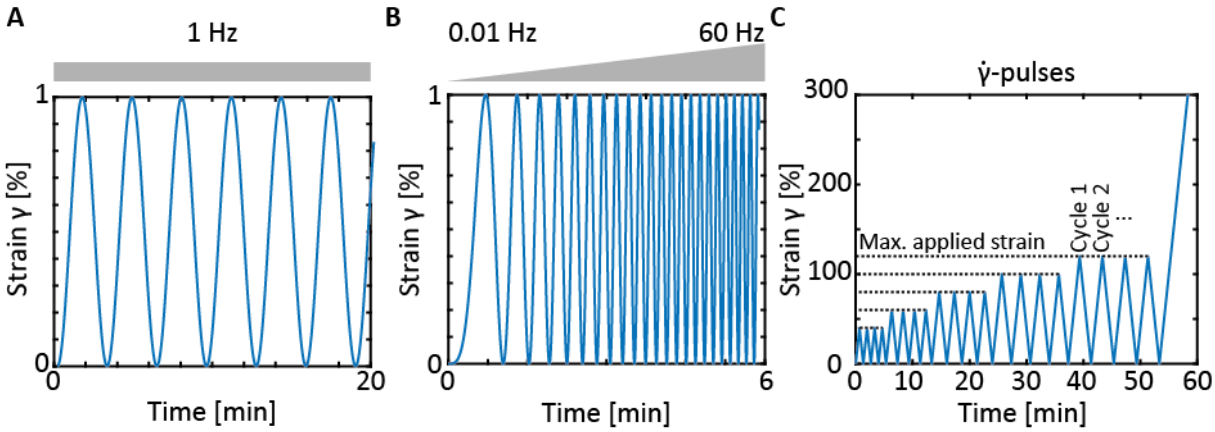

Figure 3-1: Experimental protocol for probing the linear and nonlinear properties of the different hydrogels. ***A*** The polymerization of the hydrogels is probed by applying continuous oscillations with 1 % strain at 1 Hz. **B** The linear properties are characterized by frequency sweeps between 0.01 and 60 Hz at a maximal strain of 1 %. **C** The nonlinear and plastic properties are revealed by cyclic $\dot{\gamma}$-pulses, which are finalized by applying a strain of 300 %.

3.1.2 Hydrogel preparation

In order to reveal the mechanical environment of the mammary gland organoids in detail, Collagen type I from rat tail (Corning) was mechanically characterized. Polymerization was induced by a combination of raising the pH-value and heating the sample from 4°C to 37°C. Therefore, PBS was mixed with neutralizing solution consisting of 550 mM Hepes in 11x PBS. The volume of neutralizing solution matches a tenth of the final collagen volume. Subsequently, pure collagen solution was added with the desired volume. All mixing steps were performed on ice. Finally, polymerization was completed by heating the solution in-between the rheometer plates.

In addition, growth factor reduced and phenol red-free Matrigel (Corning) with a protein concentration of 8.2 mg/ml was analysed. Polymerization was induced in-between the rheometer plates by heating the plates from 4°C to 37°C within the time course of around 40 sec.

Hybrid gels of collagen and Matrigel were studied in varying stoichiometry. The analysed networks were enriched with either 25% or 50% Matrigel of the total sample volume, while collagen concentration was kept at 1.3 mg/ml. Sample preparation was achieved by first mixing PBS, neutralizing solution and collagen in the desired ratio. Subsequently, the solution was mixed thoroughly and afterwards enriched with Matrigel, followed by additional mixing. Finally, polymerization was induced by heating the resulting solution in-between the rheometer plates to 37°C.

During handling of Matrigel, all pipette tips and tubes used were stored on ice to prevent unintended polymerization.

3.1.3 Collagen modification

Fluorescent collagen for live cell imaging and structure analysis was prepared following a previous published protocol[55]. As first step, collagen was dialysed at 4°C to reach pH 7. Collagen was conjugated with Atto 488 (Merck) *via* overnight incubation. Subsequently, an additional dialyse for 8 hrs was conducted to remove unbound dye. In order to prevent unwanted polymerization, a dialyse with acid was performed overnight. Finally, the solution was stored at 4°C. Prior to prepare collagen gels to either perform structure analysis of to embed organoids, the fluorescent collagen was mixed with pure collagen solution in a ratio of 1:5.

In order to alter the mechanical properties of the collagen networks, unpolymerized collagen was glycated with Ribose[56]. It was shown that thereby the equilibrium compressive modulus gradually increases with increasing concentration of Ribose. While the addition of 100 mM Ribose leaves the structure of the developing collagen networks unaffected, the addition of 200 mM Ribose leads to larger collagen fibres.

To prepare the modified collagen, collagen was incubated for 3 days in 0.1% sterile acetic acid at 4°C with 0.5 M ribose. Such treatment leads to a Maillard reaction of the Ribose with the collagen, ultimately leading to Amadori products around single collagen fibres, which during polymerization introduce an additional crosslinking of collagen fibers[56]. The glycated collagen was mixed with unmodified collagen to prepare collagen solutions with the desired concentration of Ribose. In particular, gels with 200 mM Ribose were analysed. Polymerization was induced similar to untreated collagen.

3.2 Cell culture and live-cell imaging

For general cultivation and experimental preparation, cells were cultivated inside an HERAcell 150i incubator (Thermo Scientific). Within the incubator, the temperature was constantly hold at 37 °C and the atmosphere was set to a composition of 3 % O_2 and 5 % CO_2. Samples used for drug screening were prepared in 24-wells (Sarstedt AG & Co. KG) and samples used for live-cell imaging in 2-wells (Ibidi). If needed, chemicals were sterilized by using a syringe and a filter with a pore size of 0.2 µm (Sarstedt AG & Co. KG).

3.2.1 Luminal cells in 2D and luminal organoids in 3D

For luminal cell cultivation Branched Luminal Organoid Medium (BLOM) was used, which is based on the previously published Branch Cancer Organoid Medium (BCOM)[57]. In comparison, BLOM is further enriched with 0.5 % fetal calf serum (FCS). Its detailed composition can be found in table 3-1.

Prior to seeding luminal progenitor cells in 2D, cell culture dishes were functionalized with rat tail collagen I at a concentration of 5 µg/cm^2. In particular, the pure collagen solution was

Luminal	Basal	
Day 0 – Day 14	**Day 0 – Day 5**	**Day 5 – Day 14**
250 ng ml^{-1} or R-Spondin	0.004 ml ml^{-1} Bovine Pituitary Extract	
5 ng ml^{-1} EGF	10 ng ml^{-1} EGF	
20 ng ml^{-1} FGF 7	5 µg ml^{-1} Insulin	
20 ng ml^{-1} FGF 10	0.5 µg ml^{-1} Hydrocortisone	
5 nM Neuregulin 1	10 µM Forskolin	
5 µM Y-27632	3 µM Y-27632	-
0.5 % FCS	0.5 % FCS	-
100 ng ml^{-1} Noggin		
500 nM SB202190		
B27 supplement		
500 nM A83-01		

Table 3-1: *Media composition for luminal and basal organoids. Luminal organoids are cultivated for two weeks in the same media. Basal organoids require upon day 5 of cultivation a differently composed media.*

diluted in PBS and the dish was incubated with the resulting mix for at least 2 hrs at 37 °C. Subsequently, unbound collagen was removed by washing the functionalized dishes three

times with PBS. Finally, 20.000 cells were seeded and incubated at 37 °C and an atmosphere of 5 % CO_2 and 3 % O_2. Five days after seeding the cells for the first time, media was completely exchanged. Afterwards, media was changed every two days. For cell splitting, medium was removed, and cells were washed with PBS before they were incubated with 0.15 % Trypsin-EDTA for at least 5 minutes. After cells detached from the surface Trypsin was inactivated using trypsin neutralizing solution. Cells were spun down, the resulting pallet was re-suspended in medium, and the cells were seeded again. In total, luminal progenitor cells were successfully expanded in 2D for up to 17 population doublings.

Wound healing assays were prepared by spatial limiting cell cultivation to two opposing areas using 2-well Culture inserts (Ibidi). To prevent cellular adhesion to the inserts and to enhance reproducibility, the inserts were passivated with Pluronic F-127 (Sigma-Aldrich). In particular, 100 µg Pluronic were dissolved in 50 mL PBS in which the inserts were incubated for one hour. To enable passivation these steps needed to be performed at 4 °C. Afterwards, inserts were air-dried before being placed inside the 2-wells. Cells were seeded within the two chambers of the insert at a cell number of 15.000 and cultivated until they reached confluency. Prior to live cell imaging the insert was removed gently using a sterile tweezer.

3D cultivation was prepared following a previously described protocol[9]. To be specific, between 250 and 2000 freshly sorted luminal progenitor cells were mixed with rat tail collagen I solution, neutralizing solution and cell culture media. The amount of each component was chosen such that the final collagen concentration was set to 1.3 mg/ml. Further, 2 µl/ml fluorescent beads with a diameter of 1 µm were added to the solution. To prevent unintended polymerization, all mixing steps were performed on ice. Polymerization was induced by heating the dishes for one hour to 37 °C. After successful polymerization, 2x concentrated cell culture media was added to the cells. To prepare floating collagen gels, the gels were detached from the boundary using a pipette tip. After five days the media was completely exchanged and in the following days partwise exchanged every 2 days.

3.2.2 Basal organoid preparation

Basal organoids were prepared following a previously published protocol[9]. As a difference, no sorted cells were used during preparation. Luminal cells poorly proliferate and merely grow into spherical aggregates in the cell culture medium optimized for basal cell proliferation. Consequently, branching organoids can be unequivocal identified as basal organoids. In this work, organoids from five different donors of different age and with different parity were prepared (Table 3-2). In-between the donors no significant difference in organoid morphology or cellular behaviour was observed. For gel preparation, human mammary gland epithelial cells were thawed and instantly diluted in fresh mammary epithelial growth medium (PromoCell MECGM). The resulting cell suspension was centrifuged until a cell pallet was visible at the bottom of the tube. To remove remaining DMSO, the supernatant was substituted with fresh media. Cells were counted and mixed with collagen I solution, neutralizing solution and fresh media. In total, 20.000 cells were seeded per 1 ml collagen solution, while the final collagen concentration was set to 1.3 mg/ml. Only for specific experiments, the collagen concentration was varied. For specific experiments 2 µl/ml of 1 µm sized polystyrene beads (Bangs Laboratories) were added. To induce polymerization the resulting solution was heated to 37 °C. After one hour of polymerization, cell culture media was added to the gels and the gels were detached from borders by gently scratching of the gel-wall-interface with a pipette tip. During the first five days, the media was enriched with 10 µM Forskolin (Biomol), 3 µM Y-27632 (Biomol) and 0.5% FCS. From day 5 on, the cell culture media was replaced by media only enriched with 10 µM Forskolin. Media was partly changed every 2 days. The detailed composition of the medium can be found in Table 3-1.

Table 3-2: *Donors used for organoid preparation.*

Donor	Age (years)	Parity
M20	67	2
M21	61	1
M23	65	2
M26	34	2
M28	38	1

3.2.3 Immunostaining

In order to stain the organoids against different biochemical markers, organoids were first fixed in 4% paraformaldehyde (PFA) and then permeabilized with Triton-X. If not specified further, every step was performed at room temperature. First, gels were washed by replacing the media with PBS and placing the dishes on a shaker for 10 min. After the first washing step, PBS was replaced by 4 % PFA and placed on a shaker for 15 min. To remove remaining PFA, cells were washed three times with PBS. Permeabilization of the cells was accomplished by treating gels with 0.2% Triton-X in PBS for 10 min on a shaker. Subsequently, gels were washed once with PBS. To block unspecific binding sites, gels were incubated over night at 4°C with 10% donkey serum and 0.1% BSA in PBS. Next, gels were once washed and incubated over night with primary antibodies in 0.1% BSA solution. The different antibodies and their concentration and can be found in Table 3-3. After incubation, gels were washed four times. During that, secondary antibodies were prepared by diluting them 1:250 with 0.1% BSA in PBS (Table 3-4). After washing, gels were incubated for three hours with the secondary antibody solution and if needed phalloidin (Alexa Fluor 633, Thermo Fisher) was added at a ratio of 1:100. Importantly, after addition of the secondary antibody, the fixation proceeded in dark with the samples wrapped in aluminium foil to avoid unintended bleaching. To remove unbound dye and to enhance the resulting contrast, gels were washed four times with PBS. For nuclei labelling gels were incubated for two minutes with 300 nM DAPI (Thermo Fisher), which was followed by four washing steps. Finally, gels were washed 2 times with ddH_2O, carefully transferred to a coverslip and mounted by addition of two drops of Aqua-Poly/Mount (Polysciences, Inc.) on top of each gel. Finally, the gels were sealed with a coverslip and were left to dry over night at room temperature. Labelled samples were stable for several weeks.

Table 3-3: *Primary antibodies used for immunostaining.*

Epitope [Clone]	Conjugation	Host	Dilution	Catalog number	Supplier
alpha smooth muscle actin	-	Rabbit	1/100	ab5964	Abcam, Cambridge, UK
E-cadherin [HECD1]	-	Mouse	1/100	ab1416	Abcam, Cambridge, UK
Gata3 [L50-823]	-	Mouse	1/250	CM405	Biocare Medical, Concord, US
Ki67	-	Rabbit		ab15580	Abcam, Cambridge, UK
Laminin	-	Rabbit	1/100	L9393	Sigma, Steinheim, Germany
P63 [EPR5701]	-	Rabbit	1/300	ab124762	Abcam, Cambridge, UK
Phalloidin	Atto 647	-	1/250	65906	Sigma, Steinheim, Germany
MMP9 [56-2A4]	-	Mouse	1/100	ab58803	Abcam, Cambridge, UK
Integrin α6 [GOH3]	-	Rat	1/100	sc-19622	Santa Cruz, Dallas, US

Table 3-4: *Secondary antibodies used for immunostaining.*

Host/Isotype	Species reactivity	Conjugation	Dilution	Catalog number	Supplier
Donkey/IgG	Mouse	Alexa 488	1/250	A-21202	Life Technologies, Darmstadt, Germany
Donkey/IgG	Rat	Alexa 488	1/250	A-21208	Life Technologies, Darmstadt, Germany
Donkey/IgG	Rabbit	Alexa 546	1/250	A-10040	Life Technologies, Darmstadt, Germany

3.2.4 Live-cell imaging

For live-cell imaging microscopes were equipped with an on-stage incubation chamber (Ibidi, Fig. 3-2A). Within the chamber the temperature was kept at 37 °C. To prevent condensation the bottom plate was heated to 37°C, while the lid was held at 40°C (Fig. 3-2B). Further, the atmosphere was enriched with 5 % CO_2 and replaced with N_2 to ensure a constant O_2-level of 3 % (Fig. 3-2C).

For 2D live cell imaging a Leica DMI8 epifluorescence microscope (Leica Microsystems) was used. Cells were imaged using phase contrast by illuminating the samples with white light and an exposure time of 300 msec. Images were acquired every 10 mins, while the experimental duration varied in-between the experiments. In order to create a large field of view without discriminating resolution, the area of interest was divided into several smaller images and acquired with a HC PL FLUOTAR L 20x/0.40 dry objective. Neighbouring images had an overlap of 10%. Stitching of the individual images resulted in a field of view spanning several millimetres with a resolution of 0.325 µm/px.

For 3D live cell imaging a Leica SP8 scanning confocal microscope (Leica Microsytems) was used equipped with a HCX PL APO 10x CS with a NA of 0.40 and a working distance of 2.20 mm. If not stated other, brightfield imaging was conducted simultaneously with imaging labelled nuclei and fluorescent beads within the ECM. In order to label the nuclei, three hours prior to the experiments, cells were labelled with 10 µM SiR-DNA (Spirochrome). Sir-DNA was excited at 638 nm and its emission maximum was collected between 654 nm and 694 nm. Fluorescent beads were excited at 488 nm and their emission was collected between 500 nm and 540 nm. The combined light of the excitation was used to image the bright field channel. The time between each frame was set to 10 min with a scanning speed of 400 Hz. To reduce the signal-to-noise ratio the line average was set to 2. Distance between the slices was defined to 10 µm.

For immunostainings and visualization of fluorescent collagen the confocal microscope was equipped with either a HC FLUOTAR L 25x W VISIR with a NA of 0.95 and a working distance of 2.5 mm or a HC PL APO 40x CORR CS2 with NA of 1.1 and a working distance of 0.65 mm. Collagen was either fluorescently labelled with Atto 488 or the reflected signal of single fibers was detected using confocal reflection microscopy. In both cases the samples were illuminated with 488 nm. For the reflected signal, the HyD detector collected light between 483 nm and 493nm, while for the fluorescent collagen the detection range was set between 493 nm and 520 nm. The antibodies used for immunostaining are listed in Table 3-3 and 3-4. For high-resolution images a software-implemented adaptive deconvolution algorithm called Lightning (Leica microsystems) was used, pushing the confocal resolution to about 100 nm (Lightning module).

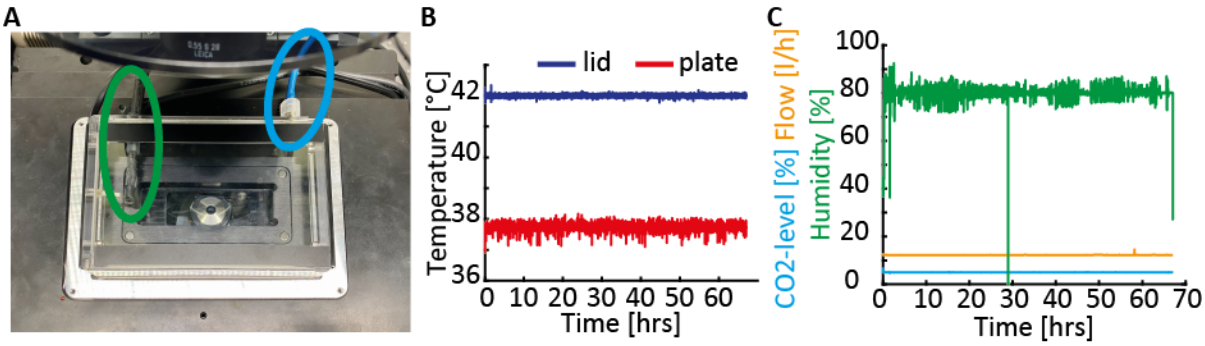

Figure 3-2: **A** Picture of the ibidi incubation chamber on the confocal microscope with the gas inlet (blue circle) and humidity sensor (green circle). **B** Temperature of the lid and plate during a long-term measurement. Accordingly, inside the chamber the resulting temperature was kept around 37 °C. **C** Time development of the CO_2-level, the flow and the humidity.

3.2.5 Laser ablation

To probe the mechanical cell-ECM interactions of growing organoids, laser ablation of the ECM in front of invading branches was conducted. All experiments were performed in collaboration with Marion Raich[58]. Therefore, a custom-made nano-dissection setup was used. Cuts within the collagen network were performed by focusing a pulsed UV-laser with a wavelength of 355 nm and a pulse duration of 400 psec successively 20 µm in front of the branch until a cut with a width, height and thickness of 100, 30 and 1 µm resulted. The laser had a peak power of 72 kW and exhibited an average power of 25 mW. For cutting a HC PL APO 40x/1.10 water objective (Leica microsystems) with a working distance of 0.65 mm was used. For live-cell imaging, the setup was additionally equipped with a spinning-disc unit (CSU-X1, Yokogawa), an Andor NEO sCMOS camera as well as two lasers with a wavelength of 488 nm and 638 nm (Cobolt). The cutting process was recorded with a frame rate between 120 fps and 200 fps. Finally, the resulting movies were analysed with ImageJ. In particular, the branch tip was tracked manually to investigate the relaxation behaviour of the branches. The resulting relaxation curves were then averaged.

3.3 Data analysis

3.3.1 Drift correction

Prerequisite for a proper organoid growth is the cultivation of cells within freely floating collagen gels. During live-cell imaging over long time periods and simultaneous imaging of several position this requirement can lead to a substantial drift of the gels and thus the field of view. The drift is further enhanced by the growth of the organoids which distinctly contract the collagen gel during their expansion, which ultimately even leads to a macroscopic shrinkage of the gel. Thus, prior to bead detection and tracking the stacks needed to be corrected in all three dimensions. Therefore, a 3D drift correction was developed written in Matlab in cooperation with Lev Ushakov within the scope of his Bachelor thesis[59].

In short, the drift correction is divided into two main functions: 1) the function *makeMovie()*, which corrects the stacks in *xyz* using a correlation maximization and 2) the function *makeTiff()*, which saves the corrected data into a new file for the subsequent bead tracking. Before running the function *makeMovie()* several input parameters need to be defined by the user. First, the *z*-slice z_j at the end timepoint in which the organoid is in focus needs to be defined. Further, the correlation threshold between the consecutive time points below which the drift correction shall start needs to be set. For the correlation threshold normally a value of 0.8 was defined, a value of 1 would refer to an utter correlation. Finally, the values *pixRed* and *pixRange* need to be set, which refer to the shift of the images to find the best correlation value. The parameters highly depended on the experiments and the magnitude of the drift. For small drifts values of *pixRed* = 30 and *pixRange* = 10 were sufficient. With those parameters set the drift correction can start to calculate the drift correction. Therefore, the correlation between two last timepoints t_i and t_{i-1} from the slice of the focus are loaded and the correlation *r* between both images is calculated *via* the formula

$$r = \frac{\sum_m \sum_n (A_{mn} - \bar{A})(B_{mn} - B)}{\sqrt{(\sum_m \sum_n (A_{mn} - \bar{A})^2)(\sum_m \sum_n (B_{mn} - \bar{B})^2)}} \tag{3-1}$$

where *A* and *B* refer to the images. The subscript indices *m* and *n* denote the pixels within the image. If the calculated correlation value is higher than the threshold, no correction is necessary and the next timepoints t_{i-1} and t_{i-2} are compared. Yet, when the correlation value is below the threshold the drift correction commences. Therefore, the image of timepoint t_{i-1} gets cropped by the value of *pixRed* and moved in *xy*-direction by the value of *pixRange*. Accordingly, the value of the pixel reduction always needs to be higher as the value for the pixel range. From there on the image gets iterative overlayed on the image of timepoint t_i and the correlation value gets calculated for each translation. Once all positions are measured, the maximal correlation value is displayed. If the value is higher than the threshold the new position is saved and the next timepoint gets compared. Otherwise, the whole procedure is repeated for the slices z_{j-1} and z_{j+1} until a sufficient correlation value is found. All maximal correlation values, their *xy*-positions and *z*-slices are saved and then used from the function makeTiff() to save a corrected stack saved as .ometiff and a time lapse movie of the organoid growth saved as .avi.

3.3.2 Bead tracking and deformation field analysis

In order to analyse the ECM deformation in detail the fluorescent beads embedded in the collagen matrix were detected, tracked over time and subsequently analysed in dependency on their position to the branch. The bead detection and tracking algorithm was developed in cooperation with Pablo Fernández and written in Matlab.

First, fluorescence images of the bead channel were masked by an intensity threshold to reduce the background within the images. Then, individual beads were detected by calculating the centre of an interpolated intensity grid. Hereby, points below or above the bead diameter were neglected, as well as beads touching the image boundary. To guarantee a precise bead

tracking also neighbouring beads in too close proximity were ignored. Finally, the bead positions at all timepoints were matched to conduct the tracking. In particular, an iterative nearest-neighbour approach in three consecutive images was used. Subsequently, the tracking data was further processed in Matlab. Hereby, one measure to demonstrate the highly nonlinear deformations is the cumulative displacement. For the calculation only beads in the near field and in extension of an elongating branch are taken in account, as the displacement appears to be dependent on the distance from the branch and the angle of the branch axis. Over time, the displacements of the beads within the region of interest are added up and finally averaged to display a single curve.

In addition to the bead tracking, the temporal development of the branch tip was measured. Therefore, the open-source program *CellTracker*[60] was used. Tips were tracked manually for each experiment. During this analysis, also the length and main axis of the growing branches were manually defined.

3.3.3 Optical flow analysis

In order to analyse the internal cellular dynamics, cell migration was analysed utilizing an algorithm based on optical flow. The code was written in Python and developed in cooperation with Franz Hutterer.

First, the slices of the nuclei channel of the raw data were z-projected, which resulted in a single movie showing the internal dynamics in time. To reduce the background signal, first pixels below a bit value of 40 were set to zero and second a median filter was applied to the images. Subsequently, the branches of interest, their branch axis and their elongation direction were defined manually by defining start and end position of a branch. These positions were used to extrapolate a linear branch axis. Finally, the flow field within the branches was calculated by a Farnebäck algorithm. Due to the earlier defined branch axis the resulting velocities were split in a parallel and orthogonal velocity component v_P and v_O. As a result, for each timepoint and for each position within the branch the parallel and orthogonal velocity can be plotted. To display the temporal development of the internal velocity the histograms of the velocity distribution of each time point were color-coded, thus plotted as line and then joined together as kymograph. To resolve the migration field spatially, the velocities in a line orthogonal to the branch axis were averaged, color-coded and plotted against their position within the branch. Conclusively, a spatiotemporal visualization of the velocity development resulted. Both analyses were done separately for the parallel and orthogonal velocity component.

To further judge the migration behaviour of cells within organoid branches, a parameter describing the directionality of migration was introduced. The directionality was then defined as:

$$Directionality = \frac{v_P}{v_O} \tag{3-2}$$

Hereby, a value of 1 refers to undirected cell migration without a preferred migration direction and a higher or lower value to a directed migration in either the parallel or orthogonal direction.

For analysing the correlation between the deformation field and the internal cell migration, the analysis was adapted, and the calculation of the optical flow was extended. First, both the bead and the nuclei channel were *z*-projected and ultimately merged into a single channel. Second, two regions for the flow calculation were defined: 1) the branch, only including the fluorescent nuclei and 2) the region in the near field of the branch, only including the fluorescent beads. As a result, the qualitative ECM displacement as well as the signed averaged internal cell velocity was plotted against the time and finally correlated.

In 2D cell assays, the level of confluency was also calculated based on the optical flow data. As the contribution of the cell-free background to the optical flow was removed by applying a threshold, only areas covered by a cell were detected. In particular, the optical flow of the background was set to zero. As a consequence, the confluency was calculated by the following equation:

$$Confluency = \frac{(Number\ of\ pixels\ \neq 0)}{(Total\ number\ of\ pixels)} \tag{3-3}$$

Hereby, the total number of pixels refers to the image size. The resulting level of confluency varied between 0 and 1, where 0 refers to no cells present in the field of view and 1 to a confluent cell layer.

3.3.4 Collagen network analysis

Collagen fibre alignment was characterized using the ImageJ plugin *OrientationJ*. With that, the distribution of individual fiber angles was measured. Using Matlab, a gaussian was fitted to the distribution and the according full width half maximum (FWHM) was calculated. Then, the degree of alignment was defined as:

$$degree\ of\ alignment = \frac{(FWHM_{max} - FWHM)}{FWHM_{max}} \tag{3-4}$$

Hereby, the maximal FWHM is a fixed value and refers to the highest measured FWHM throughout all measurements. Consequently, the degree of alignment can vary between 0 and 1, where 0 refers to a random oriented and 1 to a fully aligned collagen network.

In order to measure the properties of the collagen cage, the fluorescent signal of the collagen network around growing branches was analysed using ImageJ. The collagen density was characterized on basis of the fluorescence intensity at the cell-ECM boundary, the invasion site and in the far field. Therefore, boxes with a size 5 µm x 5 µm were defined in the according areas and their mean fluorescence intensity was calculated. Subsequently, the intensity was normalized by the maximal measured intensity value. The higher the ratio, the denser the collagen accumulation. To calculate the cage width, the fluorescence signal within a box

covering the organoid, the cage and the far field was plotted. The dimensions of the box were always set to a height of 1 µm and a width of 35 µm. Then, the cage width was defined as the length in which the fluorescence signal was at least 40 % higher than in the far field.

4 Nonlinear and plastic mechanical properties of biomimetic hydrogels

With the onset of 3D cell culture and the concomitant establishment of different organoid assays the search for hydrogels mimicking the extracellular environment *in vivo* has become a topic of intense research[3,4,61]. Hereby, collagen I networks have become a major choice as ECM, due to their abundant occurrence *in vivo* and thus good cell compatibility as well as the easy preparation. Likewise, the protein mixture Matrigel which is derived from Engelbreth-Holm-Swarm mouse sarcoma cells has become a well-established hydrogel[62]. In addition, artificial polymer hydrogels based on for example alginate, polyacrylamide or polyethylene glycol have been utilized in various cell and organoid assays[63–65]. Their major advantage is exhibited in their mostly tuneable mechanical and biochemical properties. Yet, their usage is limited by their elaborate preparation as well as by their restricted cell compatibility. Consequently, most common collagen, Matrigel or hydrogels thereof are used for 3D cell and organoid cultivation.

Although, collagen I and Matrigel are commonly used and even mixed, their biochemical, structural and mechanical properties differ drastically. Due to preparation of Matrigel from cultivated tumour cells, its composition and thus biochemical milieu always differs between different preparation batches[62]. Thus, a precise comparison between different studies is complicated. However, its major structural components are laminin, collagen IV and entactin[66,67]. Further, Matrigel is enriched with various growth factors as well as metalloproteinases in varying concentrations, which highly affect cell proliferation and migration[62]. To enhance comparability in-between different preparations, an explicitly growth-factor reduced Matrigel must be purchased. In contrast, hydrogels derived from collagen I exhibit a precise and always the same biochemical milieu as the preparation solely relies on a single component.

Further, the different biochemical composition of Matrigel and collagen I hydrogels results in differing network structures[68]. Collagen polymerizes into fibrillary matrix with well-defined mesh size[69]. The individual fibres build an entangled network and form bundles and crosslinks between each other. The network structure can be precisely modulated by pH-value, temperature and polymerization rate during the polymerization[69,70]. For instance, collagen polymerized at 22 °C forms thicker bundles with larger pores compared to collagen polymerized at 37 °C. Similar, fiber thickness significantly reduces with increasing pH-value. In contrast, Matrigel polymerizes into a fine-meshed sponge-like network, in which entactin acts as crosslinker between laminin and collagen IV[68,71]. The resulting pore size is below the order of a micron and thus distinct smaller than the common cell size. Yet, the structure of collagen-Matrigel scaffolds is just poorly characterized.

Further, the differing compositions and network architectures result in a different mechanical response function. Despite their relevance in 3D cell and organoid culture assays, their mechanical characterization is mainly limited to the linear regime, while their nonlinear

response is often neglected[72,73]. A comparison of the different hydrogels is further complicated, as there is no standardized rheological characterisation protocol testing the nonlinear and plastic properties of commonly used hydrogels. Especially for Matrigel, the mechanical characterization in literature is limited to the linear regime. Matrigel exhibits a purely linear response function, revealed by frequency and strain sweeps[72]. In contrast, the linear as well as nonlinear behaviour of collagen I networks is described in more detail in literature. Within the linear regime, frequency sweeps of collagen networks reveal a moderate increase of the storage and loss module at high frequencies above 10 Hz[72]. In order to characterize the nonlinear behaviour most commonly cyclic strain amplitudes are applied on the network, while the stress-strain relation is measured. Hereby, collagen reveals a characteristic strain-stiffening and Mullins-softening[74,75]. For small strains the stress within the collagen network increases linear. With further increasing strain the stress increases steeper, demonstrating a stiffening of the network. Remarkably, when the same collagen network is sheared with the same shear rate a second time, this onset of stiffening is shifted to higher strains, indicating a softening of the material. This behaviour is similar to the Mullins softening observed for rubber and actin networks and is the result of a plastic fibre lengthening and buckling as well as the breakage and formation of weak crosslinks[11,75–77]. Yet, the phenomena are mainly characterised qualitatively and not quantitatively, which complicates a proper comparison between different hydrogels. For Matrigel such a nonlinear characterization is completely missing.

In recent cell and organoid studies the nonlinear and plastic properties of the matrices have been demonstrated to steer the cellular behaviour[5,11,33]. However, collagen, Matrigel and hybrid gels thereof are still used without further notice of their differing mechanical response. In this chapter, the linear and nonlinear mechanical properties of hydrogels composed of collagen I, Matrigel and hybrid gels of both components are characterized by bulk rheology and subsequently compared. In particular, the predominantly linear mechanical response of pure Matrigel is contrasted to the highly nonlinear and plastic response of collagen. Further, the mechanical tunability of hybrid gels derived from Matrigel and collagen gels is demonstrated. As a result, nonlinear and plastic effects reduce in hybrid gels with increasing Matrigel concentration. By the use of fluorescent collagen, the varying polymerization dynamics of collagen in the presence of Matrigel is demonstrated and the mechanical response of the different hydrogels is linked to the underlying network structure.

4.1 Structure analysis

Prior to the mechanical characterization of the hydrogels, collagen polymerization and network structure were analysed in the presence of varying amount of Matrigel (Fig. 4-1A). By the use of fluorescent collagen, the resulting network structure was imaged, and the related pore sizes were measured. As a consequence of the fluorescent labelling of unpolymerized collagen, no signal was detected in the sample of 100% Matrigel as here the network was not

enriched with fluorescent collagen. Further, it proves that the imaged collagen network only relates to conjugated collagen I and not to collagen present in the Matrigel solution.

Pure collagen networks with a collagen concentration of 1.3 mg/ml polymerize into a fibrillary matrix in which individual collagen fibres entangle with several other fibers and form crosslinks throughout the whole network. The resulting mean pore size is around 38 µm^2 (Fig. 4-1B). In hybrid gels consisting of collagen and 25% Matrigel individual collagen fibers appear to be smaller and denser distributed within the network yet are still clearly visible. In such hybrid gels, the mean pore size reduces to around 23 µm^2 (Fig. 4-1C). Within hybrid gels of collagen and 50 % Matrigel individual collagen fibers only polymerize into small fragments, which are too short to exhibit an entanglement of individual fibers. Here, the mean mesh size reduces to 10 µm^2 (Fig. 4-1D). In some studies, it is suggested to let collagen preassemble for two hours at neutral pH-value and at 4°C, prior to mixing it with Matrigel[78]. This procedure

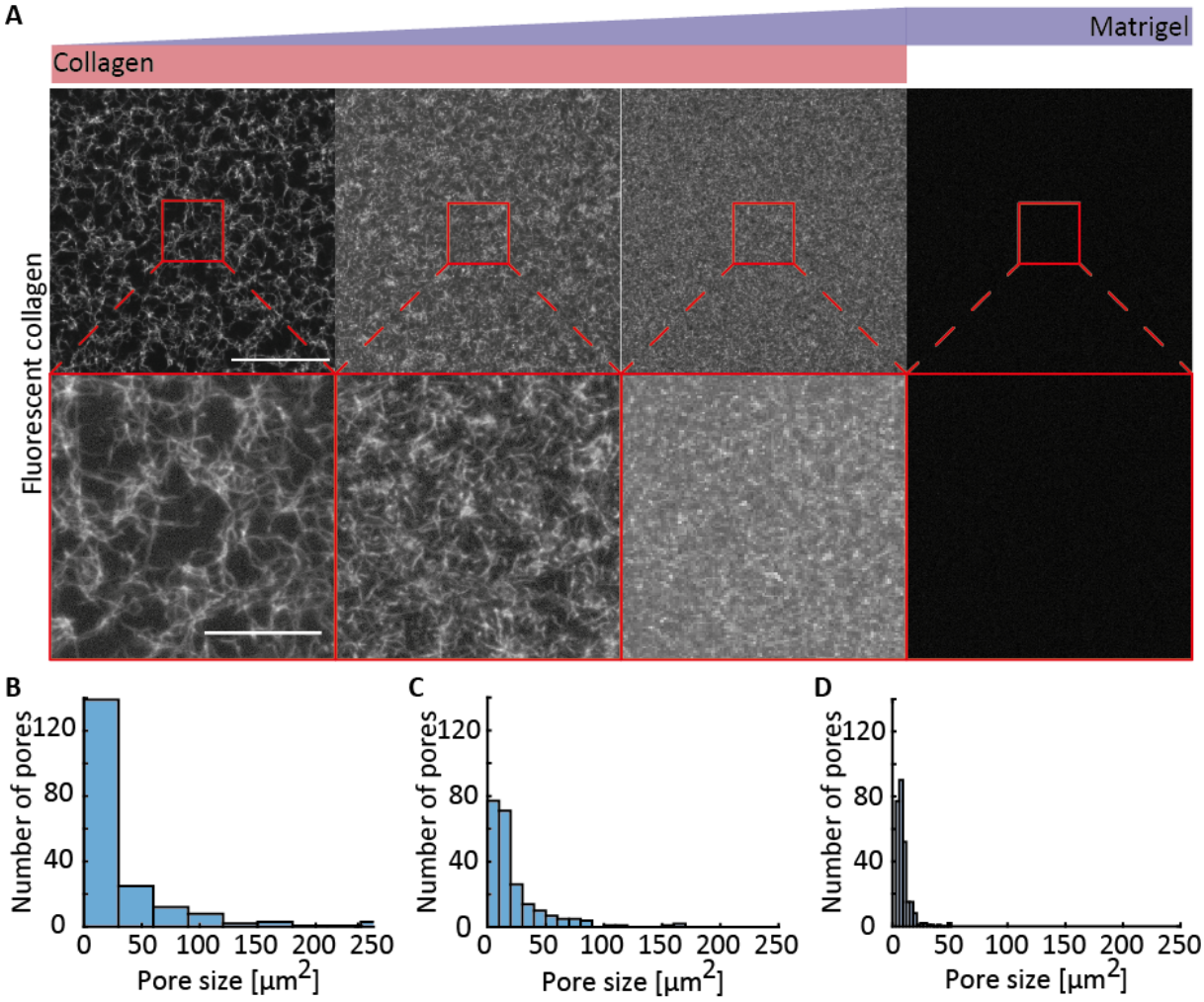

Figure 4-1: Structure analysis of the studied hydrogels. A *Collagen network structure in dependency of Matrigel concentration, unraveled by fluorescent collagen. Pure collagen (far left) exhibits a fibrillary matrix with defined mesh size. Within hybrid gels enriched with 25% Matrigel (middle left) collagen fibers shorten, and the pore size reduces. An increase in Matrigel to 50% (middle right) leads to a further shortening of individual collagen fibers. Within 100% Matrigel (far right) no fluorescent collagen is present.* ***B-D*** *Distribution of collagen pore sizes for (**B**) pure collagen, (**C**) collagen enriched with 25% Matrigel and (**D**) collagen enriched with 50% Matrigel. In all cases collagen concentration is 1.3 mg/ml. Scale bars, 50 µm (**A**, overview), 20µm (**A**, zoom in).*

shall improve collagen polymerization in the presence of Matrigel. However, after polymerization of the hybrid gels no significant difference in the collagen network compared to the pure mixing of the matrix components is detected.

Summarising, the mixing of collagen and Matrigel prior to polymerization induces distinct changes in the collagen network structure. With increasing amount of Matrigel, the collagen pore sizes stepwise reduce and the fiber length clearly shortens. Thus, the network structure of the hybrid gels cannot be solely described as sum of the individual networks but need to be analysed separately.

4.2 Linear mechanical properties

Subsequent to identifying structural differences of the collagen network in dependency of Matrigel concentration, the polymerization dynamics were monitored (Fig. 4-2). To this end, continuous oscillations were applied to the different hydrogels, while simultaneously polymerization was induced by heating the lower plate from 4 to 37 °C. During this process the storage moduli *G'* of the hydrogels were measured. Hereby, the onset of polymerization is characterized by an increase in the storage module. Once the storage module equilibrates, the networks are fully polymerized. While Matrigel starts to polymerize approximately 30 sec after heating the lower plate, polymerization of pure collagen is delayed by additional 30 sec. In both cases, it takes around 35 sec until *G'* starts to equilibrate. However, the polymerization curves of hybrid gels do not mimic the polymerization of either collagen or Matrigel but exhibit their own characteristic. In hybrid gels, *G'* is not equilibrating in the time course of 300 sec but is raising steadily. Thus, the mixing of collagen and Matrigel is impairing the individual network polymerization and thereby delaying the overall polymerization dynamics. Ultimately, this leads to the formation of distinctive networks, as seen in the structure analysis.

After successful polymerization, the linear mechanical properties of the hydrogels were measured. This characterization is achieved by measuring the frequency-dependent storage module *G'(f)* and loss module *G''(f)* by conducting frequency sweeps from 0.01 to 60 Hz. For frequencies ranging from 0.01 to 10 Hz *G'* and *G''* of pure collagen exhibit a steady plateau (Fig. 4-3A). At higher frequencies, *G'* and *G''* slightly increase. This increase manifests in

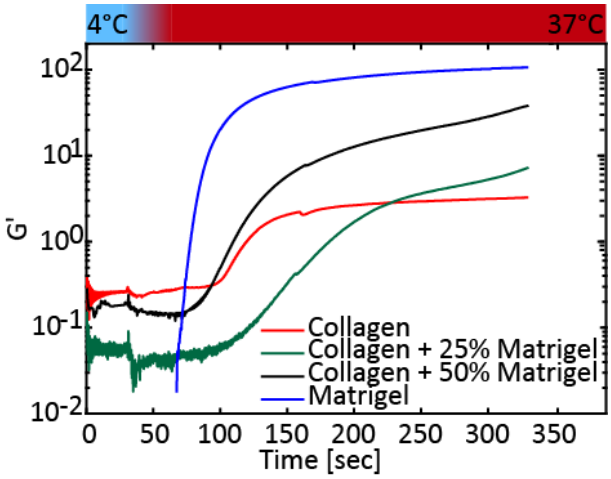

Figure 4-2: Polymerization dynamics of the studied hydrogels induced by temperature. *In contrast to pure collagen, 100% Matrigel exhibits a fast polymerization shortly after the sample is heated. Hybrid gels of collagen and Matrigel show an overall slower polymerization compared to pure gels.*

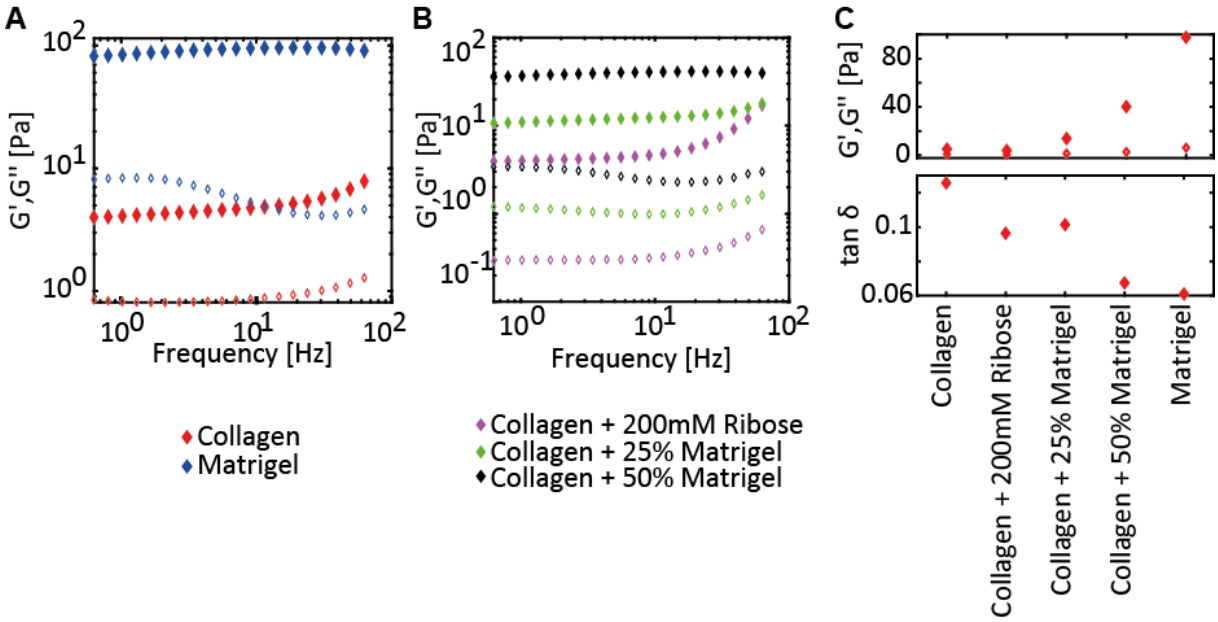

***Figure 4-3: A, B** Frequency sweeps of (**A**) collagen and Matrigel and (**B**) related hybrid gels. **C** Storage and loss module and according phase angle measured at 1 Hz.*

collagen gels crosslinked with 200 mM Ribose. In comparison, in hybrid gels of collagen and Matrigel this increase gets stepwise diminished with increasing Matrigel concentration (Fig. 4-3B). Networks composed of 100% Matrigel show a predominantly constant *G'*, while G'' reduces at frequencies larger than 2 Hz (Fig. 4-3A). However, in all studied hydrogels *G'* is dominating *G''*, underlining the gel-like characteristics of each hydrogel. Further, the predominantly linear dependency highlights no intrinsic timescale for remodeling processes within the linear regime.

In order to compare the linear stiffness of the studied hydrogels a plateau modulus $G_0 = G'(1$ Hz*)* is defined. As a result, distinct differences between the studied hydrogels become apparent and highlight the different capabilities to store energy within the linear regime (Fig. 4-3C). Of all hydrogels, pure collagen (1.3 mg/ml) exhibits the lowest storage module which is measured to be 4.9 Pa. By crosslinking collagen using 200 mM Ribose the network gets more resistant against linear deformations and thereby increases the storage module to 6.4 Pa. Also, in hybrid gels of collagen and Matrigel the storage module increases significantly in comparison to pure collagen. Addition of 25 % Matrigel to collagen leads to an increase to 12.4 Pa, while the addition of 50 % Matrigel leads to a further increase to 32 Pa. Of all studied hydrogels pure Matrigel exhibits the largest storage module of 97.6 P and is thereby almost 20 times higher than the storage module of pure collagen.

To further compare the interaction of the components in hybrid gels, their individual moduli were probed. Subsequently, the individual moduli were added and compared to the real moduli of the hybrid gels. For 25 % Matrigel only the storage and loss module are G' = 1.4 Pa and G'' = 0.13 Pa. Accordingly, the cumulative moduli add up to $G'_{25\%+Collagen}$ = 6.4 Pa and $G''_{25\%+Collagen}$ = 0.73 Pa, while the moduli of the hybrid gels are $G'_{hybrid\ 25\%}$ = 14 Pa and $G''_{hybrid\ 25\%}$ = 1.4 Pa. For 50 % Matrigel only the moduli are G' = 19 Pa and G'' = 1.2 Pa and add up to $G'_{50\%+Collagen}$ = 24 Pa and $G''_{50\%+Collagen}$ = 1.33 Pa. In comparison, the related moduli of the hybrid gels are $G'_{hybrid\ 50\%}$ = 40 Pa and $G''_{hybrid\ 50\%}$ = 2.6 Pa. Consequently, all studied hybrid gels exhibit

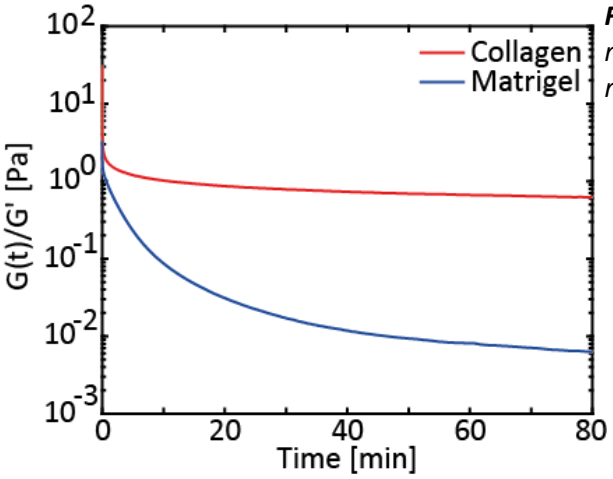

Figure 4-4: *Strain jump experiments contrasts fast relaxation dynamic of pure collagen to slow relaxation of Matrigel.*

higher moduli as the sum of the individual gels, indicating a symbiotic strengthening of both components.

In addition to the plateau moduli the phase angle $\tan\delta$ is a further possibility to reveal differences in the viscoelastic behavior of different hydrogels (Fig. 4-3C). Specifically, a higher phase angle corresponds to a higher fluidity respectively lower viscosity. Of all studied hydrogels pure collagen exhibits the largest phase angle, indicating the lowest viscosity. Similar to the plateau module, the phase angle of collagen networks can be tuned either by treatment with Ribose or by enrichment with Matrigel. In all cases a treatment leads to a more viscous material. Collagen networks crosslinked with 200 mM Ribose and hybrid gels consisting of collagen and 25 % Matrigel result in nearly the same phase angle respectively viscous behavior. An enrichment of collagen with 50 % leads to a further increase in the phase angle, which approaches the absolute value of pure Matrigel. Compared to pure collagen the phase angle of Matrigel lowers from 0.13 to 0.61. According to the difference in the phase angle, additional strain jump experiments of pure collagen and Matrigel were conducted to test the relaxation behavior of both materials (Fig. 4-4). Here, collagen exhibits a nearly instantaneous relaxation, which equilibrates at a residual stress. In contrast, Matrigel approaches nearly zero stress in the time course of more than 80 mins.

Together, the results highlight the differences of the hydrogels in the linear regime. Compared to Matrigel, collagen is a softer hydrogel with a higher fluidity. A stepwise addition of Matrigel to collagen networks leads to stepwise convergence of the linear properties to those of Matrigel. However, strain jump experiments indicate differences in the nonlinear behaviour of collagen and Matrigel, which will be further examined in the following chapters.

4.3 Nonlinear mechanical behavior

So far, the linear properties of the studied hydrogels have been the focus of the study. However, cell invasion and branching morphogenesis in three-dimensional matrices are accompanied by nonlinear and plastic remodeling processes, far beyond the linear mechanical regime. Consequently, cyclic $\dot{\gamma}$-pulses with increasing strain amplitude were conducted to probe the nonlinear properties of the studied hydrogels.

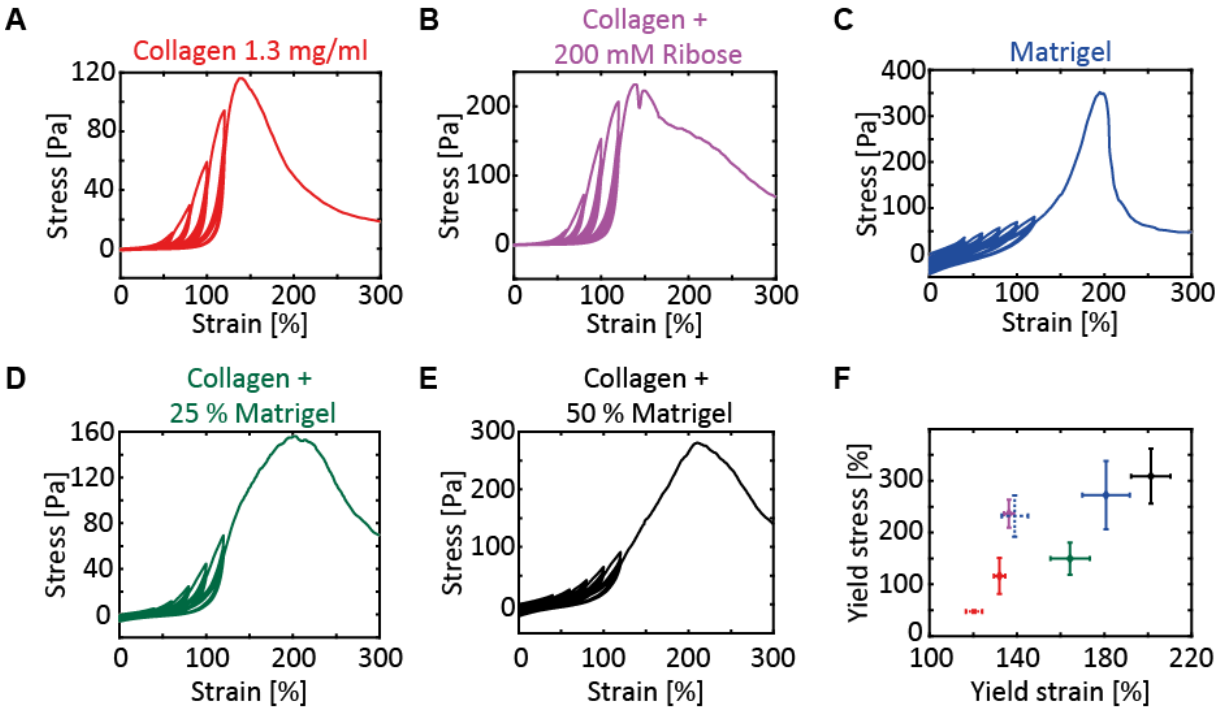

***Figure 4-5: A-E** Strain-stress relation of (**A**) collagen, (**B**) Matrigel, (**C**) Collagen treated with 200 mM Ribose and hybrid gels of collagen enriched with (**D**) 25 % Matrigel and (**E**) 50 % Matrigel. **F** Yield strain and stress of the studied hydrogels. The dotted lines refer to the yield strain and stress of collagen and Matrigel networks that were not cyclic sheared. Colors refer to the colors used for the according strain-stress relations.*

During cyclic loading the highly nonlinear mechanical response of collagen networks becomes apparent (Fig. 4-5A). For small strains the stress increase is linear with only a small slope, highlighting its soft linear response. However, within the first cycle at strain amplitudes higher than 20 % the stress steeply increases, resembling the nonlinear regime and the characteristic strain-stiffening of collagen. With increasing cycle number, the onset of strain-stiffening is shifted to higher strains. As a consequence, the linear regime extends, which leads to a softer material until the nonlinear regime is reached again. With increasing strain amplitude, the network reaches higher stresses, but exhibits the same characteristic strain-stiffening and the related cyclic shift. This characteristic nonlinear behavior is conserved in collagen networks treated with Ribose (Fig. 4-5B). In comparison to pure collagen, higher stresses are achieved as the crosslinks partly prevent a network remodeling. In contrast, Matrigel exhibits a predominantly linear mechanical response (Fig. 4-5C). Up to 30 % strain of the firs cycle the stress linearly increases with a larger slope than in collagen networks, highlighting its stiffer mechanical response. At strains above 30 % a slightly steeper increase in the stress can be observed, resembling the nonlinear regime of Matrigel. With each cycle the stress at 0 % strain decreases noticeably, displaying the slow relaxation dynamic respectively the plastic-viscous loss of Matrigel. Overall, Matrigel reaches the highest stresses. Hybrid gels consisting of collagen and 25 % Matrigel exhibit diminished characteristic of pure collagen networks (Fig. 4-5D). However, strain-stiffening as well as a cyclic softening for small strains can still be observed. Further, the addition of 25 % Matrigel leads to an increase in the measured stress. By increasing Matrigel amount to 50 %, the characteristic strain softening gets further

diminished and the predominantly linear mechanical response of Matrigel gets reinforced (Fig. 4-5E).

Ultimately, after cyclic testing of the hydrogels their yield strain and stress were probed (Fig 4-5F). Here, pure but cyclic stressed collagen reveals to be the weakest network of all studied hydrogels. The network ruptures at around 132 % strain and 116 Pa stress. By crosslinking the collagen network, the hydrogel strengthens and reaches a more than doubled yield stress of around 237 Pa at 136 % strain. However, enriching collagen with Matrigel further tunes the hydrogel loadability with a marked increase in the yield strain. While hybrid gels of collagen and 25 % Matrigel yield at around 164 % strain and 149 Pa stress, an increase in Matrigel amount to 50 % leads to a rupturing at 201 % strain and 309 Pa stress. Thus, collagen enriched with 50 % yields at the highest strain and stress and thereby results in the most stable hydrogel. Indeed, pure Matrigel already yields at a strain around 180 % at only 272 Pa and establishes in-between the two hybrid gels. Remarkably, collagen and Matrigel networks that were not cyclic sheared but directly tested for their yielding behavior rapture at lower strains and stresses than the same cyclic sheared networks (Fig. 4-5F, dotted crosses). This observation indicates a structural remodeling of the networks upon cyclic strain, which strengthens both networks.

In summary, these observations highlight the distinct differences in the nonlinear mechanical response of the hydrogels and contrast the predominantly linear response of Matrigel to the highly nonlinear characteristic of pure collagen networks. In addition, the difference in the yield strain and stress further emphasizes the possibility to tune the linear and nonlinear properties of different hybrid gels by the use of different amounts of collagen and Matrigel.

4.4 Dissipated work

The stress-strain curves already indicate differences in the loading and unloading curves of the hydrogels, hinting towards structural remodeling processes (Fig. 4-6A, 4-6B). In order to classify the studied hydrogels according to their plastic properties, the strain and cycle dependent dissipated work within the networks is calculated. The dissipated work refers to the combination of viscous loss and plastic remodeling of the network.

At the lowest strain amplitude of 40 % pure collagen, Matrigel and hybrid gels of both components exhibit a similar dissipated work of around 30 %. However, with increasing strain amplitude distinct differences in the dissipation within the hydrogels become apparent and highlight the higher plasticity of collagen networks (Fig. 4-6C). With increasing strain amplitude, pure collagen dissipates an increasing amount of work until at 120 % strain more than 60 % of the work dissipates within the first cycle. By strengthening the collagen network *via* additional crosslinks roughly 20 % less work within each strain amplitude gets dissipated. Yet, the form of overall increase of dissipated work with increasing strain amplitude stays the same. In contrast, within networks derived from Matrigel only around 20 % of the initial work dissipates, independent on the maximal strain amplitude. This behavior is identically

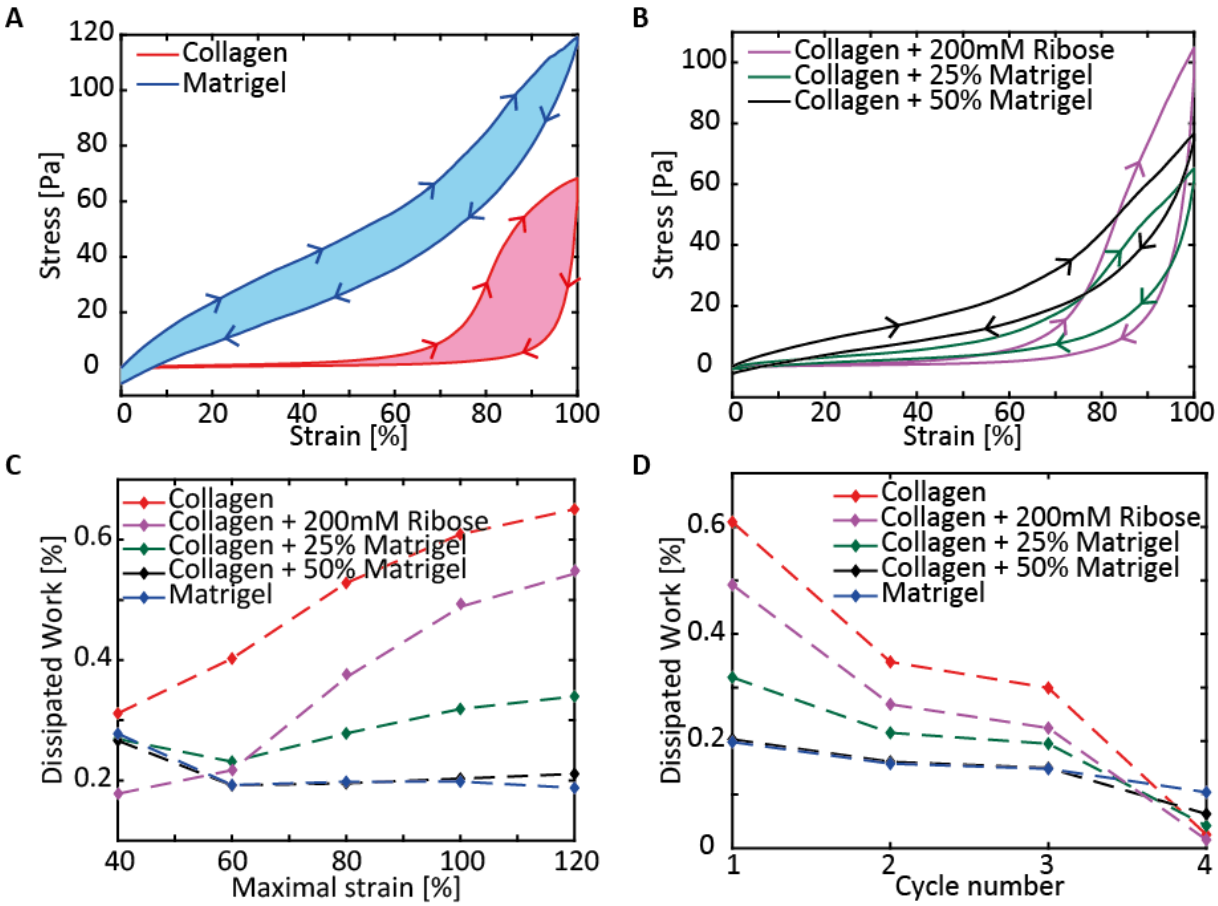

***Figure 4-6: A, B** Loading and unloading curves during the first cycle at 100 % strain for (**A**) collagen and Matrigel and (**B**) related hybrid gels. The filled areas represent the dissipated work within the first cycle. **C** In contrast to Matrigel and hybrid gels, collagen and additional crosslinked collagen exhibit with increase of maximal strain an increase in dissipated work. **D** The cycle dependent dissipated work gradually changes between the hydrogels.*

recapitulated within networks composed of collagen and 50 % Matrigel, which highlights the dominant impact of Matrigel at this mixing ratio as observed during the structure analysis. By reducing the Matrigel amount to 25 %, a diminished increase of dissipation can be observed, similar to the collagen networks. However, in such networks only about 30 % of the initial work dissipates, which is just half of the dissipation observed in pure collagen.

Yet, remodeling processes such as fiber alignment or rapture and formation of crosslinks are not limited to the first cycle but can also occur during later strain cycles. Thus, the cycle dependent dissipated work sheds light on the temporal structural toughness of the material (Fig. 4-6D). Pure and crosslinked collagen exhibit both a steadily decreasing amount of dissipative work until no dissipation can be seen anymore at the fourth cycle. The same but diminished development can be seen in hybrid gels with collagen enriched with 25 % Matrigel. By increasing Matrigel concentration to 50 % the dominant impact of Matrigel on the network properties becomes apparent again. In such networks roughly the same dissipation between 20 and 10 % can be seen independent from the cycle. This behavior is identical to the behavior of pure Matrigel, highlighting the subservient role of collagen in hybrid gels with an increasing

amount of Matrigel. Further, the steady amount of dissipated work throughout all cycles indicates a predominant viscous loss and a minor plastic remodeling.

4.5 Degree of plasticity

Plastic remodeling processes cannot only be characterized by their differences in stress increase and decrease of the loading and unloading curves, but also by their strain and cycle dependent peak stress. As a benchmark, the development of the strain dependent peak stress of the first cycle is calculated in dependency of the maximal strain amplitude (Fig. 4-7A). Here, the peak stress of networks derived from pure Matrigel increases linearly with increasing strain amplitude, starting from 33 Pa at 40 % strain and raising to 95 Pa at 120 % strain. Pure collagen gels as well as hybrid gels of collagen and Matrigel exhibit a slightly exponential increase from 3.8 Pa at 40 % strain to 98 Pa at 120 % strain. As a result of the additional crosslinks and the concomitant increased stability, collagen networks treated with 200 mM Ribose reach the highest peak stress of 180 Pa at 120 % strain, which is almost double as high as the peak stress of untreated collagen networks. However, at small strains crosslinked collagen shows an identical behavior as pure collagen.

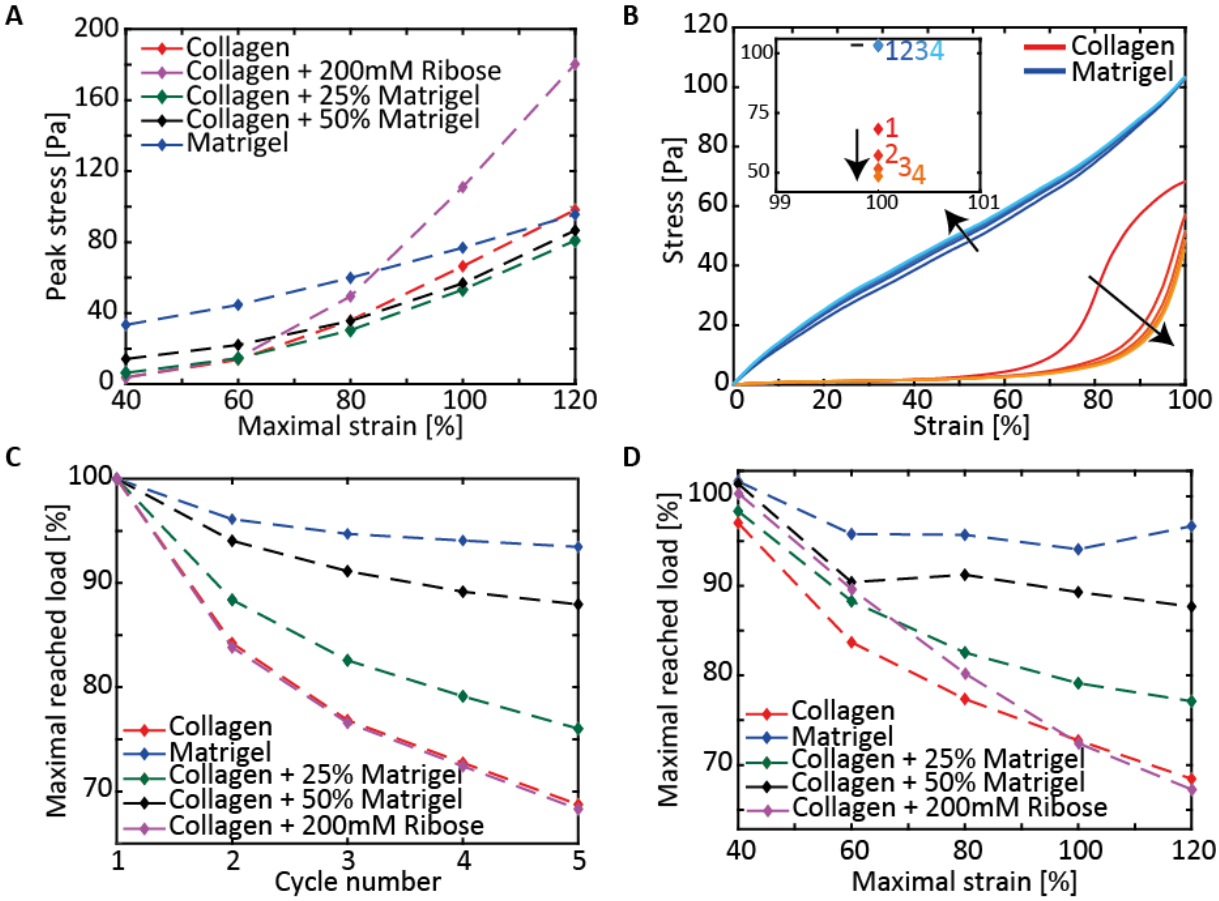

***Figure 4-7: A** Development of the peak stress within the first cycle in dependency of the maximal strain amplitude. **B** Representative corrected strain-stress relation at 100 % strain with according development of the peak stress (inset). **C, D** Maximal reachable in dependency of the (**C**) cycle and (**D**) maximal strain.*

Due to the dissipative work in the loading and unloading curves the peak stress becomes cycle dependent and thus indicates plastic remodeling processes. To exclude viscous effects, each loading curve was shifted to 0 Pa at 0 % strain to ensure a comparability of the peak stresses (Fig. 4-7B). Within the first cycle, pure Matrigel exhibits a major drop of around 5 % of the initial peak stress. This drop is followed by just minor reductions in the following cycles. Hence, after the last cycle the peak stress is in total reduced by around 8 %. In comparison, pure and additional crosslinked collagen networks exhibit a highly pronounced reduction (Fig. 4-7C). After the first cycle, the peak stress just reaches around 85 % of the initial stress and reduces thereby already remarkable more than in Matrigel after five cycles. However, with increasing cycles the peak stress further reduces until it only reaches around 70 % of the initial value at the fifth cycle. It has to be noted that the value of the peak stress did not equilibrate so far, indicating a further possible network remodeling. However, due to the experimental protocol a further prediction is not possible. By the fabrication of hybrid gels of collagen and Matrigel the diverging reduction of both components can be gradually varied. Hybrid gels with only 25 % Matrigel reveal the diminished characteristic of pure collagen networks with an overall reduction of the peak stress of around 25 %. By increasing Matrigel concentration to 50 %, the dominant influence of Matrigel becomes apparent and the overall reduction lowers to around 13 %. Further, such hybrid gels exhibit the formation of a plateau upon the fourth cycle, demonstrating that at later cycles no further remodeling processes occur. This underlines the dominant impact of Matrigel and inferior importance of collagen at this mixing ratio, identical to the structural traits.

In addition to the cycle dependency stress reduction, the maximal plasticity is also dependent on the applied strain amplitude (Fig. 4-7D). At low strains all hydrogels exhibit the same maximal reduction of the peak stress, which is in the order of 5 %. However, with increasing strain amplitude, collagen underlines it higher plasticity compared to Matrigel. In comparison, at 120 % strain and at the fifth cycle collagen only reaches 70 % of the initial peak value, while Matrigel still reaches around 95 %. This remarkable plasticity is also conserved in additional crosslinked collagen networks. Here, at low strains a proportion of the crosslinks withstand the applied stress and thus lead to a smaller plastic remodeling. At higher strains the internal stresses increase so far, that no difference to the pure network is observable. Similar to the cycle dependency, hybrid gels establish in-between pure collagen and Matrigel. Hybrid gels with low Matrigel amounts exhibit rather collagen characteristic, while hybrid gels with high Matrigel amounts mimic pure Matrigel.

According to the above analysis, the higher plasticity of collagen compared to Matrigel becomes apparent. Further, the degree of plasticity demonstrates the tunability of hybrid gels by varying collagen and Matrigel stoichiometry. However, despite collagen crosslinking *via* Ribose and the concomitant higher peak stresses, the degree of plasticity stays comparable to pure collagen networks. This observation is in accordance with simulations focusing on the breakage and formation of weak crosslinks during nonlinear strain experiments[11]. With every cyclic deformation initial crosslinks are broken apart and then formed new at different positions.

4.6 Differential module

In material science and also in cell-ECM studies the stiffness of a material is a key parameter characterising the hydrogel. In general, the stiffness of a material is defined as the quotient of the stress and strain. Within the linear regime the slope is denoted as the Elastic modulus $E = \frac{\sigma}{\gamma}$, which is independent on the strain and stress of the material. However, within the nonlinear regime the premise of the linear relationship between strain and stress does not hold anymore. Thus, the stiffness becomes dependent on the strain and stress and is the denoted as the differential module $K = \frac{\mathrm{d}\sigma}{\mathrm{d}\gamma}$.

Within the first loading curve Matrigel exhibits a purely linear stress increase and thereby a constant elastic modulus. At strain amplitudes higher then 60 % the linear regime is followed by a slight nonlinear response with a minor steeper increase. With increasing strain amplitudes this nonlinearity is conserved, yet the onset is shifted to higher strain amplitudes. For instance, at strain amplitudes of 100 % the differential module is constant until 60 % strain and only slightly increases for higher strains (Fig. 4-8A). Within the second cycle, this onset is shifted to higher strains and the maximal differential module decreases. However, compared

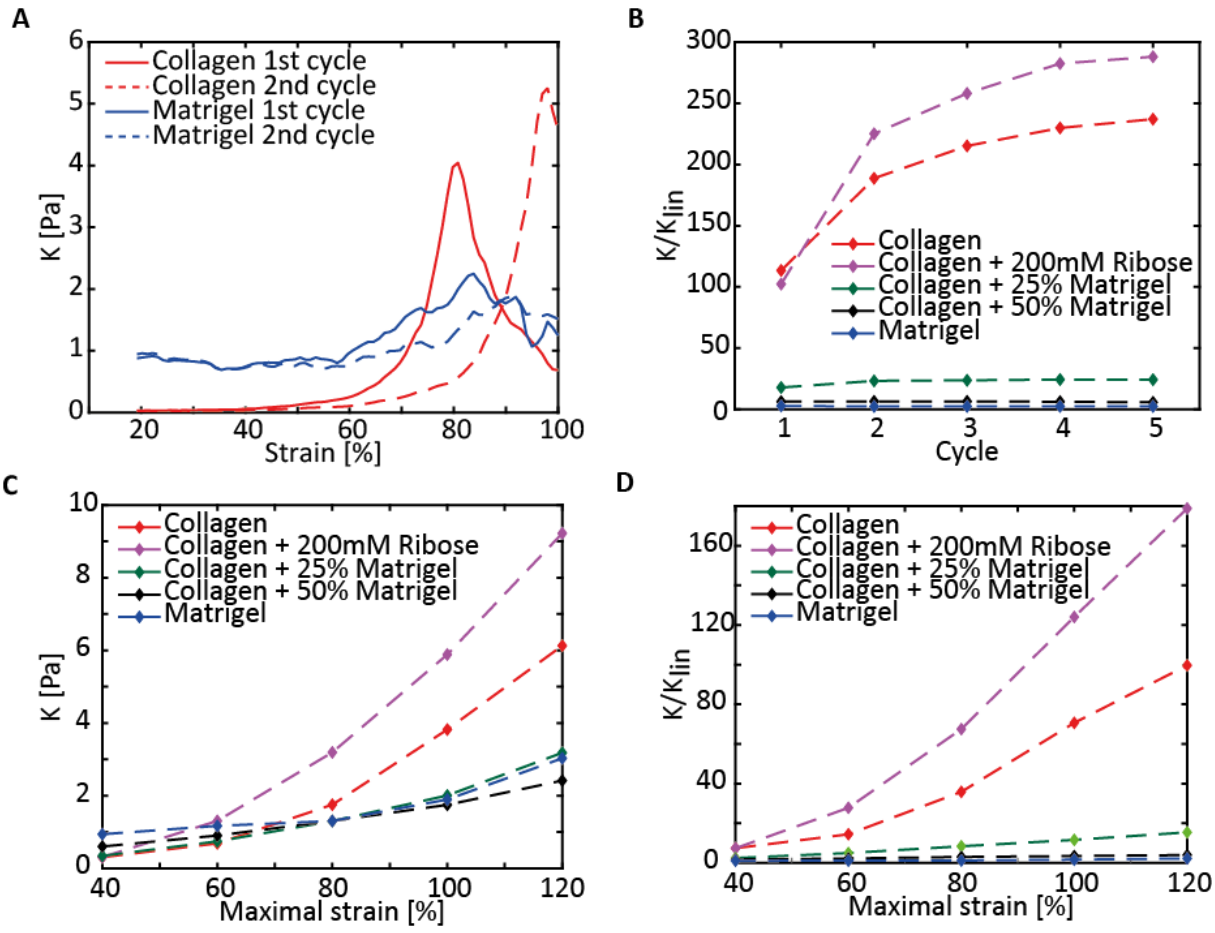

***Figure 4-8**: **A** Strain dependency of the differential module of collagen and Matrigel at 100 % strain. **B** Development of the normalized differential module against the cycle number. **C, D** Strain dependency of the (**C**) differential module and (**D**) normalized differential module.*

to the linear regime the change of the differential module with increasing cycle number is negligible. In comparison, collagen networks reveal a marked nonlinear strain-stress relation already from the first cycle on. As described in chapter 4.3, collagen networks exhibit a strain-stiffening with increasing strain and mimic a Mullins-softening for increasing cycle number[79]. At 100 % strain a linear response can be observed up to roughly 40 % strain, which is then followed by a steep increase in the differential module, highlighting the nonlinear regime (Fig-4-8A). With increasing cycle number, the onset is shifted to higher strains. For instance, at the second cycle the strain-stiffening first occurs at 60 % strain. In contrast to Matrigel, the maximal differential module increases, consequently the network gets stiffer. This behaviour is fully recapitulated in crosslinked collagen networks. While the differential module for pure collagen networks is more than 200 times higher than the linear regime, crosslinked collagen gets nearly 300 times stiffer (Fig. 4-8B). Similar to the previous analysis, hybrid gels exhibit a gradual change between the individual components. Specifically, the value of the differential module can be gradually increased with decreasing Matrigel amount. However, hybrid gels of collagen and 25 % Matrigel only exhibit a 25-fold increase in the differential module and are thereby significantly softer than pure collagen. Further, the differential module stays predominantly constant throughout the cycles and does not exhibit the cycle-dependent increase.

In addition, it has to be noted that the differential module of the first cycle is also dependent on the maximal strain amplitude (Fig. 4-8C). Here, it can be observed that for small strains all studied hydrogels exhibit a differential module in the same order of magnitude and thereby exhibit a comparable stiffness. While for Matrigel and hybrid gels, the differential module increases nearly linear with the strain amplitude, pure and crosslinked collagen exhibit an exponential increase. In particular, crosslinked collagen already increases drastically upon 60 % strain, while the differential module of pure collagen raises exponential upon 80 % strain. This difference between collagen, Matrigel and related hydrogels becomes even more obvious when comparing the normalized differential module (Fig. 4-8D). Within the first cycle at the highest strain amplitude of 120 %, collagen networks get up to 170 times stiffer than in the linear regime. In comparison, the differential module of pure Matrigel only doubles.

4.7 Conclusion and Outlook

Recent studies highlighted the complex biochemical composition of Matrigel and compared it to the chemical highly uniform network of collagen gels[62]. In rheological studies their description is mostly limited on the linear mechanical properties of the hydrogels[72]. In this chapter, the nonlinear and plastic properties of collagen gels and Matrigel were characterized and contrasted in detail. In particular, the highly nonlinear and plastic behaviour of collagen was demonstrated. The major nonlinear characteristics of collagen networks are a strain-stiffening at large strains as well as marked strain-softening at small strains with increasing cycle number. As a consequence of the concomitant dissipated work, the network stores overall less elastic energy with each cycle. However, the development of the dissipative work

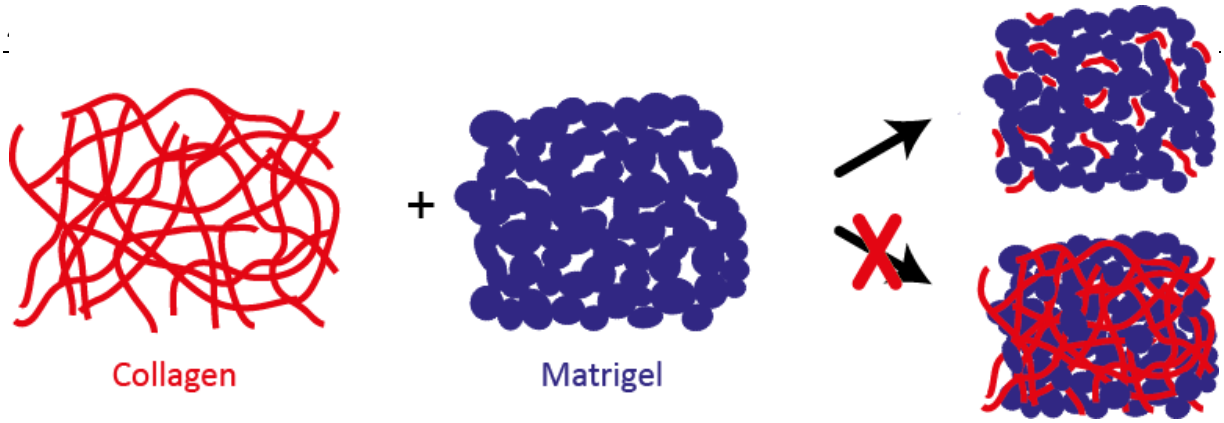

***Figure 4-9*:** The combination of the individual network structures of collagen and Matrigel does not describe the structure of the resulting hybrid gel. A simultaneous polymerization of both hydrogels leads to a separate network structure.

and maximal reached load after four cycles did not equilibrate and thus indicate that remodelling processes such as fiber alignment or the binding and unbinding of weak crosslinks did not saturate but led to steadily reduced changes in the mechanical properties[11,75]. The observed characteristic properties were fully conserved in additional crosslinked collagen networks but partly appeared to be differently pronounced. While crosslinked collagen networks are significantly stiffer and dissipated less work, their percental reduction of the peak stress exhibits the same decrease as in pure collagen networks. In contrast, Matrigel exhibits a predominantly linear stress response with only little plasticity and a diminished strain-stiffening and softening. Due to the long relaxation times within Matrigel, which are demonstrated by strain jump experiments, the plastic effects can mainly be attributed to a viscous loss in the network. This is further emphasized by the steady amount of dissipated work throughout all cycles.

Further, it was demonstrated in this chapter how the nonlinear and plastic mechanical properties of collagen and Matrigel can be tuned by the fabrication of hybrid gels of both components. In particular, the plasticity as well as the linear and nonlinear stiffness can be gradually adopted with variation of the mixing stoichiometry of collagen and Matrigel. At low Matrigel concentrations hybrid gels exhibit the diminished characteristic of collagen with the typical strain-stiffening and softening. By increasing the Matrigel concentrations the characteristics of collagen get markedly supressed and mainly a viscous-loss can be observed, which is typical for pure Matrigel. These different impacts of the materials can be linked to the underlying network structure of the collagen network as with increasing Matrigel concentration the collagen mesh size gradually decreases until no fibrillary matrix can be observed anymore. The different network structures can be explained by the earlier polymerization dynamics of Matrigel, which in turn suppresses collagen polymerization. As a result of the shorter fibers and the concomitant supressed crosslinking only a remarkable reduced amount of energy can be dissipated through the collagen network, which explains the reduced plasticity in hybrid gels with increasing Matrigel concentration.

In summary, the results emphasize the mechanical and structural specificity of each analysed hydrogel. So far, hybrid gels were mainly used without further analysing their individual structure and mechanical response and just mixed uncared. Yet, it has been demonstrated in this chapter that the mechanics and structure of a hybrid gel cannot be simply concluded from

the individual properties of the hydrogel components but need to be characterized separately (Fig. 4-9). In particular in chapter 4.2, it has been shown that the polymerization dynamics of the individual components highly differ in comparison to the polymerization dynamics of hybrid gels consisting of the same components. As a result, also the structure of the hybrid gels cannot be described solely as sum of the individual components but polymerizes into a hydrogel with differing network structure. In addition, the observed differences in the linear and nonlinear mechanical behaviour of the hydrogels can be transferred to the matrix-dependent cellular migration in 3D matrices. While cells embedded in pure Matrigel exhibit no protrusions and reduced cell-ECM invasion, an enrichment of Matrigel with collagen I leads to an increase of filopodia-like protrusions until cells in pure collagen networks show a marked ECM invasion[29]. In particular, it has been demonstrated that cell migration is enabled by hydrogels with a high plasticity and is nearly inhibited in hydrogels with low plasticity[33]. During organogenesis of mammary gland organoids the resulting morphology highly varies in-between Matrigel and collagen I matrices[53]. While organoids cultivated in Matrigel exhibit a smooth cell-ECM boundary and a humble cell-ECM interaction, organoids grown in collagen form filopodia-like protrusions at their invasion site. Hence, the presented results have a huge potential to explain 3D cell migration in dependency on the mechanical properties of the used hydrogel as well as ECM-specific organoid phenotypes in different ECMs.

5 Compatibility of 2D and 3D luminal cell culture assays

In vivo structure formations such as embryogenesis or tumorigenesis are the result of a complex interplay between biochemical, mechanical and environmental regulators and signaling pathways[36,37]. These structure formation are orchestrated by complex collective cellular interactions between various cell types[80–82]. In particular during organogenesis, branch elongation and structure remodeling are enabled by cellular rearrangements and an internal cellular migration[38,83]. To recapitulate the cellular migratory behavior *in vitro* the complexity of the environmental conditions are often reduced to two-dimensional model systems[12]. Hereby, cells are cultivated on top of extracellular matrix proteins such as collagen or fibronectin where they adhere and migrate, without invading into an ECM. By spatially confining cell migration to a restricted 2D area, the three-dimensional confinement by the ECM *in vivo* is mimicked[84,85]. Collective patterns are generated by these migrating cells depending on the geometry of the boundary conditions. While on 2D cyclic patterns cells show a collective rotational migration, on strip-like patterns cells exhibit a directed collective outgrowth[23,24]. In artificial 3D tubular confinements cellular migration displays a combination of both phenomena[26]. Cells collectively rotate perpendicular to the long axis of the tube while extending. In comparison, in 3D hydrogel assays such a tubular confinement is naturally given by the ECM which in turn hampers the cellular migration and complicates ECM invasion. Cell migration and ECM invasion are specifically steered by the mechanical and structural properties of the ECM[27]. This environmental difference of 2D and 3D assays induced by the ECM raises the question to which degree cellular phenomena in 2D can be transferred to the cellular behavior in 3D.

In this chapter, primary luminal mammary gland cells were cultivated in 2D and 3D cell culture assays. In particular, their behavior in both dimensionalities was compared depending on the activation of Rho-associated protein kinase (ROCK) and its related signaling pathways. First, the properties of luminal cells were characterized on a collagen-functionalized 2D surface in dependency on the cultivation with and without the ROCK-inhibitor Y-27632. Their migratory and proliferative behavior was examined *via* live-cell imaging during spatial unrestricted and restricted expansion. Second, cell proliferation and invasion were monitored in 3D collagen matrices. It was demonstrated that branched organoid formation is restricted to cell culture media enriched with Y-27632. On the base of live-cell imaging and biochemical treatment affecting matrix degradation and cell-cell adhesion, the observed branch elongation is linked to the internal directed and collective cell migration. In particular, branch outgrowth is guided by specified leader cells, while stalk cells in the back get dragged outwards. Ultimately, 2D and 3D observations are compared.

5.1 Cell dynamics on functionalized 2D surfaces

To study cellular phenomena, 2D cell assays have the advantage of an easy accessibility and preparation. The experimental setup enables a straightforward observation and simple

manipulation of the culture conditions. Here, luminal progenitor cells were seeded on a collagen functionalized surface and analyzed in dependency on different concentrations of the ROCK-inhibitor Y-27632. Their proliferation and migration were monitored using live-cell phase contrast microscopy over a time course of up to 24 hrs. In addition, fluorescence imaging of the underlying actin network for both conditions were conducted.

Luminal progenitor cells were seeded without any spatial restriction on a collagen functionalized surface using different media compositions. While one medium was enriched with 5 µM Y-27632, the other contained no ROCK-inhibitor. To guarantee a reliable comparability, both media conditions were measured at the same time with the equal initial cell density. As a result, the proliferation rates of the cells cultivated in each media

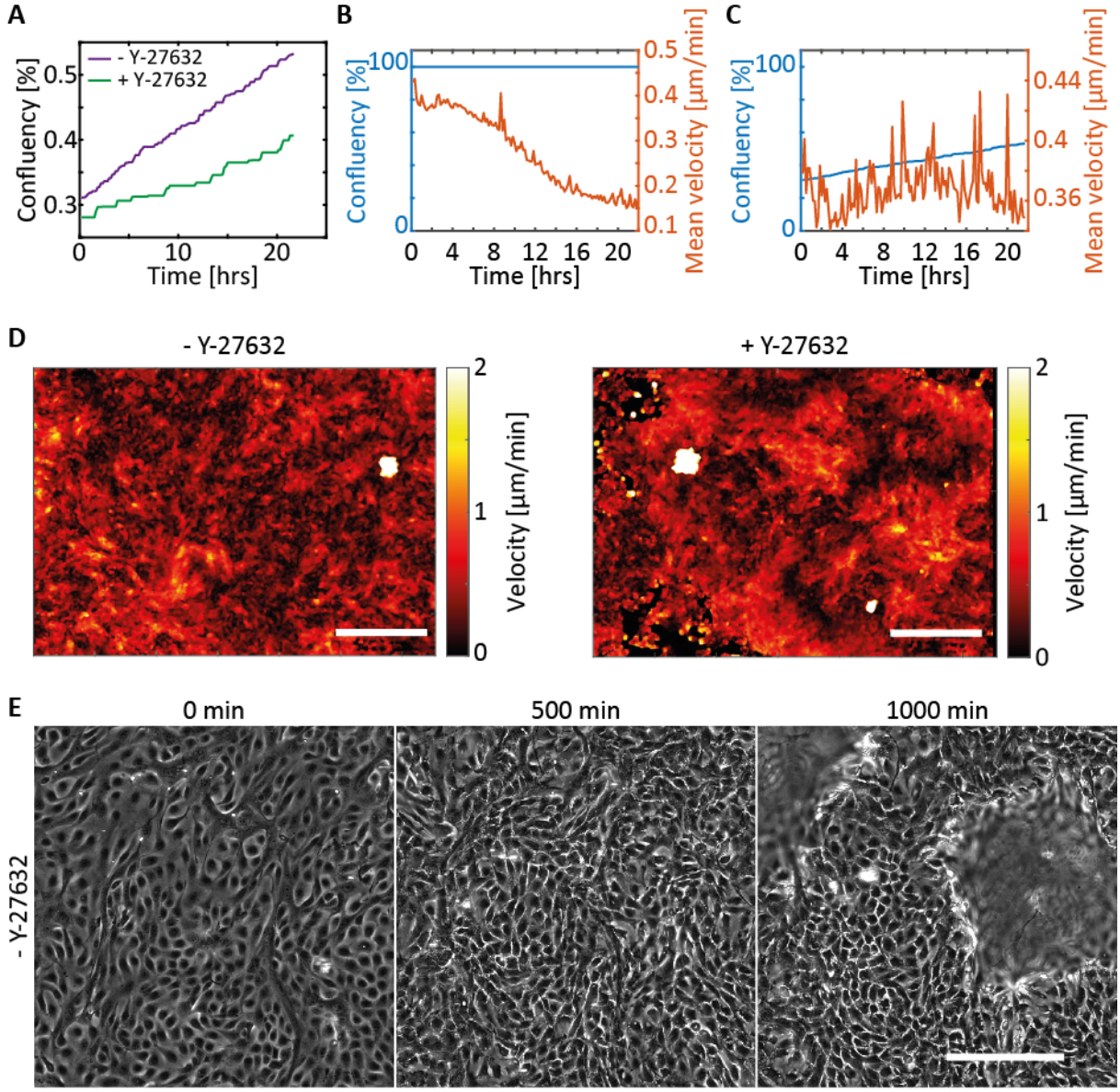

Figure 5-1: 2D cell proliferation and migration of primary luminal cells. A *Cells cultivated with 5 µM Y-27632 exhibit a slower proliferation than cells cultured without Y-27632.* ***B, C*** *Representative development of the cell velocity (**B**) within a confluent layer and (**C**) an expanding cell layer.* ***D*** *Macroscopic overview of the cell migration field in dependency on ROCK-inhibitor concentration at the same cell density.* ***E*** *Representative dome formation. Scale bars, 1 mm (**D**), 200 µm (**E**).*

composition was derived by calculating the confluency over time. Hereby, cells cultivated with ROCK-inhibitor proliferate significantly slower than cells cultured without (Fig. 5-1A). While the doubling time for cells with ROCK-inhibitor calculates to around 50 (± 9) hrs, the doubling time for cells without ROCK-inhibitor is around 30 (± 3) hrs. In addition to the proliferation rate, the migratory behavior of the cells was analyzed in detail as ROCK upregulates myosin light chain which in turn affects cellular contractility. At low cell density luminal progenitor cells either migrate individually or in small clusters of adherent cells with a constant velocity (Fig. 5-1C). Thereby, cells show random migration patterns in their two-dimensional environment. In the long-term of several hours, single cells either collide into an existing cluster and adhere to it or establish their own cluster as a consequence of individual cell division. In time, these clusters merge and ultimately expand into an epithelial sheet covering the whole surface. The underlying migration and expansion patterns appear similar in both media conditions with and without the ROCK-inhibitor Y-27632 (Fig. 5-1D). In both conditions, cells exhibit similar mean migration speeds between 0.3 and 0.6 µm/min. In particular, individual cells and cell clusters exhibit similar speeds. Once 100 % confluency is reached the migration speed first stays constant. Within the developed epithelial sheet, cells exhibit noticeably collective cell migration patterns, characterized by neighboring cells exhibiting similar cell velocities and migration directions. However, due to the ongoing proliferation

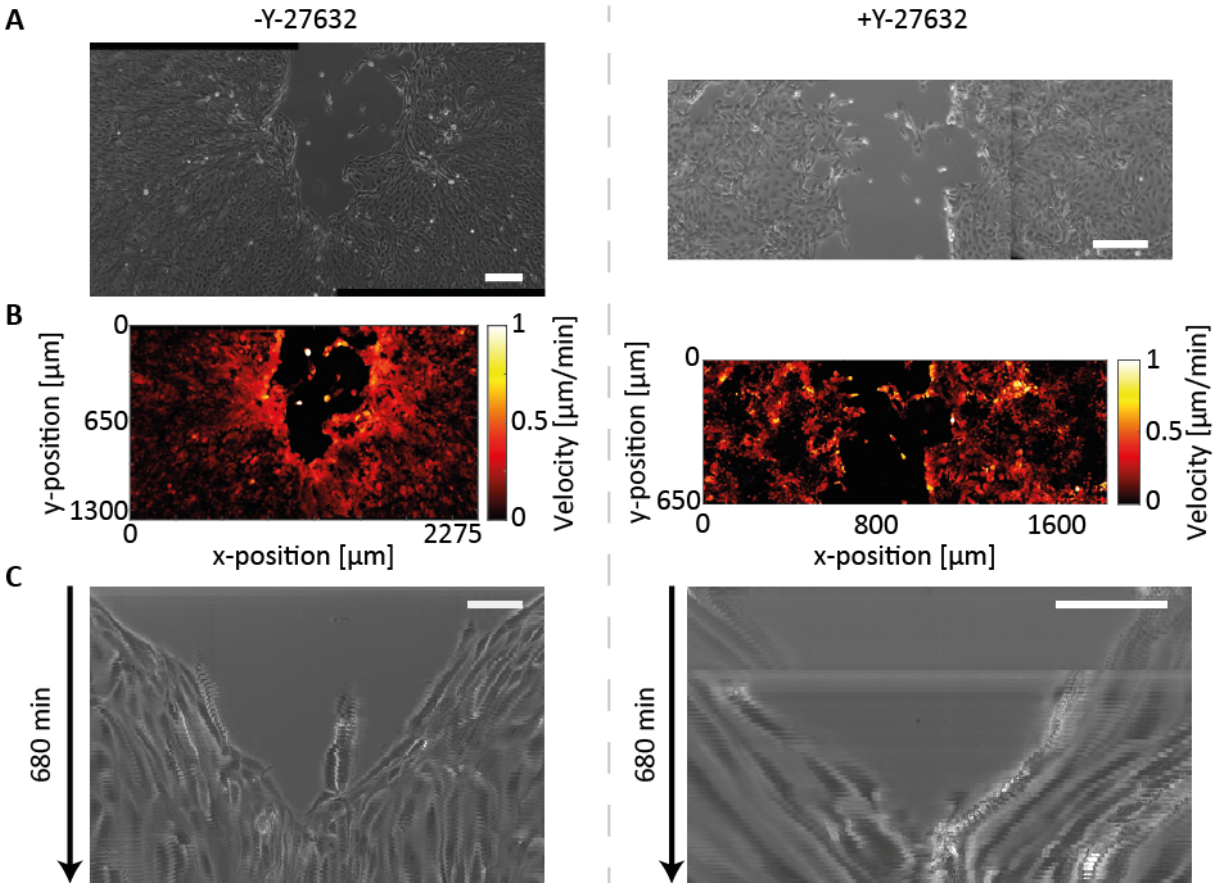

Figure 5-2: Wound healing assays. A *Representative wound at different time points and for different culture conditions. Left: Wound after 5 hrs. Right: Wound after 1 hr.* ***B*** *Velocity patterns for the different culture conditions. Highest velocities are detected at the leading edge.* ***C*** *Kymographs showing the closure of the gap in the time course of 680 min. Scale bars, 200 µm (**A**), 25 µm (**C**).*

within the cell layer and the resulting increase in cell density the migration speed of the cells slowly reduces (Fig. 5-1B). With increasing cell density, parts of the epithelial sheet buckle upward into the third dimension without loosening the cell-cell adhesion. The arising structures are reminiscent to the epithelial domes, which were observed also for epithelial sheets of MDCK cells[21].

In order to enable a directed cell migration and enhance the comparability between different culture conditions a reproducible experimental setup with a defined migration geometry is necessary. Therefore, wound healing assays are a suitable tool, in which the closure of a gap with defined size can be monitored (Fig. 5-2A)[86]. Experimentally a defined cell density and reproducible spatial confinement is realized. The closure of the gap and the cell velocities highly depend on the number of cells and the internal cellular pressure and thus can vary in-between the measurements. In particular, a higher cell density leads to a faster closure of the gap. During wound healing assays of the luminal cells no significant differences in dependency on the culture conditions were detectable. With and without ROCK-inhibition cells exhibited similar velocities of up to more than 1 µm/min (Fig. 5-2B). In both conditions the highest velocities were detected at the leading edge of the wound, while the cells in the back just

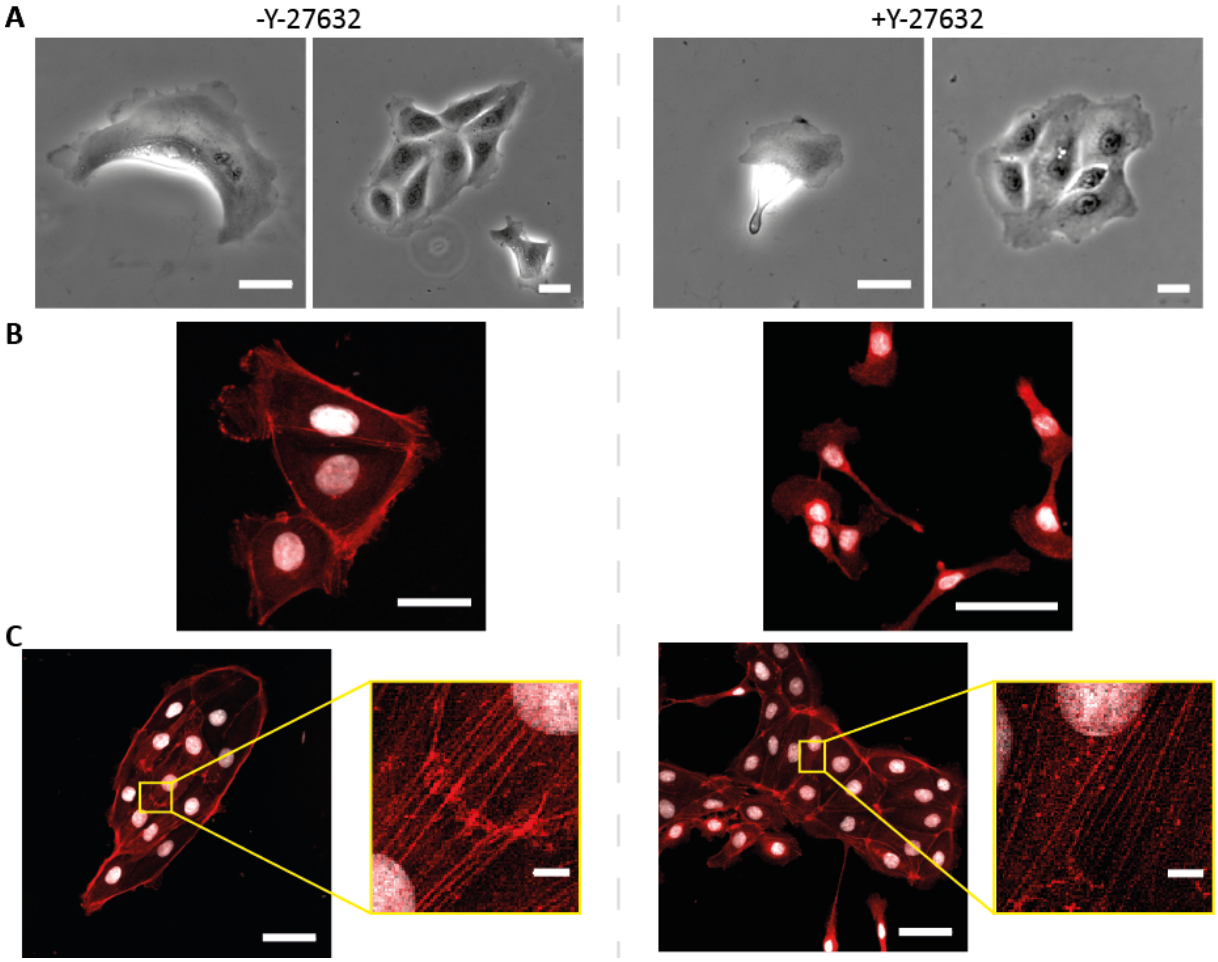

Figure 5-3: Cell morphology and actin cytoskeleton in dependency on the culture conditions. A *Cell morphology of single cells and cell clusters imaged by phase contrast microscopy.* ***B*** *Actin network in individually migrating cells.* ***C*** *Actin network and stress fibres in cell clusters. Scale bars, 25 µm (**A, B**), 50 µm (**C**), 5 µm (inset **C**)*

slowly migrated outward. Leader cells exhibited velocities between 0.6 µm/min and 1.2 µm/min. Consequently, the closure of the 500 µm sized gap took in both conditions between 7 and 14 hrs (Fig. 5-2C).

In addition to affecting contractility and migration, an upregulation of ROCK is also activating LIM kinases which leads to a phosphorylation of cofilin. As a consequence, actin depolymerization gets inactivated which results in filament stabilization. In single cell morphology, within the phase contrast images of treated and untreated cells only marginal differences during migration can be observed (Fig. 5-3A). In both culture conditions cells form a distinct lamellipodia. While cells cultivated without Y-27632 exhibit a broader lamellipodia, ROCK-inhibited cells display a slightly smaller lamellipodia. In comparison, the general morphology of cell clusters and confluent cell layers looks similar in the phase contrast images. To specifically investigate the underlying actin structure, phalloidin staining against actin was conducted. The actin network of single cells as well as of cluster of cells was monitored. In single untreated cells the lamellipodia exhibits a marked actin accumulation and the formation of single stress fibers (Fig. 5-3B left). In contrast, the actin network of ROCK-inhibited cells looks diffused with an increased actin accumulation around the nucleus (Fig. 5-3B right). Within arising cell cluster this difference is conserved. While at the boundary of untreated cells a distinct actin expression is observable, ROCK-inhibited cells again display a diffuse actin network (Fig. 5-3C). However, in both conditions cells display stress fibres spanning over neighboring cells (Fig. 5-3C yellow inset). Yet, in particular ROCK-inhibition leads to slightly less marked fibres.

5.2 Organogenesis of luminal cells in 3D matrices

When progressing from 2D to 3D cell culture conditions, primary human luminal cells grow in the time course of two weeks into multicellular complex branched structures, mimicking the morphology of the mammary gland *in vivo*. This capability of the cells cannot be extracted from the 2D assays and is first revealed by embedding the cells in a 3D environment. In comparison to 2D assays, cells start to proliferate as singularized cells and thus do not adhere to other cells but mainly to the collagenous matrix surrounding them. As a consequence, cell-matrix adhesion as well as mechanosensing become major key parameters driving cell proliferation and migration[87,88]. These changed culture conditions not only differ regarding different adhesion sites and concomitant signaling pathways, but also induces a physical confinement in which the cells migrate and expand[27,89].

In the following chapter section, the growth behavior of the luminal organoids will be characterized with the focus on the growth dynamics, the internal cellular migration and the interplay of the cells with their surrounding matrix. In order to reveal the underlying mechanism driving branch elongation and matrix invasion the organoids will be manipulated using inhibitors which affect cell contractility, cell-cell adhesion as well as matrix degradation. Simultaneously, the organoids are monitored *via* live-cell imaging to specifically reveal the

underlying processes driving branching morphogenesis. In total more than 100 organoids of five different donors were examined.

5.2.1 Growth behavior

The growth behavior of luminal organoids can be divided in three different developmental phases: an establishment phase, a branch elongation phase and a finalizing growth phase. Within the establishment phase from day 0 to day 5, cells adhere to the matrix and adapt to the culture conditions. Within this phase, cells do not divide and thus stay as singularized cells. From day 5 to day 11 cells start to proliferate, form cell-cell aggregates and invade into matrix. As a result, different multicellular structures evolve: spheres, sticks but mostly important highly branched organoids, which mimic the mammary gland *in vivo*. More specifically, between 43 % and 73 % of the structures are branched organoids. During this phase, organoids develop primary, secondary and up to tertiary side branches. Within the final growth phase from day 11 on, organoid branches stop invading into the matrix while their branch tips simultaneously round up. Finally, organoids reach a diameter of more than 1 mm. Particularly, organoids are monoclonal and thus derive from a single cell only and not from initially formed cell aggregates. Specifically, between 1 out of 9.52 and 1 out of 20.7 freshly sorted luminal progenitor cells successfully survive the first phase and are partial capable to form organoids. However, once luminal cells were cultivated in 2D the potential to form an organoid increases as just cells which already adapted to the culture conditions survived the first cultivation. In the following, organoid formation specifically during the branch elongation phase will be the focus.

Elongation and side branching

In order to analyze the branching behavior of the luminal organoids in time, live cell confocal imaging of organoids between day 7 and day 9 was conducted over a time course of around 24 hrs (Fig. 5-4A). In addition, fluorescent tracer particles were embedded within the matrix to investigate deformations and remodeling processes within the ECM. During branch elongation phase, the majority of branches continuously elongated and invaded into the ECM. Only short interruptions during the invasion were observable, independent on the branch length (Fig. 5-4B). Simultaneously, branches either grew bigger or kept their initial branch width, but never shrank in size (Fig. 5-4C). During the elongation process only minor deformations in the ECM were observable. These deformations were restricted to the near field of invading branches and were neither detected at the sides of an elongating branch nor in the far field. Throughout the whole elongation and branching process, the individual cells within the branches appear to be highly motile which is marked in distinct fluctuations of the organoid boundary. During this developmental phase, bright field imaging revealed in total 26 side branching events during which new branches arose (Fig. 5-4D). In general, mainly two mechanisms describing side branching are described. Either branches split *via* bifurcation, where the tip of the initial branch divides into two new individual branches or a new branch arises from the side of an already existing branch as a result of individual cell invasion[90,91]. In

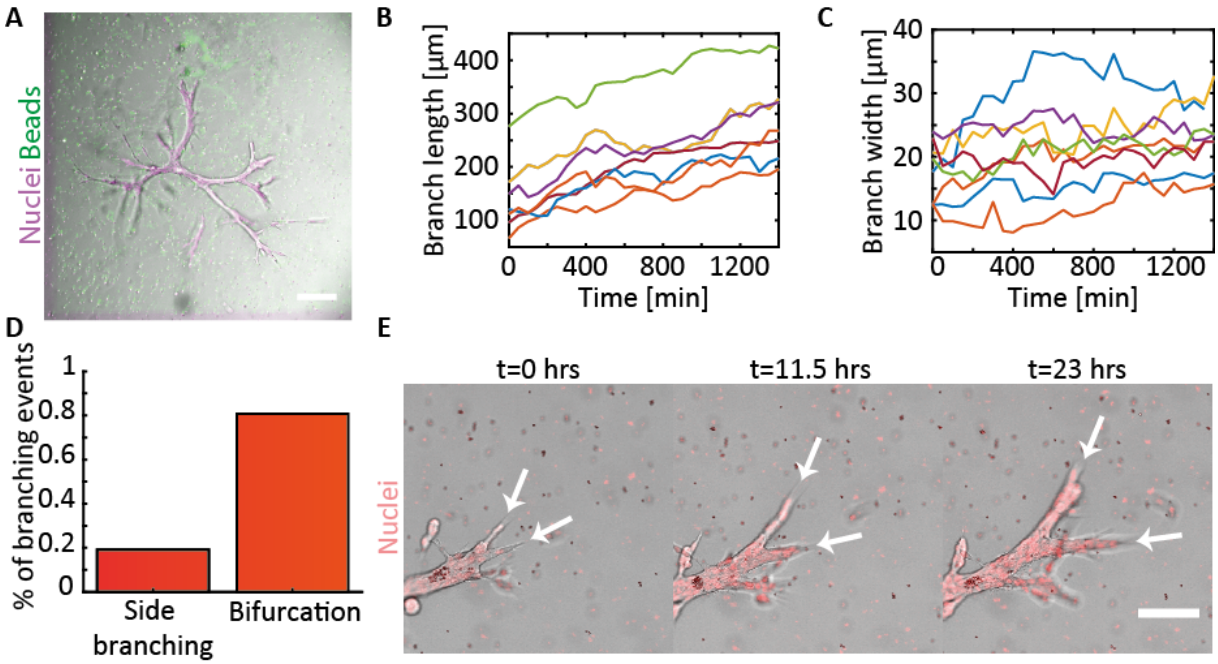

Figure 5-4: Luminal organoid growth and side branching. A B, C *Temporal development of (**B**) branch length and (**C**) branch width for different organoids.* ***D*** *Spatial distribution of branching events.* ***E*** *Representative branching event. Scale bars, 200 µm (A), 100 µm (E).*

particular, during the branch elongation phase of luminal organoids, 80 % of the branching events happen *via* bifurcation while only in 20 % of the cases branching results from side branching of individual cells. In order to unravel the temporal development of the dominant branching *via* bifurcation, brightfield imaging of specifically the branch tips were conducted (Fig. 5-4E). In general, it can be observed that branches can be led by only one cell or by a collective of cells, which sense their environment and invade into the ECM by the formation of filopodia-like protrusions. However, prior to branching *via* bifurcation, the tip is always led by at least two cells which are responsible for establishing new branches. These cells adhere to opposing invasion sites and thus invade the ECM in different directions. As a consequence, the tip cells migrate independently from each other and diverge further apart. After the establishment of two new branch tips, the stalk cells follow the tip cell dependent on their position within the branch and further facilitate the elongation processes of the newly formed branches. Finally, in the time course of around 24 hrs two new independent branches establish. Branches at the side did not emerge at a specialized position but were the result of an ECM invasion by a single cell.

A reduced contractility is key factor for luminal branching morphogenesis

As described above, during 3D cell migration cell contractility has become an important factor driving the invasion process into the ECM. Especially in tissue morphogenesis, it is the collective interplay of contractile cells leading to pronounced ECM deformations and concomitant fiber alignment[92]. Consequently, the impact of contractility on luminal organoid growth was analyzed. Here, a main key regulator is ROCK, which predominantly regulates actin

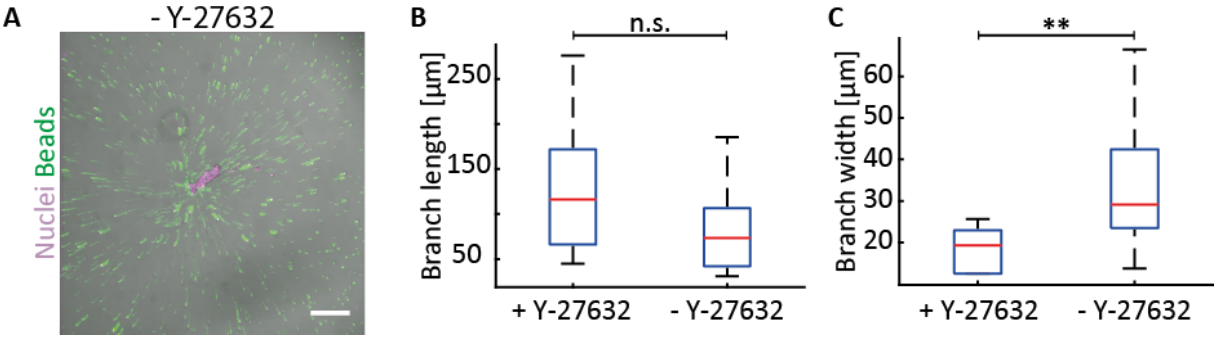

Figure 5-5: ECM deformation field and organoid morphology in dependency on the ROCK-inhibitor. ***A*** *Deformation field of a growing organoid cultivated without ROCK-inhibitor.* ***B, C*** *Organoids cultivated with and without Y-27632 did exhibit (B) no significant difference in their branch length but* ***(C)*** *a significant difference in their branch width. Scale bar, 200 µm* ***(A)****.*

organization within a cell and thus cell migration and cell contractility[93]. ROCK inhibits depolymerization of actin filaments *via* activation of LIM kinase and promotes cellular contractility by activation of myosin II. In the standard culture conditions ROCK-activation and thus the contractility is reduced by the addition of 5 µM Y-27632, a prominent ROCK-inhibitor. Consequently, in order to induce a higher contractility, Y-27632 was removed from the media used from day 5 until day 14. As a result, cells mainly grow into spherical or elliptical cluster and thus lose their capability to form branched organoids (Fig. 5-5A). Only in rare cases, branched organoids occur. These structures do not resemble the highly branched architecture of the mammary gland *in vivo* but only exhibit primary branches. Overall, the developing branches grow as long as control branches but grow significantly thicker (Fig. 5-5B, 5-5C). To reveal differences in the differing growth behavior, live-cell imaging between day 9 and 10 was conducted. Tracking of fluorescent beads within the ECM was used to display the deformation fields during the growth. Cells grown in media without Y-27632 exhibit a distinct omnidirectional deformation field. Each cell, which is in contact with the ECM, exhibits contractions and thus, no tip cell establishment guiding a branch outgrowth can occur. Overall, the deformations are in the order of 9 (±2) µm/hrs. In contrast, organoids treated with Y-27632 only exhibit deformations restricted to the tip of the branch, which are in the order of 5 (±1) µm/hrs.

5.2.2 Cellular dynamics

As the brightfield measurements already indicate cellular rearrangements and interactions within the organoid, nuclei were supplementary labelled using a fluorescent dye targeting the histones. Consequently, the internal dynamics of cells can be monitored. Two major observations become obvious. First, nuclei proliferate independent on their position within

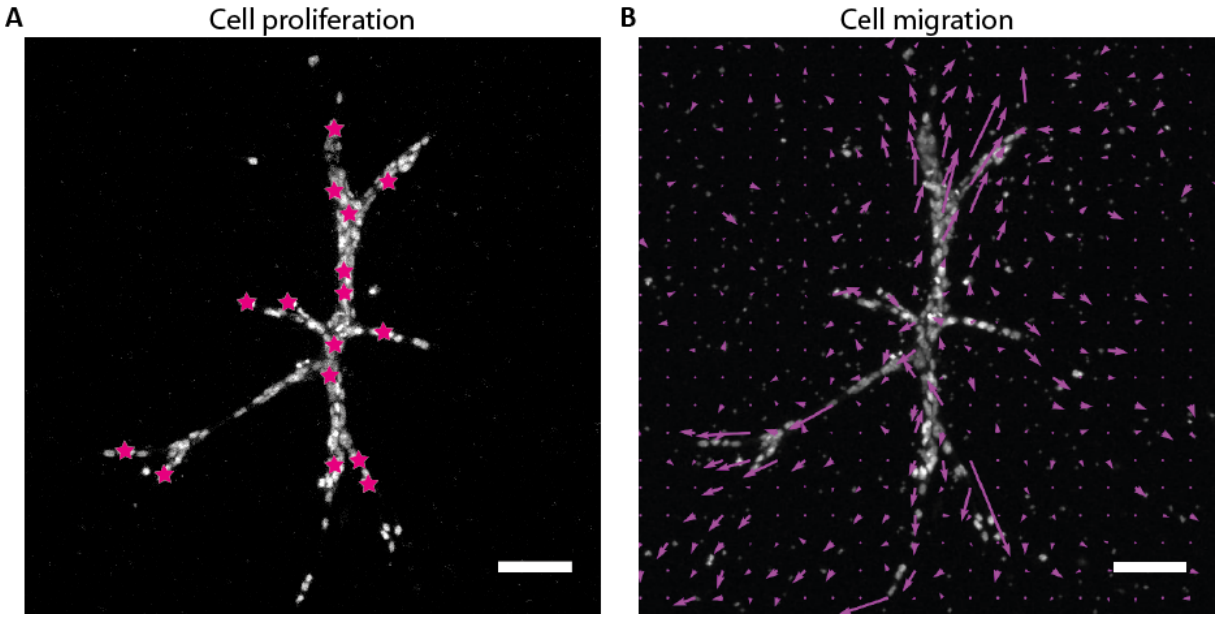

Figure 5-6: Luminal organoid growth. ***A*** *Proliferation can be seen everywhere within the organoid. Every star refers to a cell division within a time course of 6 hrs.* ***B*** *Velocity field of the internal cell migration and deformation field of the ECM. Scale bars, 100 µm (**A**, **B**)*

the organoid and second, cells are motile showing a collective and mainly outward directed migration (Fig. 5-6A, 5-6B).

Cell proliferation is driving branch growth

Prerequisite for the continuous organoid growth and concomitant branch expansion is an increasing cell number. Within the luminal organoids live cell imaging reveals no specific area where an increased cell division rate is observable. In contrast, cells within an organoid proliferate equally within the organoid body as well as in primary, secondary and tertiary branches. Further, the number of cell divisions is highly heterogeneous in-between organoids and donors and seems to be stochastic. With increasing cell number an increase in cell divisions is observable. In order to examine a possible link between branch elongation and cell division, both properties were extracted from the live cell imaging data and correlated (Fig. 5-7A). During the time course of 25 hrs persistent cell divisions can be observed within all analyzed branches, while the length change highly varies in-between the branches. Some branches continuously elongate, some oscillate around their initial branch length and others

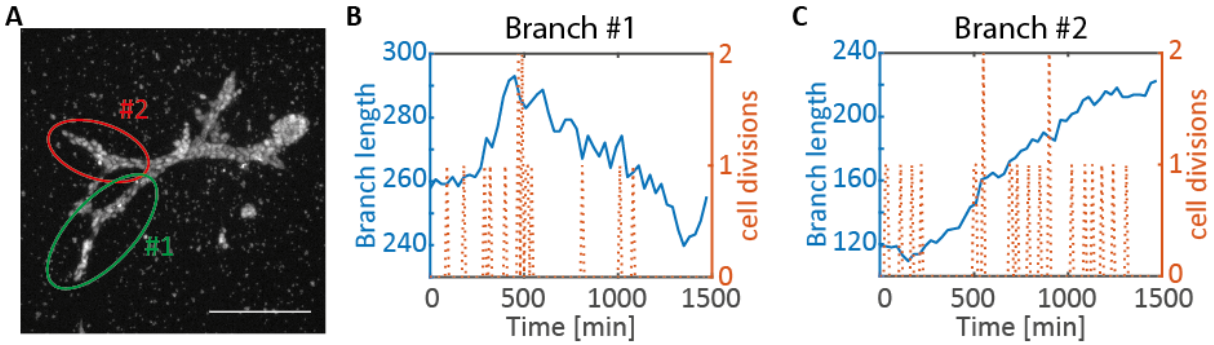

Figure 5-7: Branch extension and cell divisions. ***A*** *Representative organoid for the analysis.* ***B***, ***C*** *Branch extension and time points of cell divisions for different branches. While branch #1 shrinks after several cell divisions, branch #2 extends. Scale bar, 200 µm (**A**).*

shorten (Fig. 5-7B, 5-7C). Throughout the measurements, no correlation between individual branch elongation and related cell divisions can be found. This observation hints towards a global connection of the individual branches within the organoid or further parameters such as biochemical signaling which additionally regulate branch elongation.

Luminal cells are highly motile within the organoids

In addition to the pronounced proliferation, cells reveal to be highly motile within the organoid. During their migration, cells migrate with a mean velocity of 0.1 µm/min. However, the actual velocity of cells within a branch differs between branches, organoids and donors. Predominantly, cells within the branches migrate collectively and parallel to the branch axis with only small movements along the orthogonal branch axis (Fig. 5-8A, 5-8B). As a consequence, their overall velocity is dominated by the parallel velocity component, while the associated orthogonal velocity is negligible. Due to cell-cell adhesion, neighboring cells exhibit similar velocities, leading to spatial clusters of cells migrating with a comparable velocity. Only in rare occasions individual cell rearrangements in opposite direction can be observed. The developing spatial patterns which exhibit similar velocity can span up to several 100 microns. In time, these patterns merge and newly evolve at various positions within the branch, leading to highly dynamic velocity patterns. Consequently, cells do not persistently migrate in time but show an irregular stop-and-go pattern. In particular, branches exhibit long time periods in which the cells migrate towards the branch tip, while during short interruptions cells exhibit a stop in their motion or even a brief migration towards the organoid body (Fig. 5-8C). Summarizing, cells spatially and temporally predominantly migrate collectively towards the branch tip and thereby facilitate branch elongation.

Tip-cells guide branch elongation

As described briefly in chapter 5.2.1, the tip of a branch is guided by one or even more tip cells, which are followed by the so-called stalk cells. The tip cells are highly responsible for the invasion into the ECM. During branch elongation, tip cells exhibit a distinct stop-and-go motion

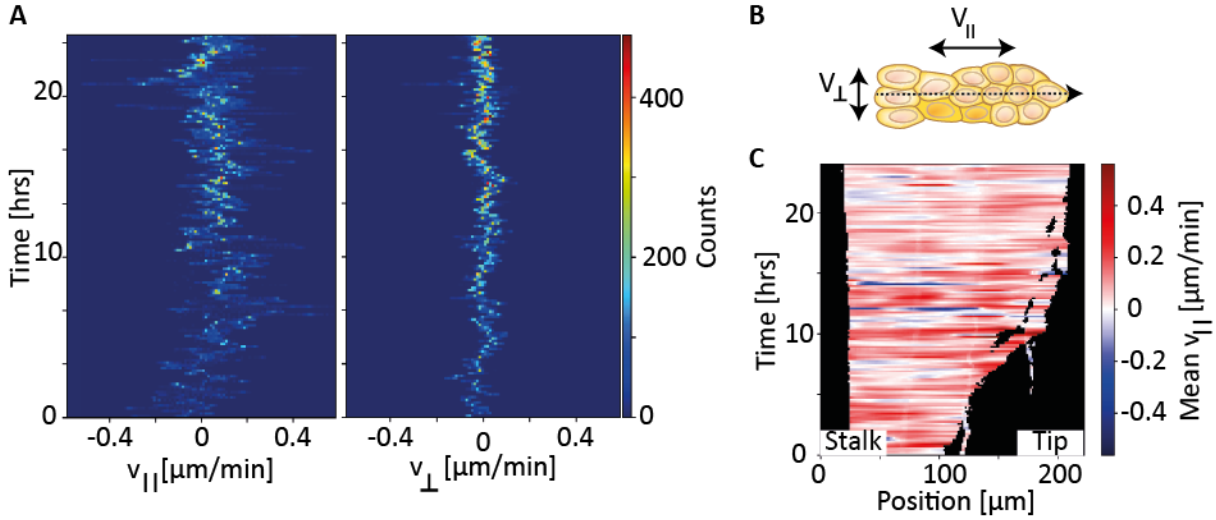

Figure 5-8: Velocity distribution in luminal organoid branches. ***A*** *Representative temporal development of the parallel and orthogonal velocity.* ***B*** *Schematic definition of the velocity separation.* ***C*** *Representative spatiotemporal development of the cell velocities within an extending branch.*

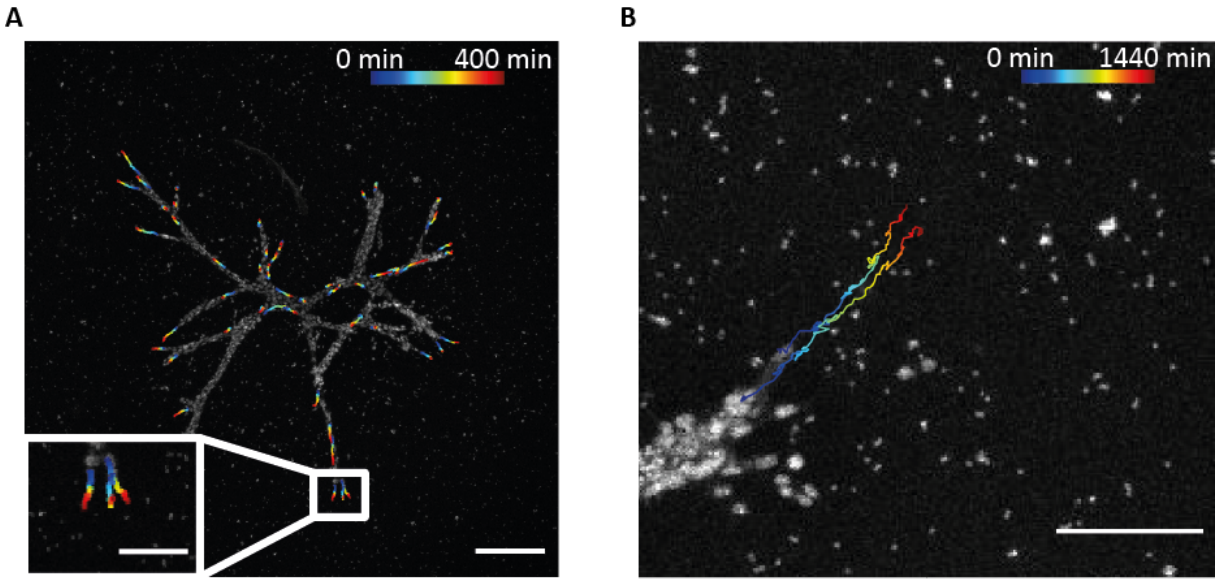

Figure 5-9: Tip-cell dynamics. A *Internal migration of individual cells. Tip and stalk cells predominantly migrate outwards.* ***B*** *In time, tip cells are overtaken by stalk cells in their back. Scale bars, 100 µm (**A**, **B**).*

but exhibit with up to 0.05 µm/min a slower migration speed as the stalk cells. Consequently, the stop-and-go pattern of the stalk cells results from fast outward migrating cells bumping into the slower migrating tip cells causing a jamming within the branch. Similar to the stalk cells the tip cells predominantly migrate away from the organoid body and only in rare cases migrate inward (Fig- 5-9A). Individual tip cells are not permanently designated but can be replaced by following stalk cells. Either tip cells are overtaken by faster stalk cells while they keep migrating or they even stop their invasion while neighboring stalk cells keep migrating and thus get replaced. Judging from the live-cell imaging data, this replacement process seems to be purely stochastic. In addition, live-cell imaging of the nuclei further proofs the in chapter 5.2.1 described mechanism driving side branching *via* bifurcation. During invasion, tip cells adhere and sense various adhesion sites of the ECM in front of them. Thereby, neighboring tip cells occasionally decide to migrate in opposing directions. Consequently, the branch splits at the tip into to new branches with the stalk cells following partwise into both new branches (Fig. 5-9B).

Cell-cell adhesion is prerequisite for collective cell migration and organoid formation

A distinct cell-cell adhesion seems to be prerequisite for the developing collective cell migration patterns during collective cell migration. This requirement of cell-cell adhesion is in accordance with recent publications focusing on the cell-cell adhesion in the mouse mammary gland. Here, the formation of cell-cell adhesion *via* E-cadherin is found to be required in order to develop a healthy mammary gland *in vivo*[94]. In contrast, a reduction of E-cadherin expression is associated with an increased invasiveness of the tissue as observed during breast cancer[95]. In order to further scrutinize the cell-cell adhesion and the concomitant collective behavior of the luminal cells, organoids were treated with HECD1, a function-blocking E-cadherin antibody specifically reducing cell-cell contacts. Therefore, HECD1 was added at day 5 with beginning of the branch elongation phase after cells could successfully adapt to the

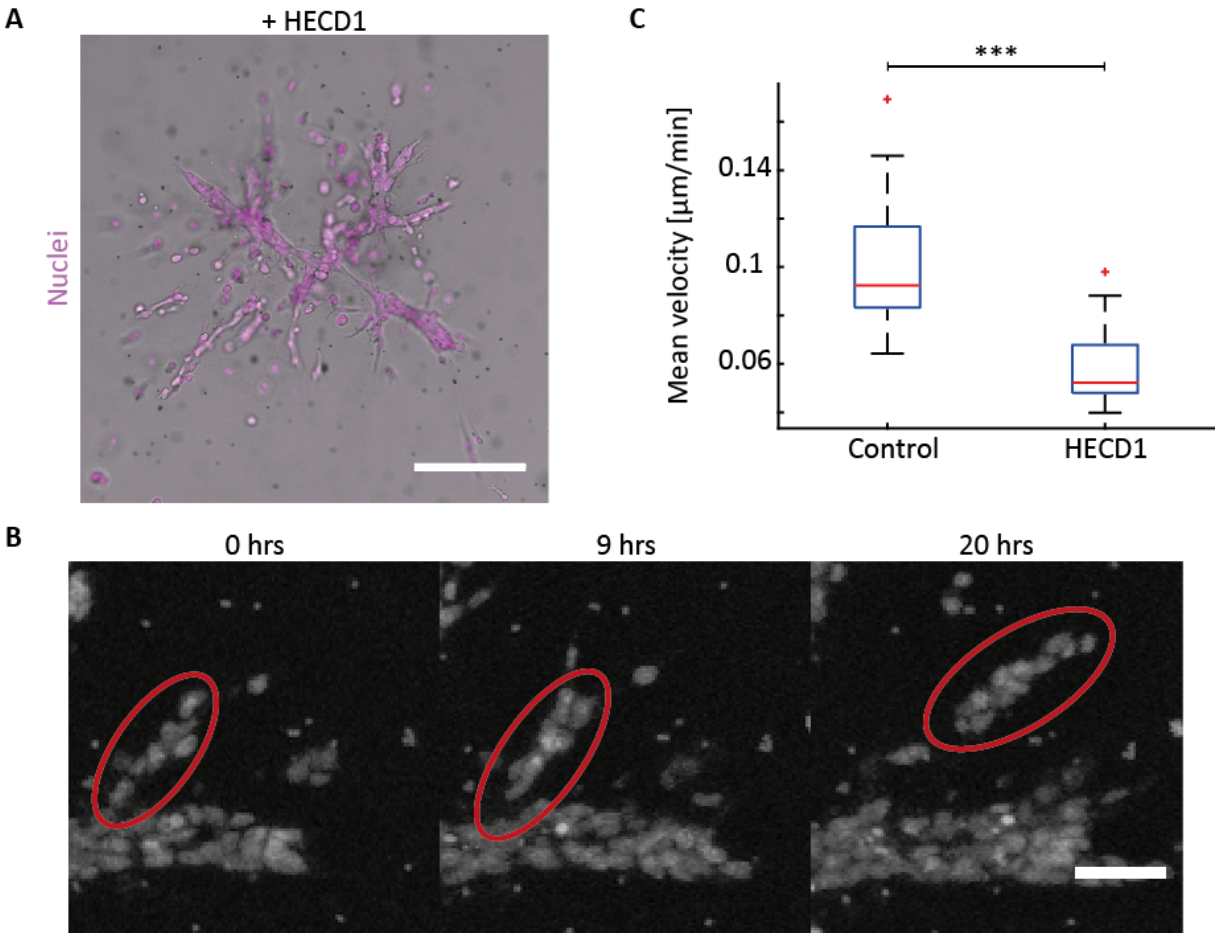

Figure 5-10: Inhibition of cell-cell adhesion leads to scattered organoids and prevents collective cell migration. ***A*** *Representative organoid grown with the HECD1.* ***B*** *Cell cluster raptures from the initial branch.* ***C*** *Inhibition of cell-cell adhesion leads to a significant decrease in the mean cell velocity. Scale bars, 200 µm (A), 50 µm (**B**).*

culture conditions. During the following cultivation, cells keep proliferating and also keep their capability to develop into branched structures. However, the developing branches become thinner, and the organoids appear torn (Fig. 5-10A). In particular, HECD1 treatment leads to an increase of singularized cells around the organoids. During live-cell imaging, it can be observed that individual branches partially thin out until they are just one single cell wide. Such branches even rapture into two parts, resulting into two unconnected branches (Fig. 5-10B). In addition, an increasing proportion of tip cells releases from the branch tip and invade individually into the ECM. Once the cells are unconnected from the organoid, they stop their invasion and remain at their current position, which explains the huge number of single cells around the developing organoids. Overall, the reduction of cell-cell contacts significantly decreases the mean migration velocity from 0.1 µm/min to 0.05 µm/min and leads to an enhancement of individual cell migration (Fig. 5-10C). In summary, these observations highlight the importance of cell-cell adhesion to establish a collective cell migration and to prevent individual cell migration, which in turn leads to the formation of a globally connected tissue. Further, the results highlight the necessity of E-cadherin in the human mammary gland, as it was proposed from observations found in mice[94,95].

Reduced cell contractility enables directed cell migration

As described in chapter 5.2.1, the modulation of the endogenous contractility of the cells by the treatment with the ROCK-inhibitor Y-27632 induces distinct changes of the resulting organoid morphology. The impact of the treatment on the underlying cellular migration was analyzed. Regarding the mean velocity of the cells no significant change between the two conditions can be observed. In both cases cells exhibit a mean velocity of around 0.1 µm/min with a comparable variance, indicating an intrinsic cell velocity independent on the contractile behavior (Fig. 5-11A). The underlying migration patterns differ drastically. Cells were cultivated in medium enriched with Y-27632 and thus the reduced contractility leads to the already described collective and directional migration and a concomitant local anisotropic deformation. In contrast, cells cultured in medium without Y-27632 are highly contractile and reveal a pronounced long-ranged isotropic deformation field. Further, these cells within the aggregates exhibit an individual migration. Cells mainly commute in circles around their central position as seen by calculating the directionality v_P/v_O, which is significantly reduced compare to the high directionality of cells inhibited with Y-27632 (Fig. 5-11B). The individual cell migration within the cell aggregates prevents a collective outgrowth of the tissue and leads to the formation of spherical or elliptical aggregates, without the identification of a designated tip cell. In summary, the pronounced isotropic deformation field in combination with the diminished collective cell migration leads to a loss of the capability to form highly branched structures. In contrast, the collective and directional cell migration and the establishment of designated tip cells enables organoid formation on the base of only small and anisotropic ECM deformations.

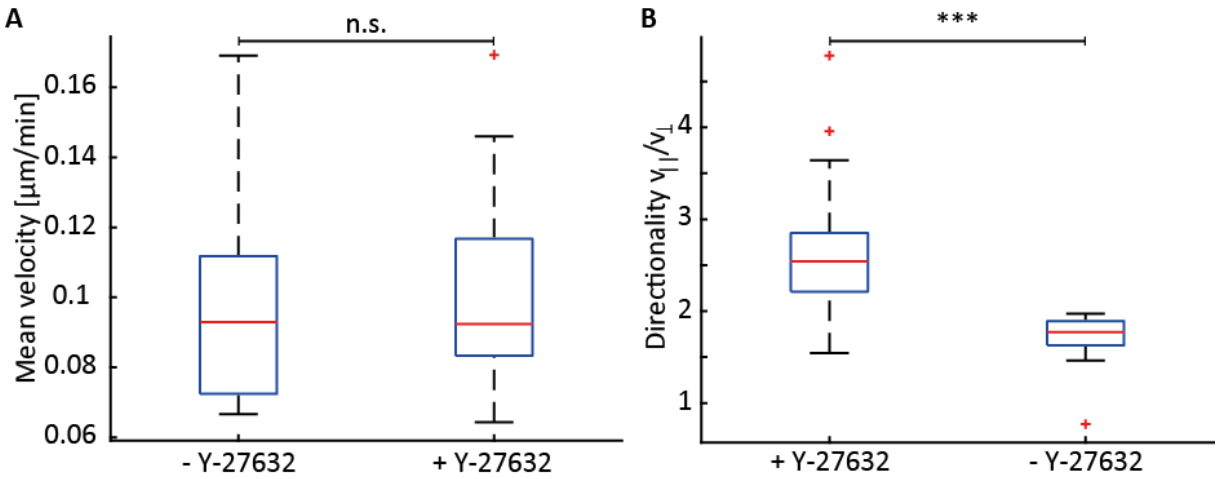

Figure 5-11: Cell migration velocity in dependency of the contractility. A *Cells exhibit no significant difference in their mean velocity if cultivated with and without ROCK-inhibitor.* ***B*** *Cells treated with Y-27632 exhibit a directed migration, while untreated cells exhibit similar velocities in parallel and orthogonal direction.*

5.2.3 Cell-matrix degradation and remodeling

Matrix degradation

In addition to the proliferation driven expansion and internal cellular interaction, the organoids invade into the ECM by interacting and remodeling the collagenous environment. In particular, recent studies highlighted the importance of matrix degradation *via* MMPs during the development of the mammary gland in mice[96]. In order to reveal the importance of MMPs during the branch elongation phase of luminal organoids, the cell culture medium of already branched organoids was enriched with 10 µM Marimastat, a broadband MMP-inhibitor (Fig. 5-12A). Within the first 10 hrs after addition, tip cells behave as in control organoids by forming filopodia and interacting with their collagenous environment. However, cells do not actively invade into the ECM anymore. Branches only slightly elongate as cells within the branches still proliferate (Fig. 5-12B). The cell mass is continuously increasing and pushing the branch further outward. At later time points tip cells round up and loosen their adhesion to the ECM. Consequently, branches get pulled towards the organoid center. After 20 hrs of MMP inhibition the overall elongation of the branches is significantly diminished, and branches end up around their initial branch length. In comparison to control organoids there is no significant difference in the development of the branch width. In both conditions, branches thicken around 30 % of their initial width during the same time period. The combination of the diminished branch elongation and the resulting concomitant steady branch volume with the ongoing cell proliferation leads to an increase in cell density. To reveal the internal cellular dynamics within the organoids, the nuclei were tracked during live-cell imaging. In the time course of 20 hrs the internal cell migration speed reduces significantly from about 0.1 µm/min to 0.07 µm/min (Fig. 5-12C). The initial predominantly outward pointing migration is stopped as ECM invasion is inhibited. As a result, cells mainly oscillate around their individual position and no collective cell migration or cellular rearrangements are observable anymore.

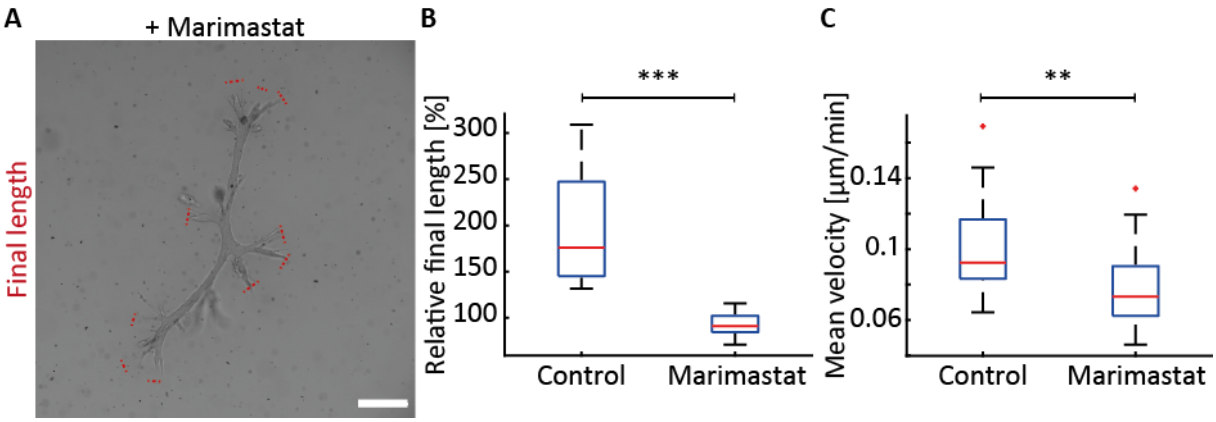

Figure 5-12: Matrix degradation enables branch elongation. A *Representative branch elongation after treatment with 10 µM Marimastat. Dotted red lines refer to the final branch tip.* ***B*** *In the time course of 24 hrs branches do not extend after treatment with Marimastat.* ***C*** *Cells within organoids treated with Marimastat exhibit a significant reduction in their mean velocity. Scale bar, 200 µm (**A**).*

Remodeling of the collagen microstructure

In order to invade the matrix cells do not only degrade the collagenous matrix but further remodel and sense the microstructure and mechanics of their environment. Recent publications have demonstrated that in single cell experiments aligned collagen fibers act as guiding cues for 3D cell migration and are used for mechanical signaling between neighboring cells[97]. During organogenesis such aligned fibers are thought to arise from the collective contractility of the cell aggregates, which in turn are used as further guiding cues for the invasion process[92,98]. The luminal organoids exhibit a proliferation-driven invasion with only little deformations within the ECM. As described above, the deformations are spatially limited to the near field of invading branches. In order to analyze the microstructure of the collagen network, luminal progenitor cells were cultivated in fluorescent collagen. After day 10 in the cultivation the collagen network was analyzed. Aligned fibers in front of the branches are detectable (Fig. 5-13A). With increasing angle to the branch axis, this fiber alignment reduces and thus resemble the deformation field of the tip cells. At the sides of extending branches the collagen network does not show any aligned collagen fibers (Fig. 5-13C). Here, no preferred orientation is observable as seen when calculating the degree of alignment, as defined in chapter 3.3.4. In particular, the alignment field at the sides resembles the random oriented collagen network in control measurements, where no organoids are present within the matrix (Fig. 5-13B). Taken together, the small deformations of the tip cells are sufficient to significantly align the collagen network in front of them. In turn, those collagen fibers are then used to guide the further outgrowth. In addition to the fiber alignment, a minor accumulation of collagen can be observed at the boundary between organoid and ECM. This compacted layer of collagen results from the earlier invasion process during which the tip cells push the collagen fibers to their sides. The accumulation is later further intensified by the branch thickening.

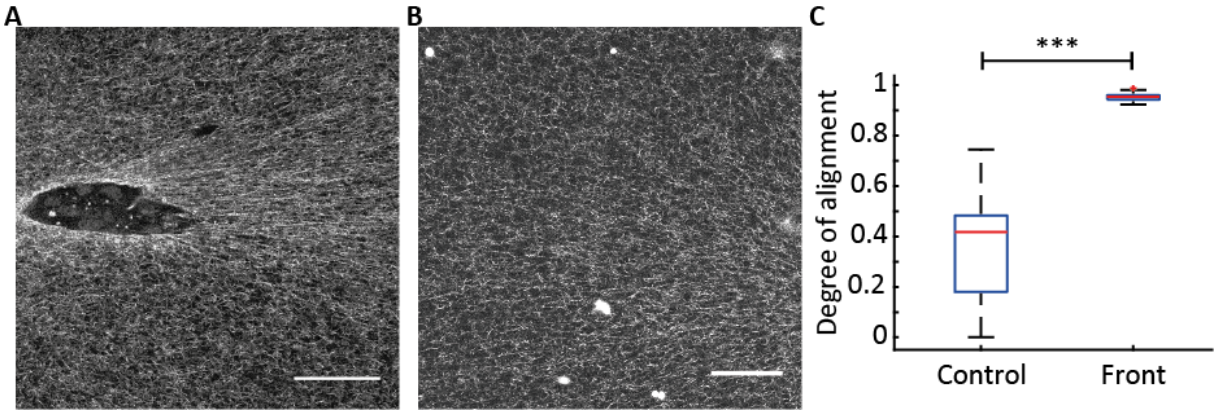

Figure 5-13: Collagen alignment in front of invading branches. A *In front of invading branches aligned collagen fibres are detectable. At the sides less alignment is observable.* ***B*** *In the far field of the organoids no collagen alignment is observable.* ***C*** *In front of invading branches a significant fibre alignment compared to control measurements is detectable. Scale bars, 50 µm (**A**, **B**)*

5.3 Conclusion and Outlook

5.3.1 Comparison of 2D and 3D cell culture assays

On 2D substrates only marginal differences in the cell properties cultivated with and without ROCK-inhibitor are observable. During migration, cells exhibit similar velocities, cell-cell adhesion and 2D migration modes. As a consequence of the inhibition of the ROCK signaling cascade, the underlying actin network only shows small differences. Cells within media without the ROCK-inhibitor, express a more pronounced lamellipodia and stress fibres. However, individual stress fibres were detected in both conditions. A significant difference was observed only in the proliferation rates. Cells cultivated with ROCK-inhibitor proliferated slower than cells without ROCK-inhibitor. In contrast, in a 3D collagen matrix the two different culture conditions led to completely opposing cell aggregate morphologies, a different contractile behavior and a contrary migration within the aggregates. Cells cultivated without ROCK-inhibitor mostly grew into spherical-like aggregates, which did not exhibit any branches. These aggregates exhibit a marked omnidirectional deformation field, while the cells only commuted within the structure. In comparison, cells with a reduced contractility grew with only minor ECM deformations into largely branched organoids, mimicking the morphology of the human mammary gland *in vivo*. Further, the cells collectively migrated in the direction of the branch extension.

The most obvious difference of 2D and 3D assays is the spatial confinement of the cells given by the collagen network. In order to migrate and to proliferate, cells need to interact with their environment. Such an interaction is displayed by matrix remodeling such as matrix degradation by matrix metalloproteinases or collagen fibre alignment. Therefore, cells need to apply forces on the individual collagen fibres. It is suggested that in 3D the forces are similarly generated *via* acto-myosin as during 2D cell migration[99]. In particular, the force built-up is highly dependent on the ROCK-pathway which regulates the phosphorylation of myosin light chain and thus the contractility. In comparison, on 2D substrates cells might need to apply lower traction forces in order to migrate as there is no spatial restriction given. The partial reduction of contractility by addition of 5 µM Y-27632 seems to be too less to affect cell migration. However, the described differences may not completely rely on the different extracellular confinement in 2D and 3D but can also be the result of differing biochemical cues. For instance, it has previously been demonstrated that cells cultivated on 2D substrates exhibit a change in their morphology, phenotype and polarity in comparison to freshly isolated cells from their tissue of origin[100]. Further, the cell lines cultivated in 2D exhibit a marked difference in their gene expression[101]. In comparison, in 3D assays specifically mimicking the ECM *in vivo* these properties are conserved to a higher degree, enabling a more profound analysis and comparison[102].

In summary, it has to be noted that caution is needed when transferring 2D observations to 3D or even *in vivo* phenomena. As demonstrated, even when in 2D only marginal differences are observable, the same tested conditions in 3D lead to drastic differences. Especially the

ECM with its additional adhesion sites as well as spatial confinement can trigger different biochemical signaling pathways and enables completely different migration modii as in 2D[13,28]. The data suggests that it is specifically the interplay between proliferation and contractility, which drives the different cell aggregate morphologies in 3D. In 2D the interplay has only a minor impact on cell migration.

5.3.2 Luminal branch elongation model

The presented results of the 3D assay of primary luminal cells with the addition of the ROCK-inhibitor Y-27632 summarize into a non-contractile proliferation-driven branch elongation model, which is facilitated by the individual matrix invasion of the tip cells. Specifically, proliferating cells within the organoid body lead to an increasing amount of cell mass, which in turn leads to an internal outward pointing pressure. In combination with the tight cell-cell coupling *via* E-cadherin, cells collectively migrate outward. The invasion into the ECM at the front of the branch is accomplished by the tip cells, which degrade the collagen by the use of MMPs. The invasion speed is remarkably slower than the migration speed of the stalk cells, that leads to a jamming of the cells. Consequently, cells exhibit a stop-and-go motion or in rare occasions also a temporary inward pointing migration. However, during invasion, tip cells not only degrade the ECM in front of them but also noticeable align the surrounding collagen network by minor contractions. The aligned collagen fibers guide the further migration direction of the tip cells and thereby the overall branch elongation. However, branches do not only exhibit a single tip cell but can also be guided by several cells. If there are multiple tip cells, it can occur that those cells invade the ECM in diverging directions and thus lead to the formation of two new branches. As the migration direction is predominantly parallel to the branch axis with no ECM invasion observable perpendicular to the branch, side branching mainly occurs at the tip of a branch. Only in rare cases new branches arise at the side of an already existing branch.

It has been demonstrated in this chapter that branching morphogenesis of the luminal organoids highly depends on the endogenous contractility of the individual cells. A reduction of the contractility promotes an arborized branched organoid morphology and invasive behavior. Only small deformations at the tip of the branches are sufficient to align collagen fibers in order to guide the further elongation process. In particular, the ROCK-Myosin II signaling cascade seems to have predominant impact on cellular migration and organoid growth efficiency. Without ROCK-inhibition the increased contractility promotes individual cell migration and thus hampers collective cell migration. In addition, the increased contractility enables that all cells mechanically interact with their environment. As a result, an omnidirectional deformation field occurs, which prevents a tip cell establishment. Conclusively, no cell triggers the formation of a branch. This marked dependency on the ROCK pathway is coinciding with observations found in immortalized mammary epithelial cells and in epithelial kidney cells[29,103]. In both cases, matrix invasion into a collagenous matrix is only enabled by ROCK inhibition.

In summary, the balance between cell-cell adhesion, contractility, migration and proliferation as well as matrix degradation seems to be key to understand branching morphogenesis of primary human luminal progenitor cells. However, the exact mechanism how all those physical parameters are connected to biochemical signaling pathways needs further attention.

6 Mechanical plasticity of the ECM directs branch elongation in human mammary gland organoids

In nature, organs like kidney, lung, pancreas or mammary gland exhibit a similarly branched architecture[104–107]. Their expansion into a tree-like, ductal epithelium is summarized into a universal description called branching morphogenesis, which is orchestrated by a complex interplay of biochemical and mechanical guiding cues[37,91,108]. Specifically, the extracellular matrix surrounding the organ is a major cue sculpting the resulting organ[109,110]. For instance, aligned collagen fibres guide the three-dimensional cell migration and enable force-transmissions between neighbouring cells[97,111]. Further, the ECM modulates cell-ECM invasion by its density, pore size, mechanical stiffness and matrix composition[27,90]. However, the growth of each organ depends on organ-specific biochemical, mechanical and structural cues and highly differs in-between the organs as well as between different species. Thus, the detailed process of branching morphogenesis has to be analysed for each system separately. In the case of the highly branched mammary gland, organoids from the mice as well as from human cells have been established as model systems[112,113]. While mammary gland organoids derived from mice cells are mainly cultivated in Matrigel and form densely packed networks, human cell-derived organoids in a collagenous environment branch into an arborized ductal network, nicely resembling the architecture of the mammary gland *in vivo*[9,38]. In human mammary gland organoids, the according branch elongation seems to be guided by protrusive leader cells[53]. However, the detailed elongation process as well as the cell-ECM interaction remains elusive.

In this chapter, the development of human mammary gland organoids derived from single primary basal cells is investigated. Therefore, static structure analysis and immunostainings are combined with dynamic live-cell imaging over several days. Further, branch elongation is manipulated by precise laser-ablation and treatment with various inhibitors affecting for instance matrix degradation, contractility or cell-cell adhesion. Further, a detailed analysis of the collagen structure and the network remodelling during branch expansion will be conducted. As a result, it is demonstrated that branching morphogenesis of human mammary gland organoids highly depends on the non-linear and plastic mechanical properties of the extracellular matrix. During elongation, the strong cell-cell adhesion and collective cell migration leads to an integration of the individual cell forces which lead to high anisotropic ECM deformations. In turn, these deformations enable a plastic remodelling of the collagen network. Such network remodelling results in the formation of a mechanical stable and plastic collagen cage covering the organoids. Its mechanical stability facilitates the tension built-up within the branches. Ultimately, the cage directs further elongation in combination with plastically aligned collagen fibers in front of the branches.

6.1 Basal organoid assay

In the time course of two weeks, primary human basal cells proliferate within the collagenous matrix and form multicellular branched aggregates, consisting of more than thousand cells. The developing organoids highly mimic the morphology of the mammary gland *in vivo* as they develop primary, secondary and tertiary branches and as their branch tips undergo alveologenesis and round up. Accordingly, the resulting organoids are denoted as Terminal

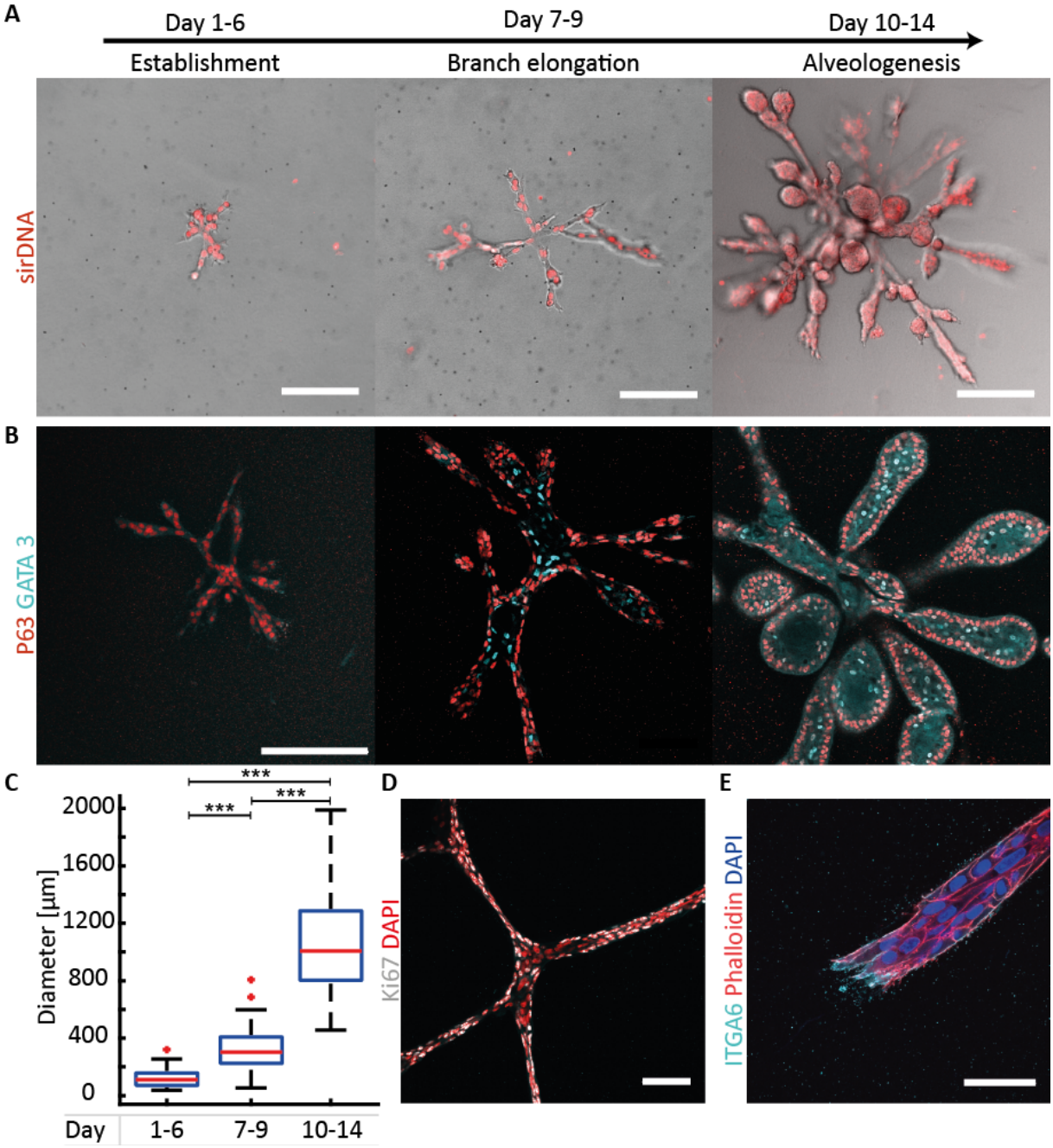

Figure 6-1: Temporal organoid morphology. ***A*** *Organoid morphology at the different developmental stages. Nuclei are labelled with 10 µM sirDNA.* ***B*** *Expression of basal-like (p63) and luminal-like (Gata3) markers at the different developmental stages.* ***C*** *Organoid diameter at the different developmental stages.* ***D*** *Cells proliferate throughout the whole organoid as demonstrated by expression of Ki67.* ***E*** *Branches adhere to the collagen via integrin α6 and exhibit aligned actin fibers within the branches. Nuclei are visualized with DAPI. Scale bars, 200 µm (**A**), 100 µm (**B**), 50 µm (**D**, **E**).*

Ductal Lobular Unit (TDLU) like structures. However, beside branched organoids also star-like structures evolve, which are characterised by a dense cell accumulation in the middle and thin branches growing outwards. These structures mainly develop as a result of a poorly polymerized collagen or inferior culture conditions and should not be analysed nor be denoted as organoids. In addition, within the used media the luminal subpopulation of seeded cells only develops into small spheres or elliptical aggregates and thus are obviously different from branched organoids derived from basal cells.

In time, organoid development can be divided into three developmental phases based on their morphology (Fig. 6-1A). From day 1 to 7 cells are in the establishment phase, which is followed by a ductal elongation phase from day 7 to 11. From day 11 to day 14 organoids reach their alveologenesis phase and develop into their final morphology. In particular, during the establishment phase the small rod-like geometry with an organoid diameter between 150 µm and 250 µm is characteristic. Already in this phase, the cell aggregates exhibit rudimentary branches and do not develop from a spherical structure. During the ductal elongation phase, these branches elongate, invade into the ECM and side branch into primary, secondary and tertiary branches. Further during the elongation phase, branches within the organoid centre widen and develop a bilayered cell architecture. Once cells within the organoid permanently loose the contact to the ECM, basal-like marker such as p63 get downregulated and an increased expression of luminal-like markers such as GATA3 can be observed, similar to the polarization observed *in vivo* (Fig. 6-1B). Ultimately, the development of the organoids is finalized by the alveologenesis phase. Hereby, branches stop invading into the ECM, shorten and develop round terminal end buds at the tip. In addition, at the end of development a lumen connecting the individual branches can be observed and the polarized expression of lineage markers intensified. The diameter of the resulting structures can span up to several millimetres (Fig. 6-1C). Proliferation is not spatially restricted but can be seen throughout the whole organoid (Fig. 6-1D). Further, at the tip of the invading branches filopodia-like structures are observable and an increased expression of integrin alpha-6 is detectable, indicating an invasive branching process (Fig. 6-1E). Concomitant with the organoid growth the freely floating collagen gels shrink up to half their initial size during the two weeks of development, indicating a distinct mechanical interaction of the cells with their ECM.

6.2 Boundary conditions steer organoid development

Organoid morphology and in specifically alveologenesis can be stirred by changing the boundary conditions of the collagen gels. While in freely floating collagen gels branched organoids grew into TDLU-like structures, organoids in attached collagen gels grew into branched structures without undergoing alveologenesis (Fig. 6-2A). However, alveologenesis of organoids grown in attached conditions can be triggered by detaching the collagen gels from the walls. As a result, the branches collapse towards the organoid centre and round up in the time course of three days[9].

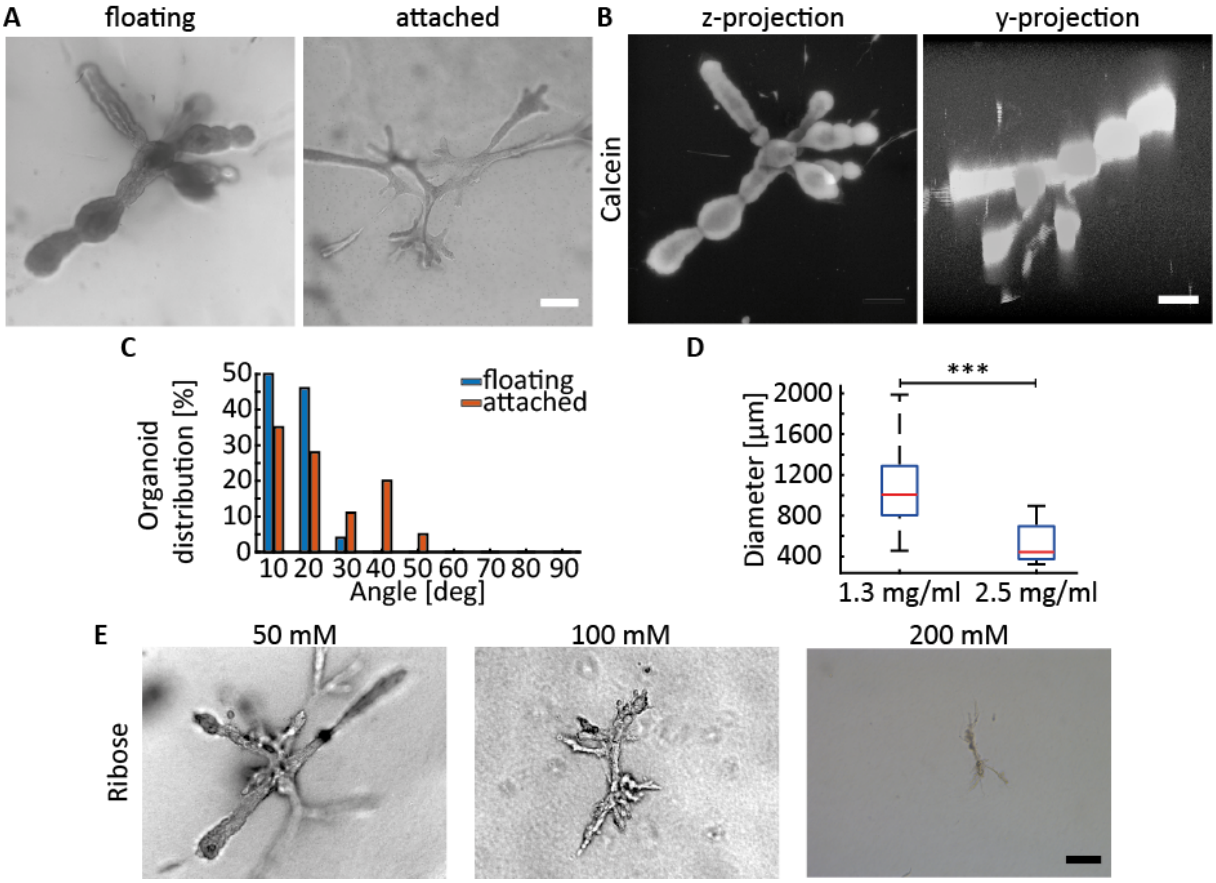

Figure 6-2: Boundary conditions affect organoid morphology. ***A*** *In floating gels organoid develop round alveoli, while branches in attached gels stay straight.* ***B*** *Organoids mainly spread in xy-direction and only show a slight expansion in z-direction. Organoid volume is visualized by Calcein staining.* ***C*** *Organoid orientation of the main axis to the xy-plane.* ***D*** *Organoid diameter in dependency of the collagen concentration.* ***E*** *Organoid morphology in collagen gels treated with different amounts of Ribose. Scale bars, 200 µm (**A**, **B**), 100 µm (**E**).*

In order to further reveal the impact of the boundary conditions on the organoid morphology, the position of grown organoids in dependency on their position within the gel, their related orientation towards the boundary and their growth efficiency in dependency on the gel volume was analysed. Hereby, it was observed that organoids mainly branched parallel to the to the bottom of the plate, while individual branches only slightly oriented up- or downwards (Fig. 6-2B, 6-2C). Further, organoids grew at any position in the gel independently on the distance to the boundary and thus did not exhibit a preferred position within a gel. However, an increased rate of alveologenesis was observed in close proximity to the edge of the gel.

To further vary the boundary conditions, the mechanical properties of the collagen network was modulated by two different approaches. On the one side the collagen density was increased from 1.3 mg/ml to 2.5 mg/ml and on the other side the mechanical properties of the collagen network were stepwise modulated by treatment with different amounts of Ribose while the collagen density was kept at 1.3 mg/ml.

Small variations in the collagen density did not affect organoid growth. Here, between 0.7 and 1.7 mg/ml cells kept branching into TDLU-like structures. In contrast, at higher collagen concentrations of 2.5 mg/ml cells grew into significantly smaller but still branched structures

(Fig. 6-2D). Yet, cells lost their capability to undergo alveologenesis. At such high concentrations organoid growth was either hampered by the increased stiffness or by the changed network structure, as an increase in collagen concentration leads to smaller pore sizes. To mainly steer the mechanical response function of the collagen gels without drastically altering the network architecture, the collagen was treated with ribose prior to polymerization. Thereby, the final ribose concentration was varied between 0 and 200 mM. Previously, it has been demonstrated that within the regime between 0 and 100mM Ribose no visible effect on fiber distribution or network architecture is observable[56]. Yet, a further increase to 200 mM Ribose led to the formation of thicker collagen fibres, which originated from an alternating polymerization dynamic. However, it was specifically shown that the collagen modification has no drawback on cell proliferation. As a result, organoid morphology and growth was modulated using Ribose treated collagen gels (Fig. 6-2E). Basal cells embedded in collagen gels treated with 50 mM Ribose did grow into branched structures with a size comparable to control measurements but did not undergo alveologenesis. A further increase to 100 mM Ribose limited the maximal organoid diameter to 450 µm and thus inhibited branching morphogenesis dramatically. In total, only rudimentary organoids developed, which did not undergo alveologenesis. At 200 mM Ribose even organogenesis was inhibited and no structures were observable anymore. Conclusively, basal cells are highly sensitive to their mechanical environment. As pointed out in chapter 3, especially the plastic remodelling is highly reduced in gels treated with Ribose, which might induce the different growth efficiency.

In general, organoid morphology highly depends on the choice of the ECM. Hereby, mainly Matrigel, collagen I or compositions of both have been established as standard matrices for various organoid assays. In the case of mammary gland, it was previously shown that aggregates of mammary cells MCF-10A grow into different morphologies in dependency of the composition of their ECM. While in collagen the aggregates exhibited an invasive phenotype, cells grown in Matrigel did not exhibit any cell protrusions and grew by a reduced cell-ECM interaction. Accordingly, primary basal cells were seeded into gels of pure Matrigel or collagen I and mixtures of both components. Mixtures were prepared at ratios of 30:70, 50:50 and 70:30. As a result, in Matrigel just single cells were detected, which did not proliferate. Likewise, in composite gels of Matrigel and collagen I no structures grew and if so, only spherical aggregates occurred. Contrary, in pure collagen gels highly branched structures

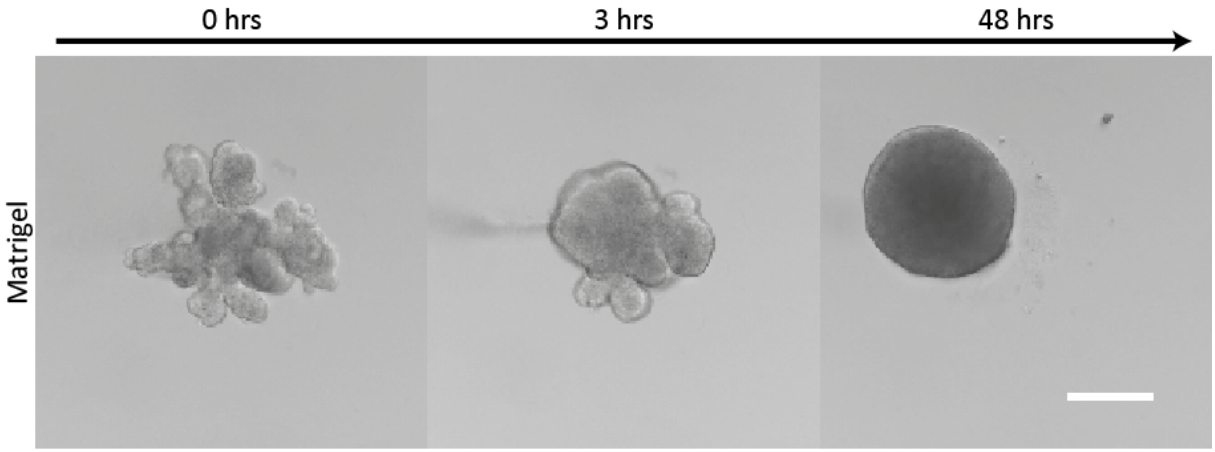

Figure 6-3: Temporal development of organoid transplants in Matrigel. *Within the first hours the branches of the organoid transplant collapse towards the centre, until after 48 hrs only a sphere is observable anymore. Scale bar, 250 µm.*

developed into TDLU-like structures. These results highlight the specificity of the biochemical and mechanical milieu of the ECM on the organoid development.

To overcome the impossibility of organoid growth in pure Matrigel but to investigate organoid morphology and behaviour in Matrigel, organoids were grown in pure collagen as described in chapter 3.2.2, then transferred to pure Matrigel and subsequently imaged for 48 hrs (Fig. 6-3). Specifically, organoids were picked between day 10 and day 14 once they branched and reached a minimal diameter of 600 µm. Organoids with and without alveoli were used. In order to transplant the organoids, first, collagen was depolymerized using 0.01 U/ml collagenase (Sigma) until the whole collagen was degraded. Second, a suitable organoid was picked using a 1000 µl pipette tip and transferred to fresh medium. Third, the organoid was mixed with Matrigel which was polymerized for 30 min at 37 °C. Finally, the gel was washed several times with media to remove left collagenase. During the following live cell imaging a drastic collapse of the branches towards the organoid centre was observed already within the first 3 hrs. After 48 hrs the initially branched organoid fully shrank to a spherical cell aggregate. However, after the collapse to a spherical cell aggregate, fluctuations in the surface were observable, indicating ongoing cellular rearrangements within the organoid. By additional nuclear labelling, such rearrangements and an ongoing cell proliferation were confirmed. Conclusively, this transplantation highlights the tremendous impact of collagen on basal organoid morphology.

In summary, these variations of the mechanical properties of the collagen network highlighted its strong influence on the organoid development and thereby motivated further investigations of the mechanical interaction of the organoids with their environment. So far, floating gels with a collagen I concentration of 1.3 mg/ml without any treatment appeared to be ideal for the formation of TDLU-like structures and were used for further analysis of their invasion of the ECM.

6.3 Branches non-continuously invade the collagen network

So far, mainly organoid morphology was used to propose key parameters for organoid growth and to judge the efficiency of organoid cultivation in various matrices. Thereby, it became apparent that the mechanical interplay of the organoids with their ECM is a crucial parameter driving branching morphogenesis. However, in order to specifically reveal the underlying cell-ECM interactions and to develop a model for branch elongation, live-cell imaging of growing organoids during their elongation phase was performed. To unveil the internal cellular dynamics, additional nuclear labelling was conducted.

6.3.1 Non-continuous branch elongation and ECM invasion

First, only brightfield live-cell imaging during the branch elongation phase of growing organoids was conducted. During branch elongation branches invaded into the ECM while they simultaneously deformed their surrounding ECM. In particular, branches did not continuously elongate, but exhibited a stop-and-go motion (Fig. 6-4A). Branch extension alternated between phases of branch elongation, branch shrinkage and phases in which the branch length did not change (Fig. 6-4B, blue line). The times of these phases strongly fluctuated between several minutes and hours and did not exhibit any particular frequency. However, as branches elongated phases of branch elongation were more prominent than branch contractions. Similar to branch length, also the branch width fluctuated over time and did not show a steady increase (Fig. 6-4B, red line). Yet, branch width did not increase as significantly as the related branch length. First during alveologenesis, branches grew bigger and rounded up at their tip. Further, the final branched morphology of the organoids was the result of several side branching events happening during the elongation process (Fig. 6-4C).

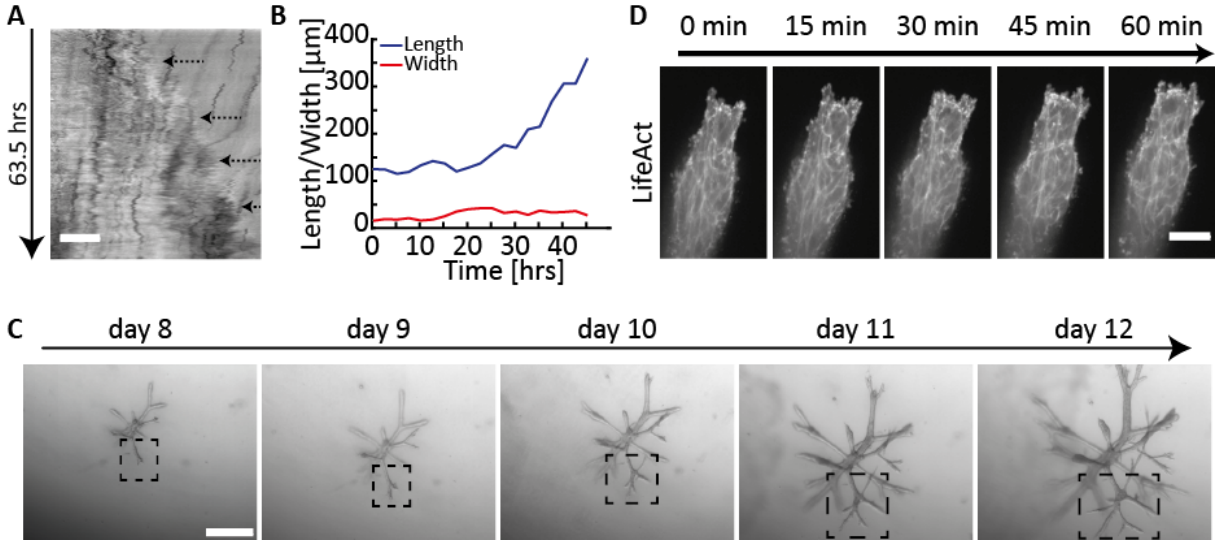

Figure 6-4: ECM invasion of the organoid branches. A *Kymograph of the branch elongation of a time course of 63.5 hrs.* ***B*** *Development of branch length and width over time.* ***C*** *New branches mainly form via bifurcation of the branch tip.* ***D*** *Branch tips invade the ECM by the formation of actin-rich filopodia-like protrusions. The actin network is visualized by LifeAct. Scale bars, 25 µm (A), 500 µm (**C**), 100 µm (**D**).*

Branches predominantly split up at their front *via* bifurcation, when two cells at the front started to migrate in different direction. As a consequence, two new branches formed. Only in rare cases side branching occurred as result of the formation of a new branch at the side of an already existing branch.

In order to further analyse the invasion process, live-cell imaging with a focus on the tip of the branch was conducted. *Via* brightfield imaging filopodia-like protrusions of the leading cells were detected. Hence, organoids were transfected in order to visualize the underlying actin structure of the extending branches. Thereby, a continual assembly and disassembly of actin-rich protrusions was observable (Fig. 6-4D). In time, cells penetrated the ECM at spatiotemporal varying adhesion sites and thereby sensed their mechanical environment. This mechanical testing of the ECM was further supported by the cell-ECM adhesion *via* Integrin α6. By additional nuclear labelling it became apparent that branches are guided by designated tip cells at the leading edge of the branch, which are followed by the so-called stalk cells in their back. However, tip cell identification was not permanent but changed in time (Fig. 6-5A). In particular, in the time course of 24 hrs in more than 50 % of the branches a tip exchange was observed (Fig. 6-5B). Hereby, in most cases an exchange was induced by either a stop-motion or inward pointing migration of the tip cells, while the stalk cells continued to migrate outward (Fig. 6-5C, 6-5D). Only in rare cases, tip cells were overtaken while they kept invading into the ECM. In addition, tip exchanges were more prone to occur in shorter and thinner branches (Fig 6-5E, 6-5F).

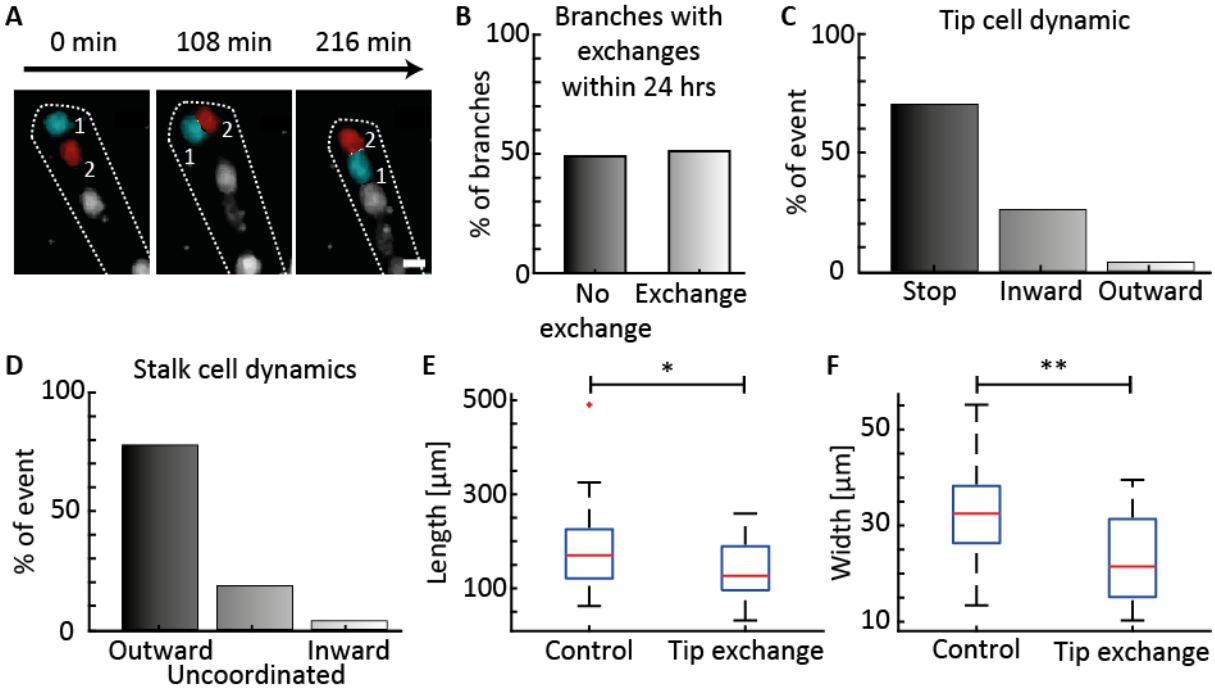

Figure 6-5: Tip cell dynamics. ***A*** *Tip cells exchange over time with their stalk cells.* ***B*** *Over 24 hrs in more than 50 % of the branches a tip exchange occurs.* ***C, D*** *During a tip exchange (**A**) tip cells mainly stop their invasion while (**B**) stalks exhibit an outward pointing migration direction.* ***E, F*** *Tip exchanges happen more likely in (**A**) shorter and (**B**) thinner branches. Scale bar, 10 µm (**A**).*

6.3.2 Basal organoid growth is accompanied by anisotropic long-ranged deformations

As already mentioned above, branch extension was accompanied by deformations of the ECM. To analyse the observed deformation field in detail, fluorescent tracer particles were embedded within the ECM and tracked over time (Fig. 6-6A). Thereby, it was demonstrated that the deformation field is highly anisotropic in space and time. While in the near field deformations of several microns towards the organoid were detected, at the sides only small deviations were observable (Fig. 6-6B). In particular, the displacements in the near field are partly up to eight times higher than at the sides. Accordingly, when calculating the angular dependent displacement in the near field, a clear decrease of bead displacement with increasing angle was observed (Fig. 6-6C). Further, the displacements only decayed slightly and were still detectable in the far field of the branches (Fig. 6-6D). Similar to the branch elongation, the deformations were also non-continuously in time. Here, phases of contractions of the ECM towards the organoid and relaxations away from them alternated in time. Within phases of contraction the magnitude highly fluctuated and exhibited power strokes during which pronounced but short deformations occurred (Fig. 6-6E). In comparison,

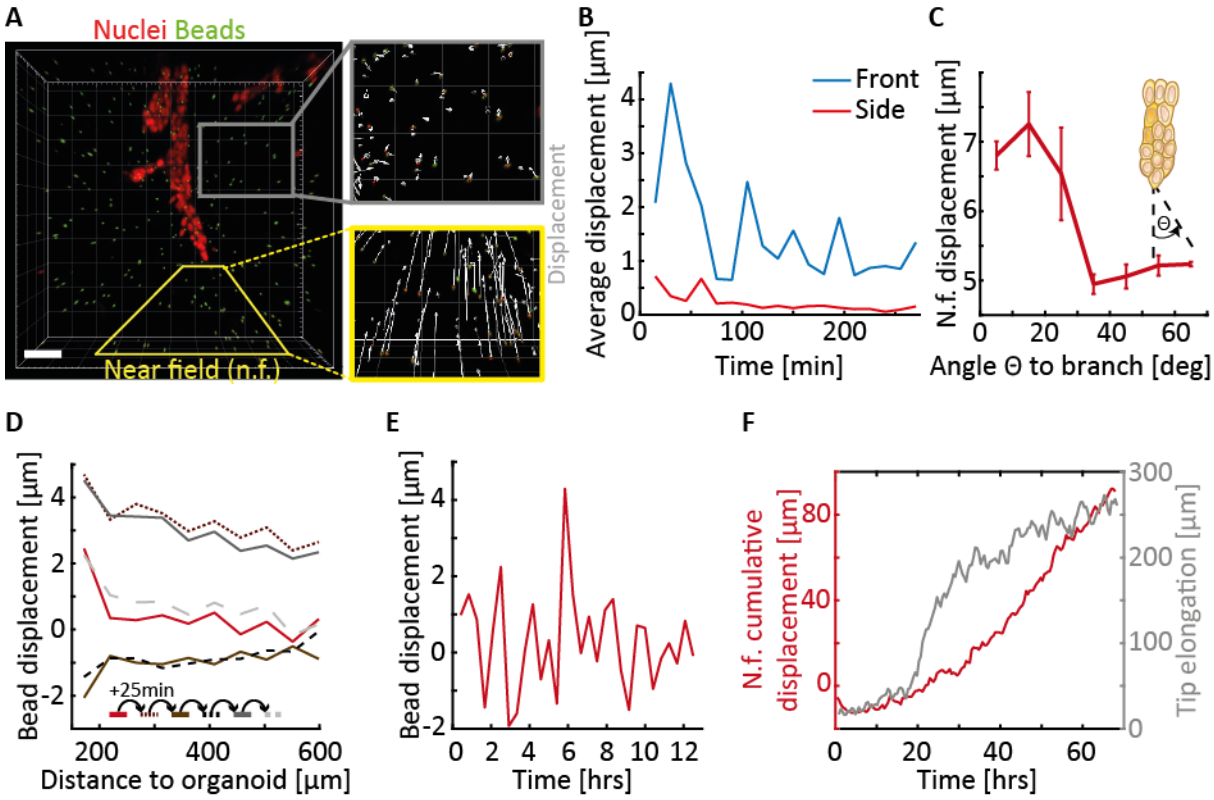

Figure 6-6: Branch extension is accompanied by anisotropic long-ranged deformations. ***A***, ***B*** *Bead deformations (grey arrows) are restricted to the front of extending branches, while at the sides only small deviations are detectable.* ***C*** *The bead deformations in front of the branches are highly dependent on the axis to the branch axis.* ***D*** *Bead deformations are still detectable in the far field but oscillate in time between contractions and relaxations.* ***E*** *In time, the bead displacement exhibits distinct fluctuations.* ***F*** *During tip elongation (grey line) the deformations (red line) drastically sum up. Scale bar, 70 µm (**A**).*

the magnitude of relaxations was in total lower and not as long-ranging as the preceding deformations. As a result, in the time course of more than two days the alternating deformations summed up to up to 100 µm, indicating nonlinear deformations of the collagen network (Fig. 6-6F).

In comparison, non-contractile luminal cells cultured within the same collagen gel and the same media did not exhibit such a deformation field (Fig. 6-7A, 6-7B). Their resulting deformations were in average more than five times lower than those of basal organoids (Fig. 7C). Further, luminal cells only grew into spherical aggregates driven by an internal pressure as consequence of their cell proliferation. However, in order to clarify that the origin of the

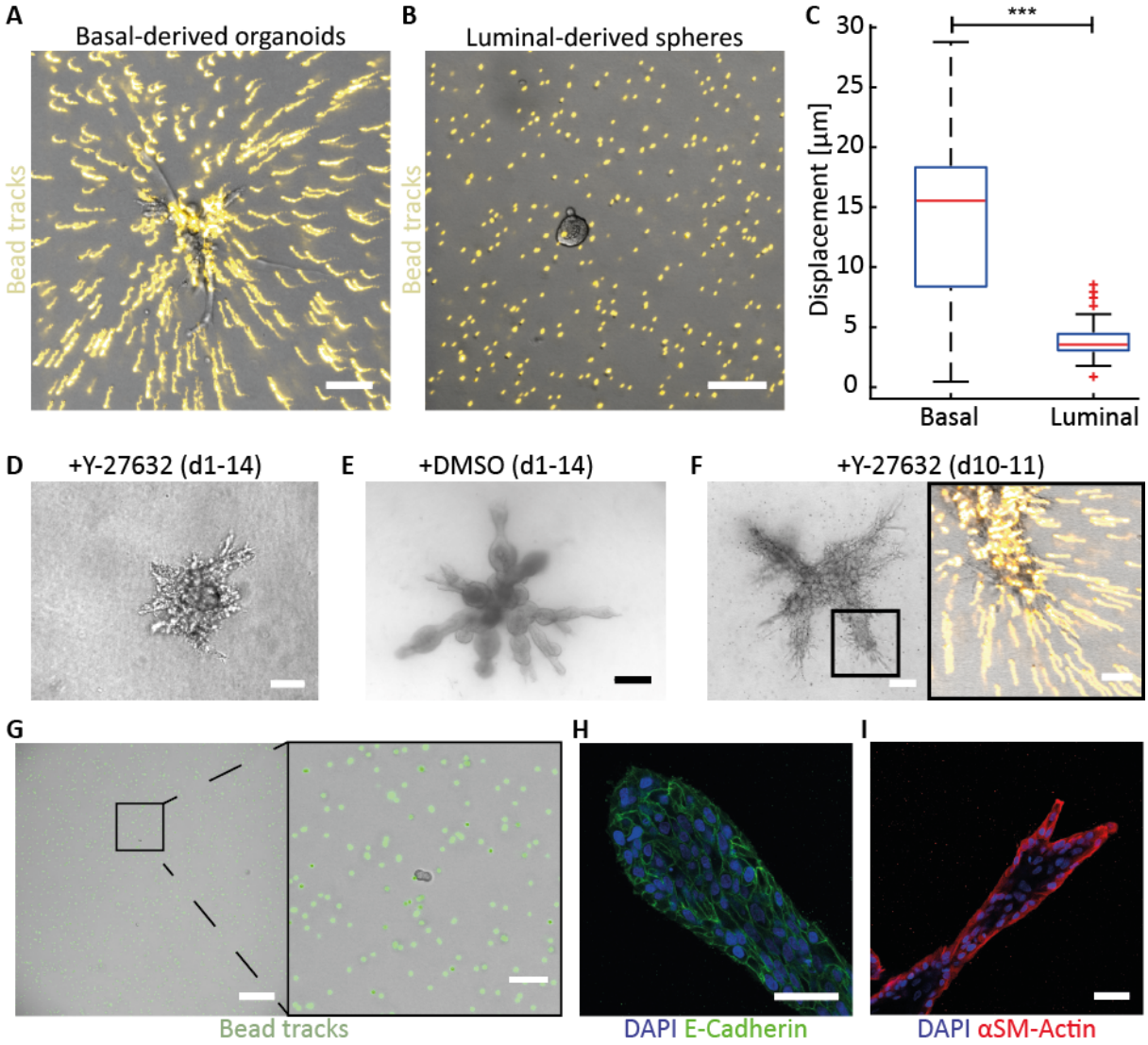

Figure 6-7: Contractility is prerequisite for organoid growth. A, B *(**A**) Basal-derived organoids exhibit a distinct deformation field, while (**B**) luminal-derived organoids exhibit no deformation field. Bead tracks are visualized in yellow.* ***C*** *Quantitative comparison of bead displacement during growth of basal organoids and luminal spheres.* ***D, E*** *(**D**) Organoid morphology after treatment with Y-27632 throughout the whole cultivation and (**E**) according DMSO-control.* ***F*** *Deformation field after addition of Y-27632 at day 10.* ***G*** *Deformation field of single basal cells.* ***H, I*** *Immunostainings against (**H**) E-cadherin and (**I**) αsm-actin. Nuclei are visualized by DAPI. Scale bars, 100 µm (**A-G**), 50 µm (**H, I,** zoom **E** & **F**).*

anisotropic long-ranging deformation field is caused by the contractile nature of the basal cells, their endogenous contractility was inhibited by the addition of the ROCK-inhibitor Y-27632. Indeed, upon treatment of the cells throughout the whole cultivation cells only grew into star-like structures and did not form branched TDLU-like structures (Fig. 6-7D). Further, when already branched organoids were treated with Y-27632 the anisotropic long-ranged deformation field abolished and branched elongation stopped (Fig. 6-7E). In contrast to control organoids, also stalk cells at the sides formed protrusions and penetrated the ECM. As a result, an omnidirectional but short-ranged deformation field emerged.

Yet, the higher contractility of the basal cells alone does not fully explain the observed long-ranged deformation field. In single cell experiments no deformation field was observable and first arose when cells built a multicellular branched structure, indicating a branch internal collective tension built-up (Fig. 6-7G). Indeed, by immunostaining a strong cell-cell coupling *via* E-cadherin was revealed (Fig. 6-7H). Further, basal cells at the outer layer of the branches exhibited a high expression of smooth muscle actin, a marker for highly contractile cells (Fig. 6-7I). In addition, phalloidin staining revealed thick actin cables connecting neighbouring cells, which further underlined the distinct cell-cell coupling and indicated a collective tension built-up.

6.3.3 Internal collective cell migration causes the deformation field

Brightfield imaging of growing organoids already indicates cellular rearrangements within the organoid. Similarly, within mouse mammary gland organoids it has been demonstrated that especially local cellular rearrangements drive the branch elongation[38]. In order to reveal the internal dynamics within the primary single cell derived human organoids, nuclei were labelled using 10 µM sir-DNA and organoids were imaged for several days. During live-cell imaging, extra precaution was needed for setting laser power and time between the frames, as a too high laser power with to short intervals in-between the frames caused cytotoxic cell apoptosis and thus impaired organoid growth. In particular, labelling efficiency and thus exact laser settings varied in-between the experiments. However, with the correct settings live-cell imaging was possible for up to 60 hrs. On longer time scales the nuclei signal slowly faded, which prevented a reliable nuclei identification and tracking.

Finally, long-term live-cell imaging revealed highly motile cells within the organoids with speeds of up to 1 µm/min. To unravel the exact velocity composition, the overall velocity was split in a parallel and orthogonal component (Fig. 6-8A). Therefore, the main branch axis was defined in the direction of ECM invasion with +-direction pointing towards the ECM. The resulting velocity calculation reveals that cells predominantly migrate in parallel direction to the branch axis and only show a negligible orthogonal velocity component (Fig. 6-8B). Further, branches exhibit phases of several hours during which only velocities either pointing inward or outward are detected throughout the whole branch. These phases of oriented migration reversed over time, meaning that all cells within the branches changed their migration direction collectively. The duration of this turning process was in the order of less than an hour until the cells within the branches established a similar total velocity as initially again. Overall, those phases of highly oriented migration with the concomitant turning phases indicate a collective cellular behaviour within the whole branch.

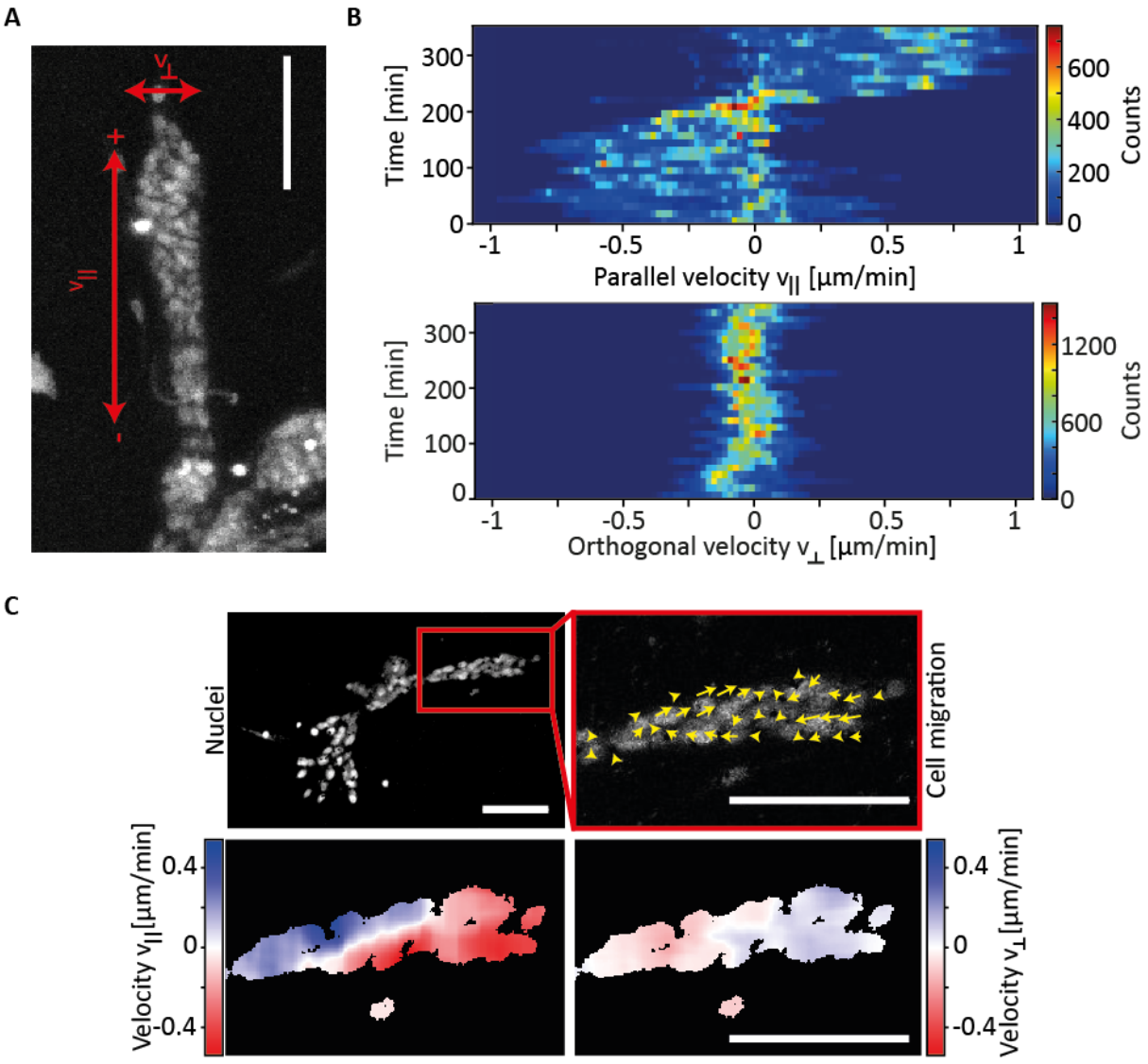

Figure 6-8: Collective cell migration. ***A*** *Definition of parallel and orthogonal velocity.* ***B*** *Temporal distribution of the parallel and orthogonal velocities.* ***C*** *Spatial velocity distribution within an elongating branch. Scale bars, 100 µm (**A**, **B**).*

To further examine the collective cellular migration, the spatial velocity distribution was calculated (Fig. 6-8C). The according velocity maps reveal clusters of several neighbouring cells with a similar velocity, demonstrating the spatial collectiveness of cell migration within the branches. In particular, during temporal phases in which all cells exhibit the same migration direction, the spatial clusters can even span the whole branch. However, in the time of direction reversal, branches exhibit several distinct clusters with opposing migration direction and different velocity as well as individually migrating cells (Fig. 6-8C). In time, these clusters disperse or merge with colliding clusters until a collective migration throughout the whole branch is established again. The origin of the initial direction reversal does not seem to occur at a specific branch position but varies in-between events (Fig. 6-9A).

In summary, the branch internal migration follows collective migration patterns in space and time (Fig. 6-9B). Hereby, cells within a whole branch migrate collectively for several hours in the same direction until they slow down and spatially establish smaller clusters with an opposing migration direction. These clusters as well as individual cells exhibit an uncoordinated migration and cell rearrangements until all cells within the branch turn their migration direction and migrate collectively again. Ultimately, the resulting migration direction is pointing in the opposing direction as in the beginning. In the following, this whole migration pattern will be denoted as back-and-forth migration. At the latest developmental stage, after undergoing alveologenesis the collective back-and forth migration evolves into a rotational migration of the cells within the developed alveoli. In short, this occurs as consequence of an isotropification of the internal tension field. The rotations are stable in time and are observable for more than 24 hrs without any direction reversal or slow down.

During branch elongation, both the deformation field as well as the collective cell migration reveal oscillating patterns. While the deformation field is characterised by long-ranged power strokes of the ECM towards the branches, the internal cell migration displays a back-and-forth migration within extending branches (Fig. 6-10A). Hence, a correlation analysis between the deformation field and internal cell migration was conducted. As a result, a correlation

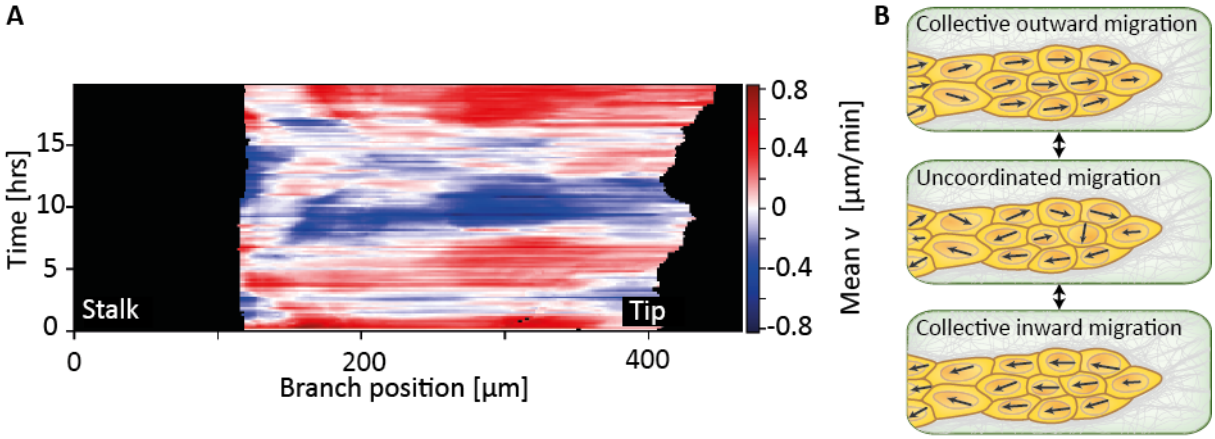

Figure 6-9: Velocity patterns within branches. A *Representative cell velocity in dependency of the position within the branch.* ***B*** *Cells within elongating branches collectively migrate either inward or outward with uncoordinated migration phases in-between.*

between both becomes apparent (Fig. 6-10B). When cells within the branch exhibit an inward pointing migration, clear ECM contractions toward the branch are detectable. In contrast, outward migrating cells cause no deformations or even lead to a relaxation of the ECM away from the branches (Fig. 6-10C). Nevertheless, small deformations within the ECM are also detectable without a pronounced inward pointing cell migration. Such small deformations are the result of the tip-cell driven matrix invasion and remodelling. In summary, it has to be explicitly noted that the long-ranged deformations which are still detectable in the far field of the branches are the result of the collective cell migration not the small deformations.

The correlation analysis demonstrates that the observed long-ranged deformation field during branch elongation is the cause of the collective internal cell migration. The tension built-up is further facilitated by the contractile nature of the basal cells and a strong cell-cell coupling *via* E-cadherin, as seen in according immunostainings. Indeed, lowering cell-cell adhesion by addition of HECD1, an E-cadherin antibody, inhibits the internal collective cell migration. In time, no back-and-forth migration is observable anymore and cells only wiggle around their initial position. Accordingly, total cell velocities drop to maximal 0.2 µm/min. In addition, parallel and orthogonal velocity component are in the same order of magnitude (Fig. 6-11A). As a consequence of the diminished cell migration, the initial anisotropic and long-ranged deformation field vanishes, as cells cannot build-up a significant tension anymore (Fig. 6-11B).

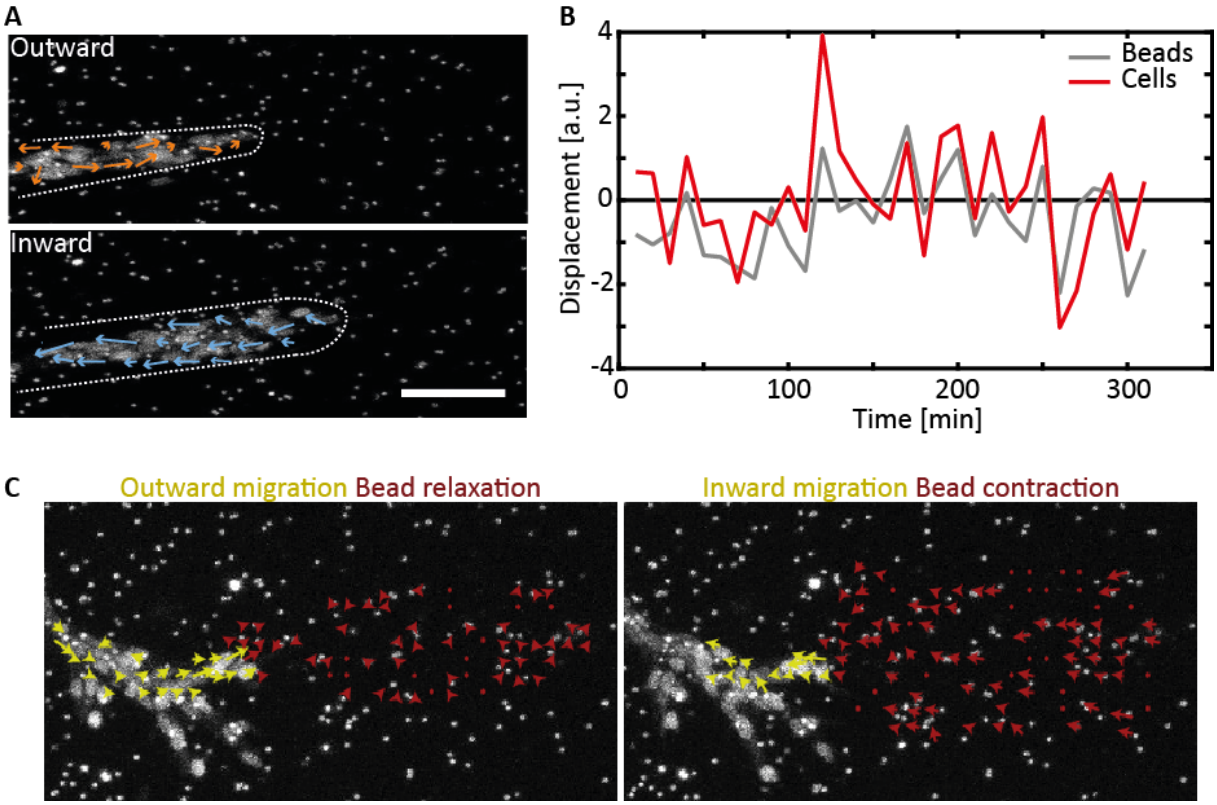

Figure 6-10: Cells collectively deform their surrounding ECM. A *Branches exhibit phases of collective inward or outward pointing migration.* ***B*** *Bead displacement and cell migration exhibit a visible correlation.* ***C*** *In phases of outward pointing migration, beads within the ECM relax. In comparison, in phases of correlated inward pointing direction contractions of the ECM towards the organoids are visible. Scale bars, 100 µm (**A**, **C**).*

Only small deformations in the near field are observable, which are only the result of the cell-ECM interaction of the tip cells.

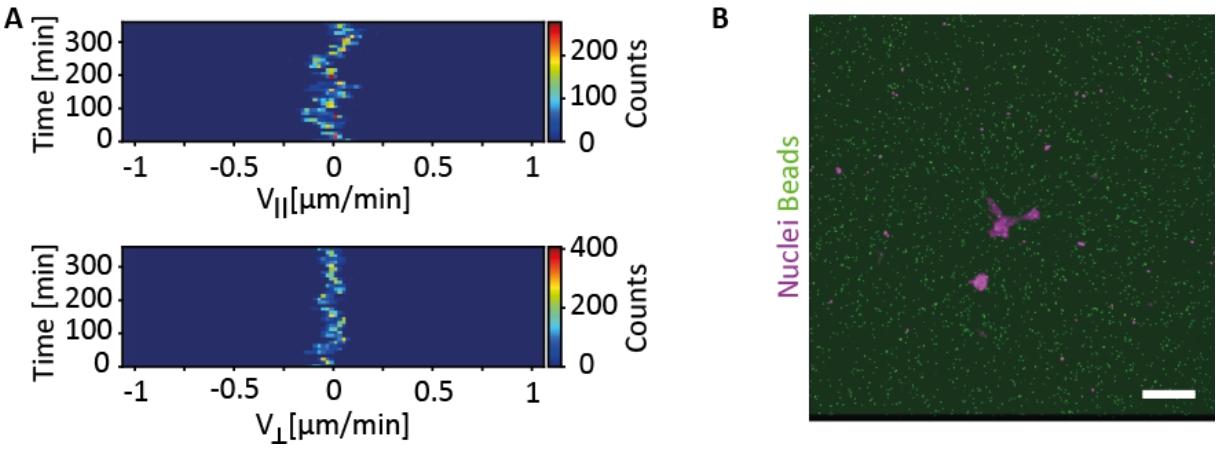

Figure 6-11: Cell migration and deformation upon treatment with HECD1. A *Organoids with reduced cell-cell adhesion exhibit drastically reduced migration velocities.* ***B*** *No deformations are detectable upon treatment with HECD1. Bead tracks are projected in green, nuclei are depicted in purple. Scale bar, 200 µm (**B**).*

6.4 Plastic ECM remodeling enables collagen cage formation

In previous publications, it has been shown that cell-ECM interactions lead to the remodelling of the underlying collagen network[97]. Thereby, individual cells as well as cell aggregates align collagen fibers, which then guide the further migration direction[98,114]. Accordingly, the collagen network structure and remodelling processes during branch elongation were analysed. Further, it has been recently demonstrated that explicitly the plasticity of an artificial network can regulate 3D cell migration. As the deformations during branch elongation are obviously in the nonlinear regime, the plastic nature of collagen was taken in account.

6.4.1 Branches generate tension equilibrium with the ECM

Before analysing the collagen network structure, first the underlying forces for the ECM deformations were examined. As the long-ranging and anisotropic ECM deformations result from the collective cell migration in combination with the endogenous contractility of the individual cells, the therefore required actin network was disrupted by the addition of Cytochalasin D (Fig. 6-12A, 6-12B). As a result, directly after addition branch elongation stopped and no deformations towards the branch were detected anymore. During the first hour after treatment the fluorescent beads within the matrix relaxed away from the branches. This relaxation clearly demonstrates the abolished tension within the branches. However, the beads did not relax towards their initial position but just covered a reduced deformation of the initial deformation field. After around four hours their relaxation stopped, and their position equilibrated (Fig. 6-12C). In addition to the ECM relaxation, a simultaneous passive elongation of the branches of around 10 % of their initial length was observed. Conclusively, the reduced relaxation highlights the plastic nature of collagen and reveals a restoring force within the collagen network pulling on the branches.

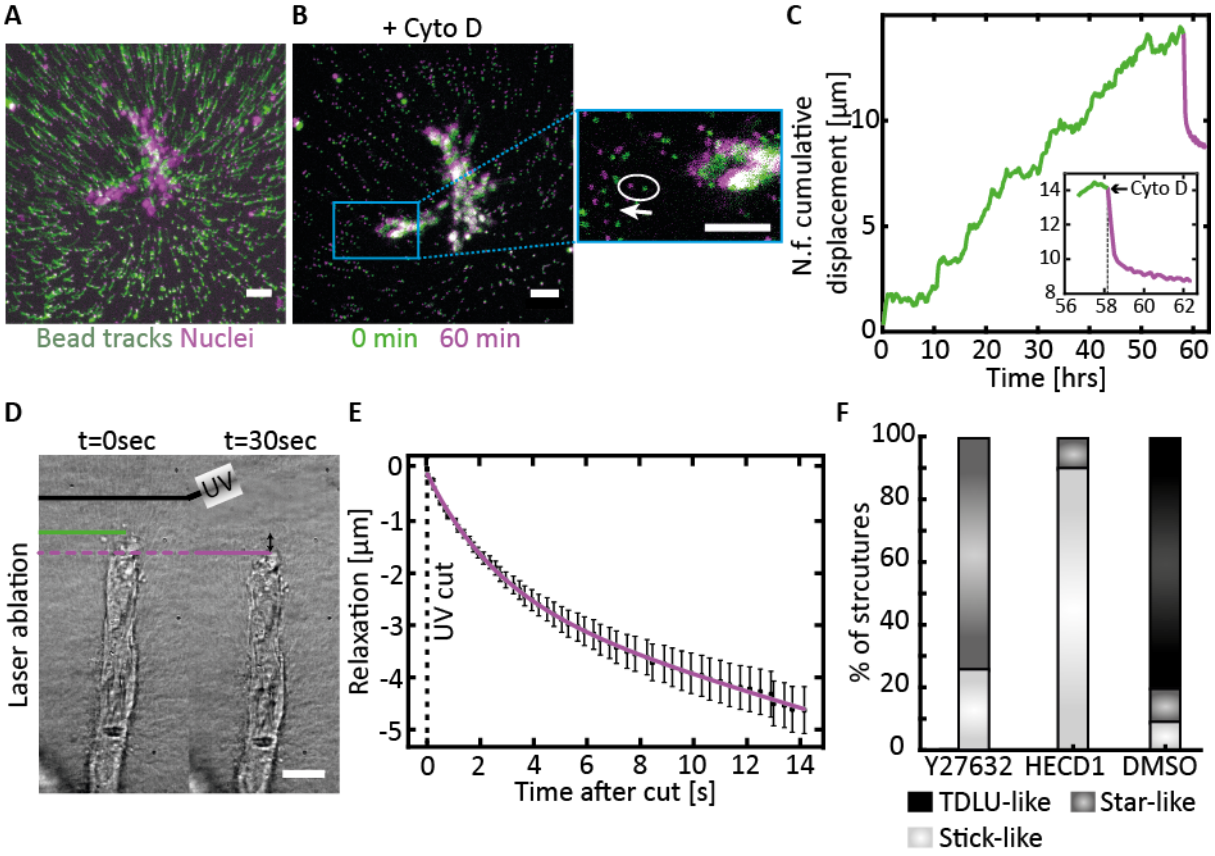

Figure 6-12: Investigation of tensile forces during branch elongation. ***A*** *During branch elongation beads within the ECM exhibit marked contractions towards the organoids.* ***B*** *After disruption of the actin network by addition of Cytochalasin D, beads relax away from the branch.* ***C*** *The deformations within the ECM only relax partly.* ***D*** *Laser ablation protocol in front of branches. The tip of the branch is tracked over time. The green line indicates the initial tip position, while the purple line indicates the last position.* ***E*** *Averaged branch relaxation after laser ablation.* ***F*** *Organoid formation is hampered after treatment with HECD1 throughout the whole cultivation. Scale bars, 50 µm (**A**, **B**), 15 µm (**D**).*

In order to analyse the opposing pulling forces of the ECM, UV-laser ablation experiments of the collagen network in the near field of the branches were conducted (Fig. 6-12D). In particular, UV-cuts with a length of 200 µm at a distance between 40 µm and 60 µm were carried out. The according branch behaviour was imaged, and the branch tip was tracked. Immediately after ablation, organoid branches contracted towards the organoid centre until their length equilibrated after around 20 seconds (Fig. 6-12E). Hereby, branches shrank in the mean 10 % of their initial length. This relaxation highlights again the cell-generated tension within the branch. Accordingly, as counterpart to the branch relaxation the ECM relaxed in the opposing direction, thus away from the organoid.

To judge the necessity of the underlying collective tension built-up for branching morphogenesis, two drug screenings affecting tension built-up were performed and the resulting organoid formation was quantified (Fig. 6-12F). On the one side, the endogenous contractility of the individual cells was reduced by the addition of the ROCK-inhibitor Y-27632 and on the other side, the collectiveness of tension built-up was inhibited by lowering cell-cell adhesion *via* the addition of HECD1. While the addition of HECD1 led mainly to the formation of stick-like but branched structures, the addition of Y-27632 enforced the formation of star-like aggregates. In both cases, the growth of TDLU-like structures was completely abolished.

Together, these observations demonstrate the collective tension built-up as prerequisite for branching morphogenesis and reveal a tension equilibrium between branches and ECM. While a disruption of the collagen network leads to branch shrinkage as a result of the branch internal tension, an opposing disruption of the actin network results in a branch elongation due to the restoring force within the ECM (Fig. 6-13A). As a consequence, cell invasion gets further guided by the restoring force of the ECM, which pulls onto the branch. Further, this tension equilibrium leads to plastic ECM deformations and thus enables an irreversible network remodelling (Fig. 6-13B).

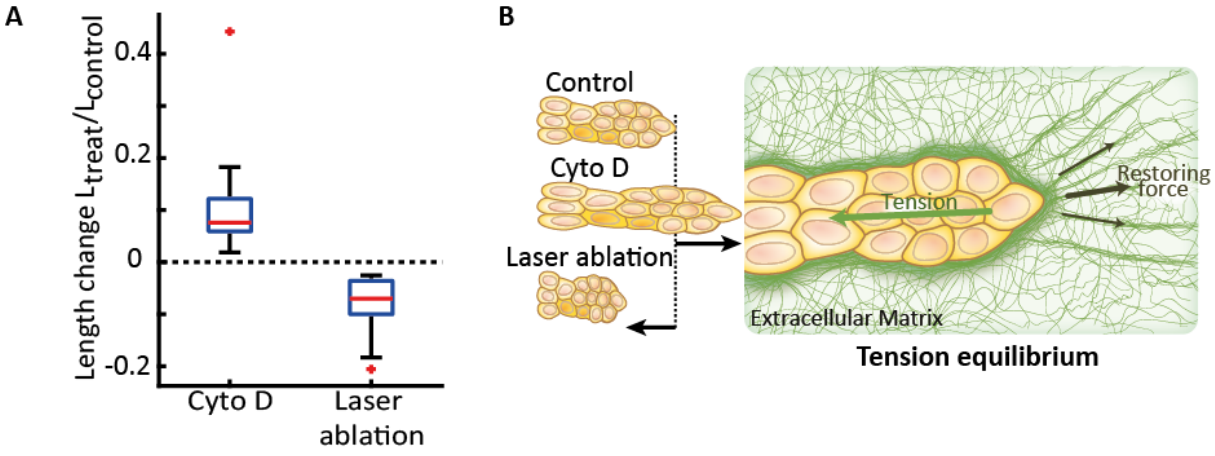

Figure 6-13: Branches exhibit a steady tension equilibrium. A *Upon treatment with Cytochalasin D branches extend, while laser ablation leads to a shrinkage of the branches.* ***B*** *The cells within the branches built-up a significant tension, which is opposing the restoring forces within the ECM.*

6.4.2 Plastic collagen fiber alignment guides branch elongation

To reveal the implication of the tension equilibrium and the concomitant plastic deformations on the collagen network, the underlying network structure was analysed in detail. By the use of fluorescently labelled collagen, individual fibres were imaged and monitored during the elongation and invasion process.

In general, a pure collagen network polymerizes into a fibrillary matrix with a defined mesh size in which individual collagen fibres were randomly oriented (Fig. 6-14A). In contrast, in front of invading branches, a densification of collagen as well as highly aligned collagen fibres and bundles were detected (Fig. 6-14B). With increasing angle to the branch axis, the degree of alignment reduced (Fig. 6-14C). Accordingly, at the sides a significantly lower degree of alignment was calculated. However, compared to control areas still a significant alignment was present, which resulted from the earlier invasion process. Hereby, tip cells did not continuously attach to the same collagen fibres but frequently changed their attachment sites during the invasion process (Fig. 6-14D). As a consequence, pronounced bundle formation appeared and disappeared in time at varying positions. In addition, the alignment at the sides highlights the plastic nature of collagen as at the sides no forces were applied from the cells to the ECM, which could have induced a fibre alignment. The underlying plasticity of collagen was further underlined by the fact that fibre alignment was conserved even after the branch internal tension was supressed by the addition of Cytochalasin D (Fig. 6-14E).

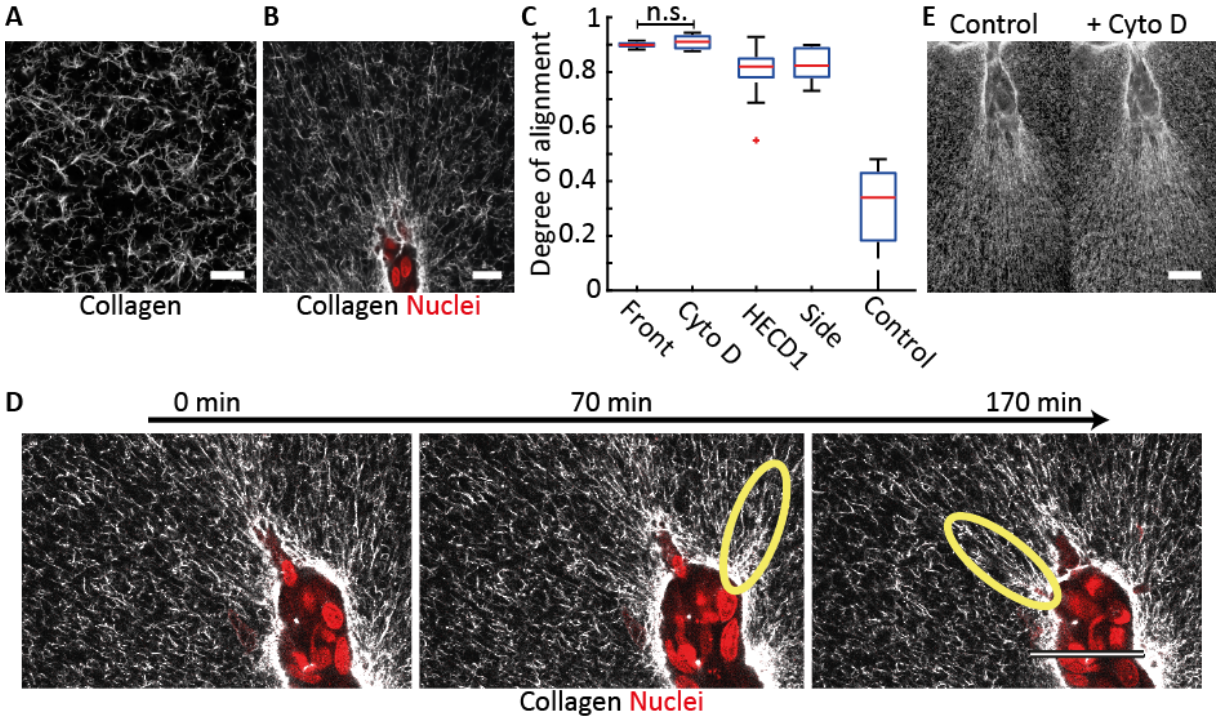

Figure 6-14: Collagen fibre structure in front of invading branches. A *In pure collagen gels no fiber alignment is detectable.* ***B*** *In front of branches aligned fibers are visible.* ***C*** *Degree of fiber alignment at various positions and after treatment with various drugs. The degree of alignment for the drug treatments were measured at the front of the branches.* ***D*** *In time, tip cells adhere to various adhesion sites of the collagen network.* ***E*** *Fiber alignment is conserved after treatment with Cytochalasin D and thus reveals the plastic collagen remodelling. Scale bars, 50 µm (**A, B, D**), 20 µm (**E**).*

In summary, the overall decrement of fibre alignment highly resembled the anisotropic deformation field during branch elongation and thus indicated that fibre alignment was caused by the extending branches. Indeed, a reduction of collective tension built-up *via* addition of HECD1 led to a significant decrease in fibre alignment. The hereby detected alignment only resulted from the individual cell-ECM interactions of the tip cells.

6.4.3 Tip cells drive ECM invasion by the use of MMPs

Despite the tension equilibrium between branches and ECM, tip cells invade into the ECM in order to create further accessible space for the stalk cells and in turn elongate the branches. By immunostaining and the use of LifeAct it has been shown that tip cells sense their environment by the formation of filopodia-like protrusions, while they adhere to the ECM by the expression of integrin $\alpha 6$. To specifically reveal the detailed and temporal resolved tip invasion process simultaneous live cell imaging of fluorescently labelled nuclei and labelled collagen was conducted (Fig. 6-15). During the invasion process nuclei stay at a steady position, while the cellular filopodia-like structures sense their mechanical environment by pulling on surrounding collagen fibers. During this, cells first create a small cavity within the collagen in front of the nucleus, which then successively widens. When this cavity is large enough, the nucleus squeezes through, compresses the collagen at its sides and settles at the new position in the front. The stalk cells expand into the new space and the invasion process starts from the beginning again. This invasion of the tip cells highly resembles the mesenchymal migration mode observed for single cells within a three-dimensional matrix and thus indicates an uncoupling of tip and stalk cells. In particular, stalk cells exhibit a collective back-and-forth migration, while tip cells exhibit a mesenchymal migration of a single cell aiming to invade into the ECM.

In addition, the tip invasion process is further exacerbated by the steady accumulation of collagen in front of the branches as consequence of the anisotropic long-ranging deformation

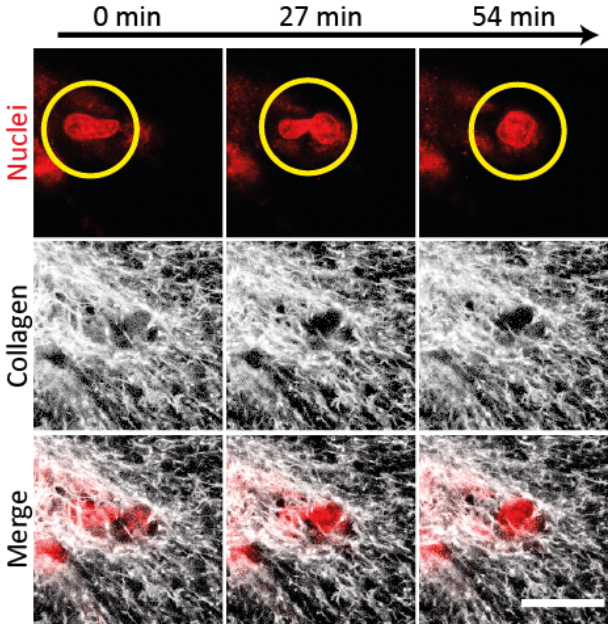

Figure 6-15: Single tip cell invasion. *To invade the ECM, nuclei squeeze through pores within the ECM. Nuclei are visualized by sirDNA. Scale bar, 20 µm.*

field towards the branch tip. In previous publications it has been shown that single cell invasion and branch elongation is facilitated by the expression of matrix metalloproteinases. To check the relevance of MMP expression for the basal organoids, immunostaining against MMP9, a prominent MMP during mammary gland remodelling, was conducted. Indeed, an expression of MMP9 can be observed at the boundaries between organoid and ECM (Fig. 6-16A). Especially, within the tip cells of the invading branch an increased expression is detectable and hints towards a distinct collagen degradation of the tip cells. To judge the importance of MMP activation during organogenesis, organoids were treated with Marimastat, a broadband MMP inhibitor. As a result, cells treated with 10 µM Marimastat throughout the whole cultivation from day 0 to day 14 did not grow into TDLU-like structures, but only formed thin stick-like but still branched structures (Fig. 6-16B). Hereby, branches grew significantly thinner, and the branched structures grew smaller compared to control organoids. To specifically elucidate the influence of matrix degradation during branch elongation Marimastat was added between day 7 and day 10 to already branched organoids. As control, organoids were first imaged for about 20 hrs in standard cell culture conditions. Subsequently, cell culture media was enriched with 10 µM Marimstat and organoids were imaged for further 20 hrs (Fig. 6-16C). As a measure, branch width and length were tracked during this procedure (Fig. 6-16D). While during the control measurement all branches

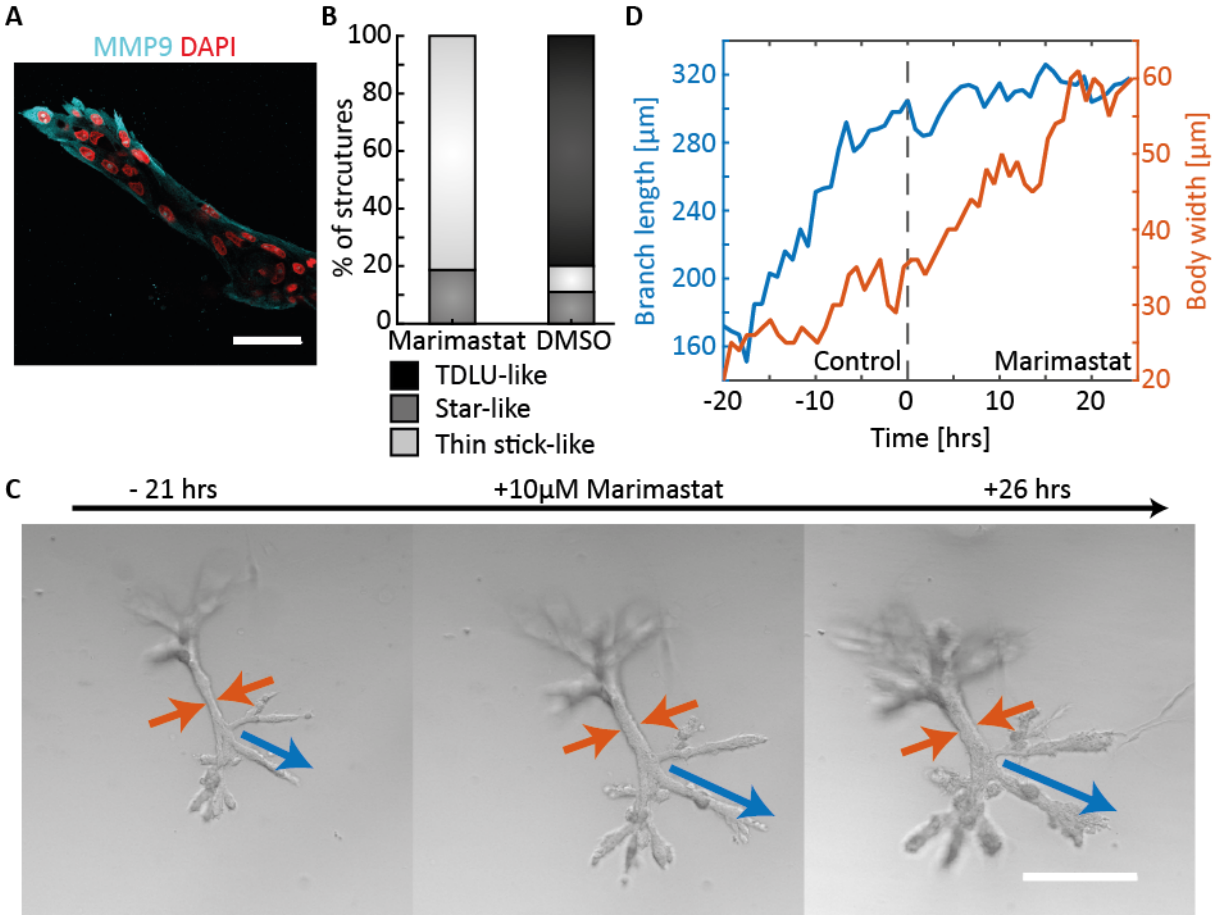

Figure 6-16: Branch invasion is facilitated by matrix metalloproteinases. A *Tip cells within the branch express MMP9. Nuclei are visualized by DAPI.* ***B*** *Upon treatment with Marimastat no TDLU-like structure grow, but mainly stick-like structures.* ***C, D*** *Marimastat stops branch elongation and leads to an increase in branch width. Scale bars, 50 µm (**A**), 300 µm (**C**).*

steadily elongated and invaded with the typical stop-and-go motion into the ECM, the addition of Marimastat abruptly stopped this invasion process and led to minor fluctuations of the branch length around the initial length. Throughout the whole measurement tip cells continuously adhered *via* filopodia-like protrusions to the ECM and unsuccessfully tried to invade into the collagen network. By additional nuclear labelling a steady proliferation was observed. In combination with the inhibited branch elongation, the ongoing proliferation led to a constantly increasing cell density within the branches which in turn led to a constant increase in branch width. In summary, these observations demonstrate matrix degradation to be prerequisite for organogenesis of primary human basal cells.

6.4.4 Basal organoids are mechanically encased by a plastic collagen cage

As seen during live-cell imaging, the long-ranging deformation field leads to a steady accumulation of collagen in front of the branches. During branch elongation, this accumulated collagen gets partly degraded by the tip cells *via* MMPs and partly compressed to the side of the branches as consequence of the tip cell invasion. Further, the collagen accumulation at the side of the branch gets amplified by the constantly increasing branch width. As a consequence, the growing organoids are fully covered by a thick layer of collagen, which will be in the following denoted as collagen cage (Fig. 6-17A). High resolution imaging revealed the porous structure of the collagen cage with pore sizes between 1 µm and 3 µm (Fig. 6-17B). By measuring the fluorescence intensity profile of the collagen cage and measuring the full width half maximum the according cage width was measured. After two weeks of cultivation the cage of fully grown organoids had a mean diameter of 5 (+/- 2) µm but became partwise up to 12 µm wide (Fig. 6-17C). Yet, during branch elongation phase the cage thickness was highly heterogeneous along the branch axis. While at the sides a pronounced cage was visible, a significantly lower accumulation of collagen was detectable at the front of the branch (Fig. 6-17D). During alveologenesis, also at the front collagen got accumulated and the cage at the front merged from the sides. As a result, the arising alveoli were fully covered by the collagen cage. However, by the inhibition of cell-cell adhesion throughout the whole organoid cultivation *via* HECD1 the collagen cage was still detectable but had a significantly reduced diameter of 1.8 (+/- 0.5) µm. Accordingly, the whole cage formation strongly relies on the collective cell migration and concomitant cell-generated tension built-up.

In order to reveal further components of the cage, immunostaining against prominent candidates of the basement membrane was conducted. Hereby, an increased laminin

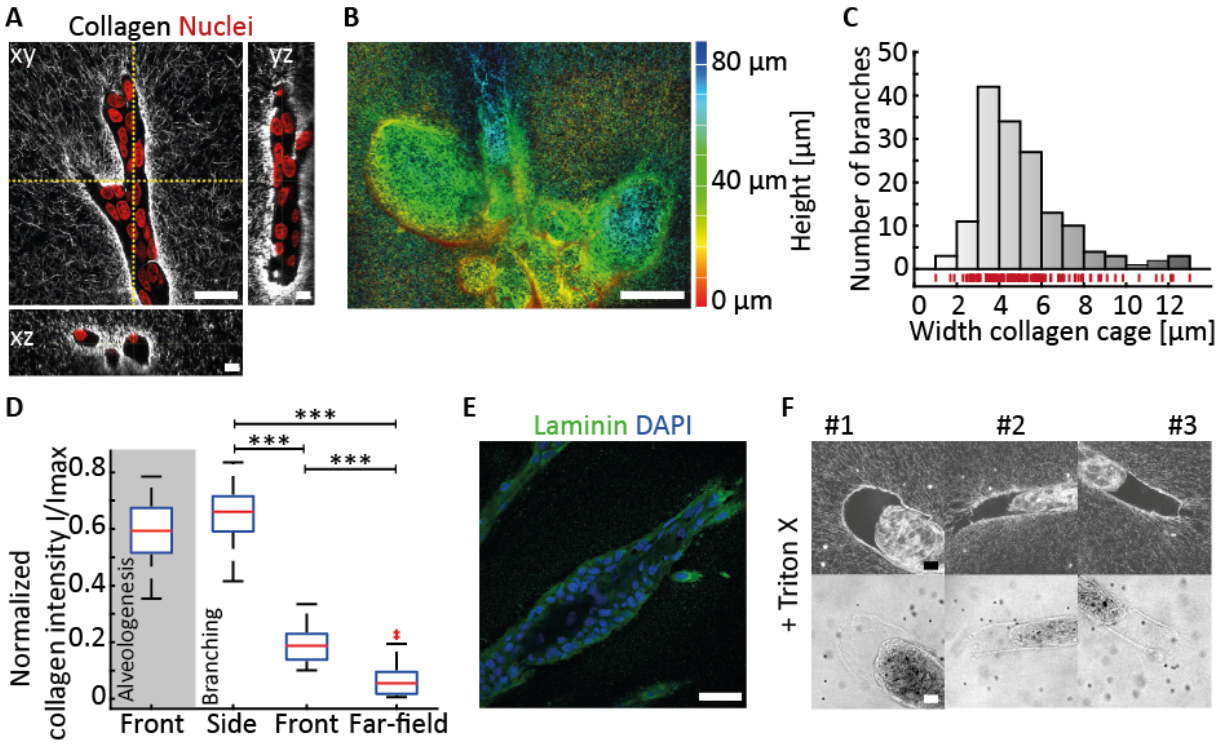

Figure 6-17: Organoids are encased by a plastic collagen cage. ***A*** *Organoid cultivated in fluorescent collagen exhibit a distinct collagen accumulation at their cell-ECM boundary. Nuclei are visualized with sirDNA.* ***B*** *High-resolution imaging reveals a porous collagen cage structure.* ***C*** *Distribution of the collagen cage width.* ***D*** *Collagen intensity at different positions of the branch. During alveologenesis the collagen cage around alveoli fully closes.* ***E*** *The collagen cage is further enriched with laminin.* ***F*** *The collagen cage is conserved even after treating the cells with Triton X. Scale bars, 30 µm (**A** xy), 10 µm (**A** yz & xz, **F**), 50 µm (**B**, **E**).*

expression was detected at the cell-ECM interface (Fig. 6-17E). Additional components such as Collagen IV or fibronectin were not detected.

As collagen is highly plastic under nonlinear deformations and plastically aligned collagen fibres were detected at the front of invading branches, the mechanical stability of the collagen cage was tested. Therefore, cells were permeabilized using Triton-X and the resulting collagen network structure was imaged. As a result, branches collapsed towards the organoid body, while the structure of the collagen cage was not affected (Fig. 6-17F). Even in the absence of the cell-generated tension within the branch, the cage persisted and was even visible in the brightfield, highlighting is mechanical stability and plastic nature.

As a consequence of the small pore size in combination with the broad cage diameter, the cage prevents cells to penetrate the ECM at the side of a branch and thus limits ECM invasion to the tip, where a significantly weaker collagen cage is detected. Accordingly, the collagen cage thereby prevents side branching from the sides of a branch and constrains side branching to the tip, where it then happens *via* bifurcation as shown in Chapter 6.3.1.

6.5 Conclusion and Outlook

6.5.1 Basal organoid growth is self-regulated by a mechanical feedback-loop

The presented results highlight that basal organoid development is highly dependent on the mechanical environment and specifically that branch elongation is dictated by a force equilibrium between the branch and its surrounding collagen network (Fig. 6-18A). Further, the presented results can be summed up into a self-enhancing mechanical feedback model, linking collective endogenous contractility of the cells with the mechanical plasticity of the extracellular collagen matrix (Fig. 6-18B). The resulting collagen cage covering the organoids mechanically stabilizes the branches and further guides the elongation process. Due to its stability, cells within the branch use the collagen cage as substrate to migrate on. In combination with the concomitant spatial confinement, cells start to migrate in a collective manner, similar to migration patterns observed in strip-like 2D confinements[23]. In particular, as the tip cells invade the ECM slower than the cells within the branch migrate, collective back-and-forth patterns emerge. Simultaneously, cells constantly apply a traction force to the cage, which integrates within the branch due to the cellular coupling *via* cell-cell adhesion. As a result, the cells generate a significant tension inside the branch pointing in the direction of cell migration, as it is observed for epithelial cell sheets in 2D[18]. Yet, as the direction of migration alternates between an inward pointing and outward pointing direction, with uncorrelated migration modes in between, also the tension within the branch fluctuates in its magnitude. Thus, uncorrelated or outward pointing migration only leads to small perturbations in the ECM, while an inward pointing collective cell movement leads to a power stroke of the branch on the ECM. As a consequence, a distinct anisotropic displacement field in the ECM emerges, with high deformations towards the branch tip and no deformations at the sides. This

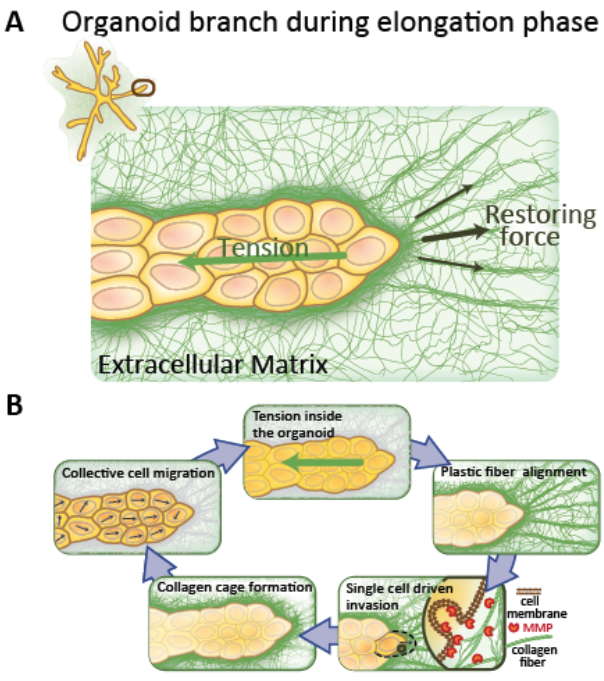

Figure 6-18: Branch elongation is dictated by a feedback loop. A *During elongation branches built-up a tension equilibrium between them and the ECM.* ***B*** *The collective cell migration within the branches leads to tension built-up, leading to contractions of the ECM. These deformations result in a plastic fiber alignment. The subsequent single cell invasion leads to the built-up of the collagen cage, which in turn enables the collective cell migration.*

deformation field in turn leads to an elongation of the collagen fibres in front of the invading branch, generating a restoring force of the collagen fibres pulling on the branch. The resulting force balance between tensile force of the branch and restoring force of the ECM prevents a relaxation of the elongated collagen fibres, which ultimately leads to plastic collagen fibre alignment. Accordingly, these aligned collagen fibres then guide the further elongation process as it is also observed for single cells and multicellular aggregates[98,114]. In addition, the ECM deformations towards the organoid cause a collagen accumulation and densification in front of the branch. *Via* collagen degradation utilizing MMPs tip cells invade into the ECM and thereby extend the branches. Further, the leading cells suppress the collagen to the sides of the branch. Ultimately, this compression of collagen fibres leads to the build-up of a mechanical stable and plastic collagen cage, which then again facilitates the collective cell migration within the branch.

6.5.2 Further applications

In this chapter it has been demonstrated that cells only invade the ECM at the tip of the branch, where a reduced accumulation of collagen is observable. This restriction is the result of the plastic collagen cage which acts as physical barrier for cells to invade their surrounding collagen matrix[115]. Additional Trichrome-stainings of cross-sections of human tissue reveal a similar collagen accumulation around human ducts *in vivo* (Fig. 6-19A). However, *in vivo* the biochemical composition of the accumulation is slightly more complex as it is further enriched with matrix proteins such as collagen IV, laminin and fibronectin[116]. Similarly, the observed collagen cage has been previously been reported also for murine mammary ducts as well as for the mouse mammary gland[117,118]. It is speculated that this accumulation stabilizes the growing ducts and guides the outgrowth[119]. However, the specific function and relevance of

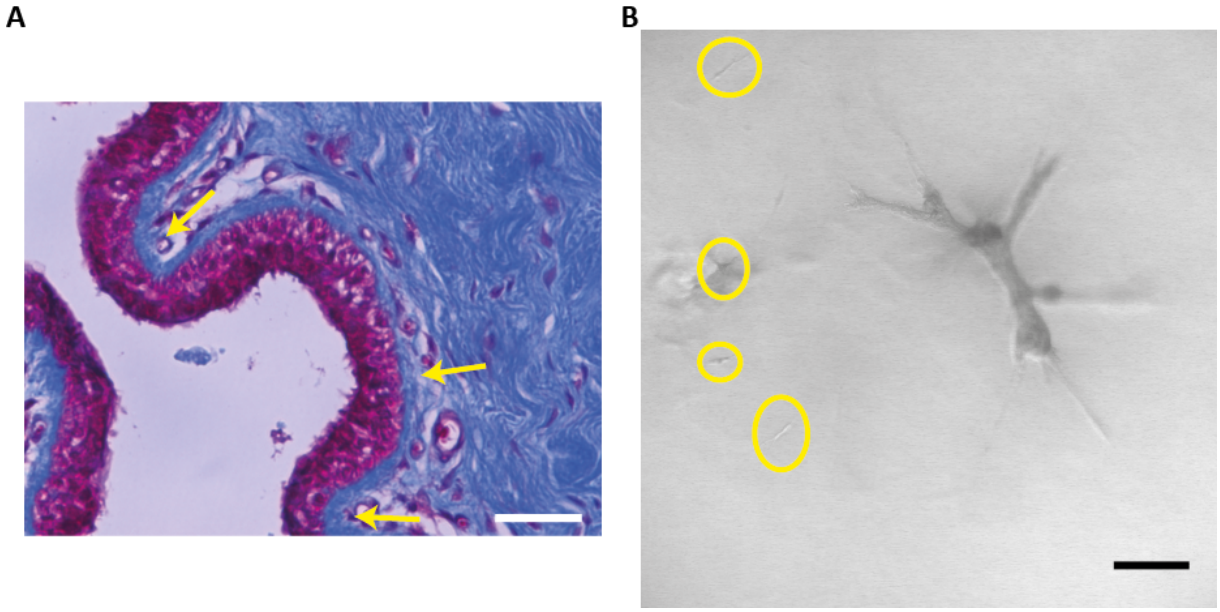

Figure 6-19: In vivo relevance and further applications. A *Trichrome staining of human cross sections. Yellow arrows indicate collagen accumulation. B Co-culture of basal organoids and primary human fibroblasts (yellow circles). As a consequence of the cell injection, fibroblasts are predominantly below the organoid. Scale bars, 100 µm (**A**), 200 µm (**B**).*

this collagen enrichment during and after growth has so far not been studied. Though, during cancer progression invasion of metastatic cells into the surrounding tissue is accompanied by defects in the basement membrane[120]. Thus, defects in the collagen cage could enable tumour invasion, which is further facilitated by aligned collagen fibres guiding metastatic cells to the blood vessels[40,118]. Obviously, such studies are highly limited by the accessibility of human tissue samples and are just restricted to static observations of diseased tissue. Consequently, the presented organoid assay would introduce a suitable possibility to study tumorigenesis and the relevance of the collagen cage with human tissue.

Yet, it has to be noted that the cellular composition of the human mammary gland *in vivo* is far more complex than the composition in the presented assay. *In vivo*, the human mammary gland is additionally surround by fibroblasts, endothelial cells, adipocytes, immune cells, and mesenchymal stem cells interacting with the ECM and epithelium[121]. By establishing a co-culture of different cell types the underlying interaction could be analysed in detail. First successful experiments co-culturing grown organoids with primary fibroblasts already demonstrate the possibility to cultivate different cell types within the same collagen gel (Fig. 6-19B). In addition, a full coverage of luminal organoids by basal organoids would further enhance the organoid systems and improve the replication of the human mammary gland. Hereby, a fine-tuning of the culture conditions to cultivate both systems as well as the controlled assembly into a bilayered architecture are two challenging requirements. Nevertheless, the here presented characterisation of the development of healthy luminal and basal organoids sets a first relevant benchmark for further studies.

7 Appendix

7.1 List of publications

Mechanical plasticity of collagen directs branch elongation in human mammary gland organoids
B. Buchmann, L. K. Engelbrecht, P. Fernandez, F. P. Hutterer, M. K. Raich, C. H. Scheel, A.R. Bausch
Nature Communications, **12**, 2759 (2021)

The role of nonlinear mechanical properties of biomimetic hydrogels for organoid growth
B. Buchmann, P. Fernandez, A. R. Bausch
Biophysics Reviews (accepted)

Surface tension induced budding drives alveologenesis in human mammary gland organoids
P. Fernandez, **B. Buchmann**, A. Goychuk, L. K. Engelbrecht, M.K. Raich, C. H. Scheel, E. Frey, A. R. Bausch
Nature Physics (under revision)

Generation of complex branched organoids from healthy mammary luminal cells reveals innate invasive potential
H. M. Ganz, **B. Buchmann**, L. K. Engelbrecht, M. Jesinghaus, C. J. Gabka, G. Schmidt, A. Muckenhuber, W. Weichert, A. R. Bausch, C. H. Scheel
The Journal of Pathology (under revision)

7.2 List of figures

7.3 List of tables

8 References

1. Sunyer, R. & Trepat, X. Durotaxis. *Current Biology* **30**, R383–R387 (2020).

2. Smith, L. R., Cho, S. & Discher, D. E. Stem Cell Differentiation is Regulated by Extracellular Matrix Mechanics. *Physiology* **33**, 16–25 (2018).

3. Tibbitt, M. W. & Anseth, K. S. Hydrogels as extracellular matrix mimics for 3D cell culture. *Biotechnol. Bioeng.* **103**, 655–663 (2009).

4. Geckil, H., Xu, F., Zhang, X., Moon, S. & Demirci, U. Engineering hydrogels as extracellular matrix mimics. *Nanomedicine* **5**, 469–484 (2010).

5. Chaudhuri, O., Cooper-White, J., Janmey, P. A., Mooney, D. J. & Shenoy, V. B. Effects of extracellular matrix viscoelasticity on cellular behaviour. *Nature* **584**, 535–546 (2020).

6. Kim, J., Koo, B.-K. & Knoblich, J. A. Human organoids: model systems for human biology and medicine. *Nat Rev Mol Cell Biol* **21**, 571–584 (2020).

7. Bray, F. *et al.* Global cancer statistics 2018: GLOBOCAN estimates of incidence and mortality worldwide for 36 cancers in 185 countries. *CA: A Cancer Journal for Clinicians* **68**, 394–424 (2018).

8. Harbeck, N. *et al.* Breast cancer. *Nat Rev Dis Primers* **5**, 66 (2019).

9. Linnemann, J. R. *et al.* Quantification of regenerative potential in primary human mammary epithelial cells. *Development* **142**, 3239–3251 (2015).

10. Maier, M. *et al.* A single charge in the actin binding domain of fascin can independently tune the linear and non-linear response of an actin bundle network. *Eur. Phys. J. E* **38**, 50 (2015).

11. Ban, E. *et al.* Mechanisms of Plastic Deformation in Collagen Networks Induced by Cellular Forces. *Biophysical Journal* **114**, 450–461 (2018).

12. Kapałczyńska, M. *et al.* 2D and 3D cell cultures – a comparison of different types of cancer cell cultures. *aoms* (2016) doi:10.5114/aoms.2016.63743.

13. Trepat, X., Chen, Z. & Jacobson, K. Cell Migration. in *Comprehensive Physiology* (ed. Terjung, R.) c110012 (John Wiley & Sons, Inc., 2012). doi:10.1002/cphy.c110012.

14. Ridley, A. J. Cell Migration: Integrating Signals from Front to Back. *Science* **302**, 1704–1709 (2003).

15. Wozniak, M. A., Modzelewska, K., Kwong, L. & Keely, P. J. Focal adhesion regulation of cell behavior. *Biochimica et Biophysica Acta (BBA) - Molecular Cell Research* **1692**, 103–119 (2004).

16. Han, S. J., Rodriguez, M. L., Al-Rekabi, Z. & Sniadecki, N. J. Spatial and temporal coordination of traction forces in one-dimensional cell migration. *Cell Adhesion & Migration* **10**, 529–539 (2016).

17. Rørth, P. Collective Cell Migration. *Annu. Rev. Cell Dev. Biol.* **25**, 407–429 (2009).

18. Trepat, X. *et al.* Physical forces during collective cell migration. *Nature Phys* **5**, 426–430 (2009).

19. Garcia, S. *et al.* Physics of active jamming during collective cellular motion in a monolayer. *Proc Natl Acad Sci USA* **112**, 15314–15319 (2015).

20. Pajic-Lijakovic, I. & Milivojevic, M. Jamming state transition and collective cell migration. *J Biol Eng* **13**, 73 (2019).

21. Latorre, E. *et al.* Active superelasticity in three-dimensional epithelia of controlled shape. *Nature* **563**, 203–208 (2018).

22. Liu, W.-W., Chen, Z.-L. & Jiang, X.-Y. Methods for Cell Micropatterning on Two-Dimensional Surfaces and Their Applications in Biology. *Chinese Journal of Analytical Chemistry* **37**, 943–949 (2009).

23. Vedula, S. R. K. *et al.* Emerging modes of collective cell migration induced by geometrical constraints. *Proceedings of the National Academy of Sciences* **109**, 12974–12979 (2012).

24. Segerer, F. J., Thüroff, F., Piera Alberola, A., Frey, E. & Rädler, J. O. Emergence and Persistence of Collective Cell Migration on Small Circular Micropatterns. *Phys. Rev. Lett.* **114**, 228102 (2015).

25. Jain, S. *et al.* The role of single-cell mechanical behaviour and polarity in driving collective cell migration. *Nat. Phys.* **16**, 802–809 (2020).

26. Xi, W., Sonam, S., Beng Saw, T., Ladoux, B. & Teck Lim, C. Emergent patterns of collective cell migration under tubular confinement. *Nat Commun* **8**, 1517 (2017).

27. Yamada, K. M. & Sixt, M. Mechanisms of 3D cell migration. *Nat Rev Mol Cell Biol* **20**, 738–752 (2019).

28. Petrie, R. J., Koo, H. & Yamada, K. M. Generation of compartmentalized pressure by a nuclear piston governs cell motility in a 3D matrix. *Science* **345**, 1062–1065 (2014).

29. Carey, S. P., Martin, K. E. & Reinhart-King, C. A. Three-dimensional collagen matrix induces a mechanosensitive invasive epithelial phenotype. *Sci Rep* **7**, 42088 (2017).

30. Ehrbar, M. *et al.* Elucidating the Role of Matrix Stiffness in 3D Cell Migration and Remodeling. *Biophysical Journal* **100**, 284–293 (2011).

31. Rhee, S. Fibroblasts in three dimensional matrices: cell migration and matrix remodeling. *Exp Mol Med* **41**, 858 (2009).

32. Roca-Cusachs, P., Sunyer, R. & Trepat, X. Mechanical guidance of cell migration: lessons from chemotaxis. *Current Opinion in Cell Biology* **25**, 543–549 (2013).

33. Wisdom, K. M. *et al.* Matrix mechanical plasticity regulates cancer cell migration through confining microenvironments. *Nat Commun* **9**, 4144 (2018).

34. Sundararaghavan, H. G., Saunders, R. L., Hammer, D. A. & Burdick, J. A. Fiber alignment directs cell motility over chemotactic gradients. *Biotechnol. Bioeng.* **110**, 1249–1254 (2013).

35. Riching, K. M. *et al.* 3D Collagen Alignment Limits Protrusions to Enhance Breast Cancer Cell Persistence. *Biophysical Journal* **107**, 2546–2558 (2014).

36. Ochoa-Espinosa, A. & Affolter, M. Branching Morphogenesis: From Cells to Organs and Back. *Cold Spring Harbor Perspectives in Biology* **4**, a008243–a008243 (2012).

37. Varner, V. D. & Nelson, C. M. Cellular and physical mechanisms of branching morphogenesis. *Development* **141**, 2750–2759 (2014).

38. Ewald, A. J., Brenot, A., Duong, M., Chan, B. S. & Werb, Z. Collective Epithelial Migration and Cell Rearrangements Drive Mammary Branching Morphogenesis. *Developmental Cell* **14**, 570–581 (2008).

39. Weaver, M., Dunn, N. R. & Hogan, B. L. Bmp4 and Fgf10 play opposing roles during lung bud morphogenesis. *Development* **127**, 2695–2704 (2000).

40. Brownfield, D. G. *et al.* Patterned Collagen Fibers Orient Branching Mammary Epithelium through Distinct Signaling Modules. *Current Biology* **23**, 703–709 (2013).

41. Schottenfeld, J., Song, Y. & Ghabrial, A. S. Tube continued: morphogenesis of the Drosophila tracheal system. *Current Opinion in Cell Biology* **22**, 633–639 (2010).

42. Ghabrial, A. S. & Krasnow, M. A. Social interactions among epithelial cells during tracheal branching morphogenesis. *Nature* **441**, 746–749 (2006).

43. Corrò, C., Novellasdemunt, L. & Li, V. S. W. A brief history of organoids. *American Journal of Physiology-Cell Physiology* **319**, C151–C165 (2020).

44. Clevers, H. Modeling Development and Disease with Organoids. *Cell* **165**, 1586–1597 (2016).

45. Bartfeld, S. & Clevers, H. Stem cell-derived organoids and their application for medical research and patient treatment. *J Mol Med* **95**, 729–738 (2017).

46. Schutgens, F. & Clevers, H. Human Organoids: Tools for Understanding Biology and Treating Diseases. *Annu. Rev. Pathol. Mech. Dis.* **15**, 211–234 (2020).

47. Hassiotou, F. & Geddes, D. Anatomy of the human mammary gland: Current status of knowledge. *Clin. Anat.* **26**, 29–48 (2013).

48. Sopel, M. The myoepithelial cell: its role in normal mammary glands and breast cancer. *Folia Morphol (Warsz)* **69**, 1–14 (2010).

49. Tiede, B. & Kang, Y. From milk to malignancy: the role of mammary stem cells in development, pregnancy and breast cancer. *Cell Res* **21**, 245–257 (2011).

50. dos Santos, C. O., Dolzhenko, E., Hodges, E., Smith, A. D. & Hannon, G. J. An Epigenetic Memory of Pregnancy in the Mouse Mammary Gland. *Cell Reports* **11**, 1102–1109 (2015).

51. Watson, C. J. Key stages in mammary gland development - Involution: apoptosis and

tissue remodelling that convert the mammary gland from milk factory to a quiescent organ. *Breast Cancer Res* **8**, 203 (2006).

52. McNally, S. & Stein, T. Overview of Mammary Gland Development: A Comparison of Mouse and Human. in *Mammary Gland Development* (eds. Martin, F., Stein, T. & Howlin, J.) vol. 1501 1–17 (Springer New York, 2017).

53. Sokol, E. S. *et al.* Growth of human breast tissues from patient cells in 3D hydrogel scaffolds. *Breast Cancer Res* **18**, 19 (2016).

54. Jamieson, P. R. *et al.* Derivation of a robust mouse mammary organoid system for studying tissue dynamics. *Development* **144**, 1065–1071 (2017).

55. Geraldo, S., Simon, A. & Vignjevic, D. M. Revealing the Cytoskeletal Organization of Invasive Cancer Cells in 3D. *JoVE* 50763 (2013) doi:10.3791/50763.

56. Mason, B. N., Starchenko, A., Williams, R. M., Bonassar, L. J. & Reinhart-King, C. A. Tuning three-dimensional collagen matrix stiffness independently of collagen concentration modulates endothelial cell behavior. *Acta Biomaterialia* **9**, 4635–4644 (2013).

57. Sachs, N. *et al.* A Living Biobank of Breast Cancer Organoids Captures Disease Heterogeneity. *Cell* **172**, 373-386.e10 (2018).

58. Raich, M. K. Laser-induced ablation to probe strain exerted by mammary gland organoid growth. (Technische Universität München, 2018).

59. Ushakov, L. Confocal data correction using image processing. (Technische Universität München, 2019).

60. Tinevez, J.-Y. *et al.* TrackMate: An open and extensible platform for single-particle tracking. *Methods* **115**, 80–90 (2017).

61. Nicolas, J. *et al.* 3D Extracellular Matrix Mimics: Fundamental Concepts and Role of Materials Chemistry to Influence Stem Cell Fate. *Biomacromolecules* **21**, 1968–1994 (2020).

62. Hughes, C. S., Postovit, L. M. & Lajoie, G. A. Matrigel: A complex protein mixture required for optimal growth of cell culture. *Proteomics* **10**, 1886–1890 (2010).

63. Kandow, C. E., Georges, P. C., Janmey, P. A. & Beningo, K. A. Polyacrylamide Hydrogels for Cell Mechanics: Steps Toward Optimization and Alternative Uses. in *Methods in Cell Biology* vol. 83 29–46 (Elsevier, 2007).

64. Almany, L. & Seliktar, D. Biosynthetic hydrogel scaffolds made from fibrinogen and polyethylene glycol for 3D cell cultures. *Biomaterials* **26**, 2467–2477 (2005).

65. Rowley, J. A., Madlambayan, G. & Mooney, D. J. Alginate hydrogels as synthetic extracellular matrix materials. *Biomaterials* **20**, 45–53 (1999).

66. Kleinman, H. K. *et al.* Basement membrane complexes with biological activity. *Biochemistry* **25**, 312–318 (1986).

67. Kleinman, H. K. & Martin, G. R. Matrigel: Basement membrane matrix with biological activity. *Seminars in Cancer Biology* **15**, 378–386 (2005).

68. Poincloux, R., Lizárraga, F. & Chavrier, P. Matrix invasion by tumour cells: a focus on MT1-MMP trafficking to invadopodia. *Journal of Cell Science* **122**, 3015–3024 (2009).

69. Jansen, K. A. *et al.* The Role of Network Architecture in Collagen Mechanics. *Biophysical Journal* **114**, 2665–2678 (2018).

70. Sung, K. E. *et al.* Control of 3-dimensional collagen matrix polymerization for reproducible human mammary fibroblast cell culture in microfluidic devices. *Biomaterials* **30**, 4833–4841 (2009).

71. Glentis, A., Gurchenkov, V. & Vignjevic, D. M. Assembly, heterogeneity, and breaching of the basement membranes. *Cell Adhesion & Migration* **8**, 236–245 (2014).

72. Zuidema, J. M., Rivet, C. J., Gilbert, R. J. & Morrison, F. A. A protocol for rheological characterization of hydrogels for tissue engineering strategies: A Protocol for Rheological Characterization of Hydrogels. *J. Biomed. Mater. Res.* **102**, 1063–1073 (2014).

73. Kane, K. I. W. *et al.* Determination of the rheological properties of Matrigel for optimum seeding conditions in microfluidic cell cultures. *AIP Advances* **8**, 125332 (2018).

74. Motte, S. & Kaufman, L. J. Strain stiffening in collagen I networks. *Biopolymers* **99**, 35–46 (2013).

75. Munster, S. *et al.* Strain history dependence of the nonlinear stress response of fibrin and collagen networks. *Proceedings of the National Academy of Sciences* **110**, 12197–12202 (2013).

76. Schmoller, K. M., Fernández, P., Arevalo, R. C., Blair, D. L. & Bausch, A. R. Cyclic hardening in bundled actin networks. *Nat Commun* **1**, 134 (2010).

77. Schmoller, K. M. & Bausch, A. R. Similar nonlinear mechanical responses in hard and soft materials. *Nature Materials* **12**, 278–281 (2013).

78. Nguyen-Ngoc, K.-V. *et al.* 3D Culture Assays of Murine Mammary Branching Morphogenesis and Epithelial Invasion. in *Tissue Morphogenesis* (ed. Nelson, C. M.) vol. 1189 135–162 (Springer New York, 2015).

79. Mullins, L. Softening of Rubber by Deformation. *Rubber Chemistry and Technology* **42**, 339–362 (1969).

80. Marton, R. M. & Pașca, S. P. Organoid and Assembloid Technologies for Investigating Cellular Crosstalk in Human Brain Development and Disease. *Trends in Cell Biology* **30**, 133–143 (2020).

81. Davis, T. L. & Rebay, I. Master regulators in development: Views from the Drosophila retinal determination and mammalian pluripotency gene networks. *Developmental Biology* **421**, 93–107 (2017).

82. Stratman, A. N. *et al.* Interactions between mural cells and endothelial cells stabilize the developing zebrafish dorsal aorta. *Development* **144**, 115–127 (2017).

83. Huebner, R. J., Neumann, N. M. & Ewald, A. J. Mammary epithelial tubes elongate

through MAPK-dependent coordination of cell migration. *Development* **143**, 983–993 (2016).

84. Paul, C. D., Hung, W.-C., Wirtz, D. & Konstantopoulos, K. Engineered Models of Confined Cell Migration. *Annu. Rev. Biomed. Eng.* **18**, 159–180 (2016).

85. Mohammed, D. *et al.* Substrate area confinement is a key determinant of cell velocity in collective migration. *Nat. Phys.* **15**, 858–866 (2019).

86. Jonkman, J. E. N. *et al.* An introduction to the wound healing assay using live-cell microscopy. *Cell Adhesion & Migration* **8**, 440–451 (2014).

87. Zhang, Y. *et al.* Tissue-specific extracellular matrix coatings for the promotion of cell proliferation and maintenance of cell phenotype. *Biomaterials* **30**, 4021–4028 (2009).

88. Lock, J. G., Wehrle-Haller, B. & Strömblad, S. Cell–matrix adhesion complexes: Master control machinery of cell migration. *Seminars in Cancer Biology* **18**, 65–76 (2008).

89. Winkler, B., Aranson, I. S. & Ziebert, F. Confinement and substrate topography control cell migration in a 3D computational model. *Commun Phys* **2**, 82 (2019).

90. Wang, S., Sekiguchi, R., Daley, W. P. & Yamada, K. M. Patterned cell and matrix dynamics in branching morphogenesis. *Journal of Cell Biology* **216**, 559–570 (2017).

91. Hannezo, E. *et al.* A Unifying Theory of Branching Morphogenesis. *Cell* **171**, 242-255.e27 (2017).

92. Gjorevski, N., S. Piotrowski, A., Varner, V. D. & Nelson, C. M. Dynamic tensile forces drive collective cell migration through three-dimensional extracellular matrices. *Sci Rep* **5**, 11458 (2015).

93. Liu, S. The ROCK signaling and breast cancer metastasis. *Mol Biol Rep* **38**, 1363–1366 (2011).

94. Boussadia, O., Kutsch, S., Hierholzer, A., Delmas, V. & Kemler, R. E-cadherin is a survival factor for the lactating mouse mammary gland. *Mechanisms of Development* **115**, 53–62 (2002).

95. Siitonen, S. M. *et al.* Reduced E-Cadherin Expression is Associated With Invasiveness and Unfavorable Prognosis in Breast Cancer. *Am J Clin Pathol* **105**, 394–402 (1996).

96. Wiseman, B. S. *et al.* Site-specific inductive and inhibitory activities of MMP-2 and MMP-3 orchestrate mammary gland branching morphogenesis. *Journal of Cell Biology* **162**, 1123–1133 (2003).

97. Hall, M. S. *et al.* Fibrous nonlinear elasticity enables positive mechanical feedback between cells and ECMs. *Proc Natl Acad Sci USA* **113**, 14043–14048 (2016).

98. Piotrowski-Daspit, A. S., Nerger, B. A., Wolf, A. E., Sundaresan, S. & Nelson, C. M. Dynamics of Tissue-Induced Alignment of Fibrous Extracellular Matrix. *Biophysical Journal* **113**, 702–713 (2017).

99. Kraning-Rush, C. M., Carey, S. P., Califano, J. P., Smith, B. N. & Reinhart-King, C. A. The role of the cytoskeleton in cellular force generation in 2D and 3D environments. *Phys. Biol.* **8**,

015009 (2011).

100. Von Der Mark, K., Gauss, V., Von Der Mark, H. & Müller, P. Relationship between cell shape and type of collagen synthesised as chondrocytes lose their cartilage phenotype in culture. *Nature* **267**, 531–532 (1977).

101. Birgersdotter, A., Sandberg, R. & Ernberg, I. Gene expression perturbation in vitro—A growing case for three-dimensional (3D) culture systems. *Seminars in Cancer Biology* **15**, 405–412 (2005).

102. Petersen, O. W., Ronnov-Jessen, L., Howlett, A. R. & Bissell, M. J. Interaction with basement membrane serves to rapidly distinguish growth and differentiation pattern of normal and malignant human breast epithelial cells. *Proceedings of the National Academy of Sciences* **89**, 9064–9068 (1992).

103. Zhou, H. & Kramer, R. H. Integrin Engagement Differentially Modulates Epithelial Cell Motility by RhoA/ROCK and PAK1. *Journal of Biological Chemistry* **280**, 10624–10635 (2005).

104. Shah, M. M., Sampogna, R. V., Sakurai, H., Bush, K. T. & Nigam, S. K. Branching morphogenesis and kidney disease. *Development* **131**, 1449–1462 (2004).

105. Whitsett, J. A., Kalin, T. V., Xu, Y. & Kalinichenko, V. V. Building and Regenerating the Lung Cell by Cell. *Physiological Reviews* **99**, 513–554 (2019).

106. Villasenor, A., Chong, D. C., Henkemeyer, M. & Cleaver, O. Epithelial dynamics of pancreatic branching morphogenesis. *Development* **137**, 4295–4305 (2010).

107. Sternlicht, M. D. Key stages in mammary gland development: The cues that regulate ductal branching morphogenesis. *Breast Cancer Res* **8**, 201 (2005).

108. Lu, P., Sternlicht, M. D. & Werb, Z. Comparative Mechanisms of Branching Morphogenesis in Diverse Systems. *J Mammary Gland Biol Neoplasia* **11**, 213–228 (2006).

109. Fata, J. E., Werb, Z. & Bissell, M. J. Regulation of mammary gland branching morphogenesis by the extracellular matrix and its remodeling enzymes. *Breast Cancer Res* **6**, 1 (2003).

110. Rozario, T. & DeSimone, D. W. The extracellular matrix in development and morphogenesis: A dynamic view. *Developmental Biology* **341**, 126–140 (2010).

111. Wang, H., Abhilash, A. S., Chen, C. S., Wells, R. G. & Shenoy, V. B. Long-Range Force Transmission in Fibrous Matrices Enabled by Tension-Driven Alignment of Fibers. *Biophysical Journal* **107**, 2592–2603 (2014).

112. Sumbal, J., Budkova, Z., Traustadóttir, G. Á. & Koledova, Z. Mammary Organoids and 3D Cell Cultures: Old Dogs with New Tricks. *J Mammary Gland Biol Neoplasia* **25**, 273–288 (2020).

113. Srivastava, V., Huycke, T. R., Phong, K. T. & Gartner, Z. J. Organoid models for mammary gland dynamics and breast cancer. *Current Opinion in Cell Biology* **66**, 51–58 (2020).

114. Ray, A., Slama, Z. M., Morford, R. K., Madden, S. A. & Provenzano, P. P. Enhanced

Directional Migration of Cancer Stem Cells in 3D Aligned Collagen Matrices. *Biophysical Journal* **112**, 1023–1036 (2017).

115. Cho, Y. *et al.* Construction of a 3D mammary duct based on spatial localization of the extracellular matrix. *NPG Asia Mater* **10**, 970–981 (2018).

116. Maller, O., Martinson, H. & Schedin, P. Extracellular Matrix Composition Reveals Complex and Dynamic Stromal-Epithelial Interactions in the Mammary Gland. *J Mammary Gland Biol Neoplasia* **15**, 301–318 (2010).

117. Nerger, B. A. *et al.* Local accumulation of extracellular matrix regulates global morphogenetic patterning in the developing mammary gland. *Current Biology* S0960982221002220 (2021) doi:10.1016/j.cub.2021.02.015.

118. Provenzano, P. P. *et al.* Collagen reorganization at the tumor-stromal interface facilitates local invasion. *BMC Med* **4**, 38 (2006).

119. Silberstein, G. B. & Daniel, C. W. Glycosaminoglycans in the basal lamina and extracellular matrix of the developing mouse mammary duct. *Developmental Biology* **90**, 215–222 (1982).

120. Chang, J. & Chaudhuri, O. Beyond proteases: Basement membrane mechanics and cancer invasion. *Journal of Cell Biology* **218**, 2456–2469 (2019).

121. Dzięgelewska, Ż. & Gajewska, M. Stromal-Epithelial Interactions during Mammary Gland Development. in *Stromal Cells - Structure, Function, and Therapeutic Implications* (ed. T. Valarmathi, M.) (IntechOpen, 2019). doi:10.5772/intechopen.80405.